Analyzing the Connection among Aerosol Optical Depth, Precipitation and Temperature in Southern India

K. THARANI
(Roll No: 718103)

DEPARTMENT OF CIVIL ENGINEERING
NATIONAL INSTITUTE OF TECHNOLOGY
WARANGAL, TELANGANA – 506004, INDIA
DECEMBER – 2023

Analyzing the Connection among Aerosol Optical Depth, Precipitation and Temperature in Southern India

Submitted in partial fulfilment of the requirements
for the award of the degree of

DOCTOR OF PHILOSOPHY

in

CIVIL ENGINEERING

by

K. THARANI

(Roll No: 718103)

Supervisor

Dr. VENKATA REDDY KEESARA

Professor

DEPARTMENT OF CIVIL ENGINEERING

NATIONAL INSTITUTE OF TECHNOLOGY

WARANGAL, TELANGANA – 506004, INDIA

DECEMBER-2023

To my father, who nurtured me.

To my mother, who stood like a pillar for me.

To my husband and son, who is with me through thick and thin.

To my sister, who never left my side.

NATIONAL INSTITUTE OF TECHNOLOGY

WARANGAL

CERTIFICATE

This is to certify that the thesis entitled **"Analyzing the Connection among Aerosol Optical Depth, Precipitation and Temperature in Southern India"** being submitted by **Mrs. K. THARANI** for the award of the degree of **DOCTOR OF PHILOSOPHY** in the Department of Civil Engineering, National Institute of Technology, Warangal, is a record of bonafide research work carried out by her under my supervision and it has not been submitted elsewhere for award of any degree.

Dr. Venkata Reddy Keesara
Thesis Supervisor
Professor
Department of Civil Engineering
National Institute of Technology
Warangal (T.S) – India

Dissertation Approval

This dissertation entitled **"Analyzing the Connection among Aerosol Optical Depth, Precipitation and Temperature in Southern India"** by **Mrs. K. THARANI** is approved for the degree of **Doctor of Philosophy.**

Examiners

_____

_____

_____

Supervisor(s)

_____

_____

_____

Chairman

_____

Date: _____

Place: _____

DECLARATION

This is to certify that the work presented in the thesis entitled **"Analyzing the Connection among Aerosol Optical Depth, Precipitation and Temperature in Southern India"** is a bonafide work done by me under the supervision of **Dr. Venkata Reddy Keesara** and was not submitted elsewhere for the award of any degree. I declare that this written submission represents my ideas in my own words and where others' ideas or words have been included, I have adequately cited and referenced the original sources. I also declare that I have adhered to all principles of academic honesty and integrity and have not misrepresented or fabricated or falsified any idea / data / fact /source in my submission. I understand that any violation of the above will be a cause for disciplinary action by the Institute and can also evoke penal action from the sources which have thus not been properly cited or from whom proper permission has not been taken when needed.

_____

(K. THARANI)

(Roll No: **718103**)

Date: _____

Acknowledgements

I would like to express my gratitude to the National Institute of Technology, Warangal (NITW) for providing me with the chance to collaborate with amazing individuals and for their support in finishing my thesis work, as conducting research demands a lot of resources, encouragement, and motivation.

First and foremost, I would like to sincerely thank ***Prof. Venkata Reddy Keesara***, Professor in the Department of Civil Engineering, who oversaw my thesis. He provided me insights on research, moral support, tolerance, encouragement, and timely input during my doctoral studies. Despite all the difficulties he faced, his advice was quite helpful to me throughout my entire research project. I will always be inspired by his commitment to research for the rest of my life. I will be motivated to conduct research throughout my life by his motto, "Little research everyday adds up to big results."

In addition to the support, I received from my supervisor, I am indebted to ***Prof. Devapratap*** for his valuable support throughout my research work. The way he balances his personal and professional life is always an inspiration for me.

I am thankful to my Doctoral Scrutiny Committee: Chairman ***Prof. T. D. Gunneswara Rao***, Professor and Head, Department of Civil Engineering and members ***Prof. N V Umamahesh***, Professor, Department of Civil Engineering, ***Dr. Manali Pal***, Assistant Professor, Department of Civil Engineering, and ***Prof. D. Srinivasacharya***, Professor, Department of Mathematics for their close observation, perceptive criticism, and encouragement.

I express my gratitude to my family of research scholars for their unwavering support, both directly and indirectly, during the research project and for fostering a joyful and stimulating work atmosphere. Last but not the least I extend my biggest and whole hearted thanks to my family members for their affection and encouragement throughout the research period.

K. Tharani
Roll No: 718103

Abstract

Aerosols are fine suspended solid or liquid particles in the atmosphere. Anthropogenic aerosols from industrialization and urbanization are one of the prominent parameters in the climate change process. Aerosol Optical Depth (AOD) is a quantitative estimate of the amount of aerosol present in the atmosphere. The rise in concentration of aerosols in the atmosphere has affected the clear sky's visibility in most of the metropolitan cities. The presence of aerosols has direct and indirect effects on the climate system. The direct effect of AOD was to influence temperature through the absorption or scattering of radiation. The radiative energy balance within the atmosphere of the Earth is highly affected by the presence of aerosols as they are capable of scattering and absorbing the incoming solar radiation. The indirect effect of AOD is on the formation of cloud condensation nuclei which in turn affects the precipitation of a region. The current research studied the impact of AOD on precipitation and temperature patterns in the study area along with the quantification of parameters that resulted in Extreme Precipitation Events (EPEs). The AOD data from satellite and ground observations are the main source in studying the effect of aerosol on spatial patterns of precipitation and temperature in Southern India. The suitability of satellite data was evaluated by validating various satellite observations with the ground data. The continuous AOD data was validated against ground observations at Pune and Kanpur statistically and it was observed that Moderate Resolution Spectrometer (MODIS) was closely correlated with ground observations. The coefficient of determination is 0.58 for Pune station and 0.7 for Kanpur station. Trend in AOD was assessed for two decades over Southern India using Mann-Kendall test and Innovative Trend Analysis method. Both the tests showed a decrease in area of significant trend for second decade when compared to first decade. It was observed that 67% and 40% of area showed a significant positive trend in first- and second-decades using Mann-Kendall test. On the contrary, 42% and 30% of area showed a significant positive trend in first and second decades using Innovative Trend Analysis method. The impact of AOD on temperature in the study area was assessed by using Aerosol Direct Radiative Forcing (ADRF) method. It is a measurement utilized to comprehend the impact of cooling or warming up of the atmosphere. The present research examined the impact of aerosols during the COVID-19 pandemic by comparing them to the average from the preceding five-year period (2015-2019). The study was carried out on three distinct time frames: prior to lockdown, during lockdown, and post lockdown. It was observed that the ADRF increased in the pre-lockdown period of 2020 compared against the average of 2015-2019, and the other time scales experienced an increase in ADRF. However, a drop in temperature was noticed

prior to lockdown period when compared to the other two-time frames. During the pre-lockdown period, the most notable rise in ADRF and decrease in temperature occurred in the tropical savanna and warm semi-arid climate regions. During lockdown, the increase in ADRF was seen throughout the study area, and a decrease in temperature was observed only in the tropical monsoon region. In the post-lockdown period, the decline in ADRF was accompanied by a fall in temperature in the tropical savanna region. The indirect effect of aerosols was assessed by correlation analysis among AOD, CF and precipitation for south west monsoon from 2005 to 2019 under different atmospheric stability states (K-index) over Southern India. The analysis was performed for light, moderate and heavy rainfall regimes. The low warm clouds were analysed based on cloud top pressure and cloud top temperature data. The impact of atmospheric stability on CF was greater than that on AOD. The results revealed a positive relationship between AOD and CF. This might be due to the presence of dispersive aerosols. The effect of atmospheric stability on development of clouds was evident for isolated thunderstorm state when K is between 20-25. The effect of AOD on CF was significant for $20<K<25$ and $25<K<30$. For a better understanding on the influence of AOD on precipitation an exclusive study on metropolitan cities was performed in the current research work. The influence of AOD in causing the EPEs was quantified by analyzing the remotely sensed data of aerosol, cloud, and K-index and precipitation for Peninsular India's major cities. The last 10 days remotely sensed data before the occurrence of EPE's event was analyzed. The combination of factors influencing precipitation in each city were analyzed by regression analysis. All the observed EPEs had intensified precipitation due to a combination of middle level clouds (CTP in the range of 440 hPa to 680 hPa), low AOD (0.4), with many thunderstorm states ($K>35^oC$), and CTT 0^oC. Other elements that contributed to the occurrence of EPE included low level clouds (CTP>680 hPa), an AOD in the range of 0.4–0.6, an isolated thunderstorm state ($20^oC<K<25^oC$), and $CTT>0^oC$. It was concluded that low AOD and moderate CF leads to precipitation under favorable cloud top properties.

Keywords: Aerosol Optical Depth, Atmospheric Stability, Cloud Fraction, Cloud Top Pressure, Cloud Top Temperature, Low- warm clouds, Precipitation, Extreme Precipitation Events

Table of Contents

Acknowledgements iv

Abstract v

List of Tables x

List of Figures xi

Nomenclature xiv

Abbreviations xv

1. Introduction 1

1.1 General 1

1.2 Aerosol Optical Depth 1

1.3 Direct effect of aerosols on climate system 2

1.4 Indirect effect of aerosols on climate system 4

1.5 Research Motivation 5

1.6 Aim and Objectives 5

1.7 Outline of thesis 6

2. Literature Review 7

2.1 General 7

2.2 Validation of Satellite and Model Re-Analysis Data with Observed Data 7

2.3 Trend Analysis Using R Statistical Software 9

2.4 Effect of Aerosols on Temperature 11

2.5 Impact of AOD on Cloud Fraction and Precipitation 13

2.6 Analysis of the Causes for Occurrence of EPE in Metropolitan Cities 15

2.7 Critical Appraisal of Reviewed literature 16

3. Methodology 18

3.1 General 18

3.2 Study Area 18

3.3 Data Used in the Present Study 20

3.3.1 MODIS Data Products 20

3.3.2 Precipitation Data 22

3.3.3 Radiation Flux Data 22

3.3.4 Temperature Data 23

3.3.5 AERONET Data 23

3.4 Overall methodology 23
3.5 Validation of Various Satellite Derived AOD Data with Ground Observations 24
3.6 Trend Analysis 27
3.6.1 Mann-Kendall Test 27
3.6.2 Innovative Trend Analysis 29
3.7 AOD-Radiation- Temperature Interaction 29
3.7.1 Calculation of Aerosol Direct Radiative Forcing 30
3.7.2 Effect of Aerosols on Temperature 31
3.8 Aerosol-Cloud-Precipitation Interactions 31
3.9 Analysis of the causes for extreme precipitation events in and around urban cities 33
3.9.1 Percentile Calculation 34
3.9.2 Identification of Events 35
3.9.3 Analysis of Parameters 35
3.9.4 Multiple Linear Regression Analysis 35
3.10 Closure 36
4. Validation of Various Satellite and Model Re-analysis Derived AOD Data with Ground Observations 37
4.1 General 37
4.2 Datasets for Validation 37
4.2.1 Statistics of Validation 38
4.3 Spatial Distribution of AOD 40
4.4 Decadal trends in Aerosol Optical Depth 40
4.4.1 Trend in MODIS AOD using Mann-Kendall test 41
4.4.2 Trend in MODIS AOD using Innovative Trend Analysis Method 43
4.5 Closure 44
5. Impact of AOD on Radiation Diagnostics and Temperature 45
5.1 General 45
5.2 Calculation of Aerosol Direct Radiative Forcing 45
5.2.1 Trend in ADRF 47
5.3 Yearly variations in the AOD, ADRF and temperature for the three different timescales 48
5.4 COVID-19 Lockdown: Pristine situation 50
5.5 Spatial Distribution of AOD in the Atmosphere 50
5.6 Spatial Distribution of ADRF in the Atmosphere 52
5.7 Spatial Distribution of Temperature in the Atmosphere 54

5.8 Closure 56

6. Impact of AOD on Cloud Fraction and Precipitation 57

6.1 General 57

6.2 Comprehensive Effect of AOD on CF 57

6.3 Observed relationship between AOD and CF based on atmospheric stability 59

6.4 Overall effect of AOD on CF and Precipitation 64

6.5 Spatial distribution of AOD and CF 68

6.6 Analysis of causes for extreme precipitation events in urban cities of peninsular India 77

6.6.1 Mean Precipitation 77

6.6.2 Spatial Distribution Maps 78

6.6.2.1 Mumbai 78

6.6.2.2 Chennai 79

6.6.2.3 Hyderabad 80

6.6.2.4 Bengaluru 81

6.6.3 Regression Analysis 82

6.7 Closure 84

7. Summary and Conclusions 85

7.1 General 85

7.2 Summary 85

7.3 Conclusions 86

7.4 Research Contributions 88

7.5 Limitations of the study 89

7.6 Future Scope 89

References 90

List of Publications 99

Appendix- A 100

List of Tables

Table 3.1	Details about the satellite data, parameters, and spatial resolution used in this study	21
Table 4.1	Statistical errors for evaluation of MODIS, OMI, MERRA-2 with AERONET	38
Table 4.2	Area of significant change obtained in both the tests (Lakh ha)	42
Table 5.1	Area of significant change in each climate zone (in lakh hectares)	48
Table 6.1	AOD and CF correlation coefficients for various atmospheric stability states	63
Table 6.2	Areal distribution of AOD and CF for each climatic region under light rain in 100,000 ha	74
Table 6.3	Areal distribution of AOD and CF for each climatic region under moderate rain in 100,000 ha	75
Table 6.4	Areal distribution of AOD and CF for each climatic region under heavy rain in 100,000 ha	76
Table 6.5	Multiple Linear Regression (MLR) models for the four metropolitan cities of Mumbai, Chennai, Bengaluru and Hyderabad to predict precipitation depth during an EPE (Significance level '***' 0.001 '**' 0.01 '*' 0.05)	83

List of Figures

Fig 1.1	a) Direct Effect of Aerosols b) Indirect Effect of Aerosols on climate (Source: IPCC 2013)	3
Fig 3.1	Location map of Study Area with Koppen's Climate Zones	20
Fig 3.2	Overall Methodology for the Present Study	24
Fig 3.3	Flowchart for the methodology of validating satellite and re-analysis AOD data with ground observations	25
Fig 3.4	Methodology adapted for understanding AOD-Radiation-Temperature Interactions	30
Fig 3.5	Flow chart showing the methodology adopted for AOD-Cloud-Precipitation Interactions	32
Fig 3.6	An Overview of the Research Approach for understanding the causes influencing the occurrence of EPE in metropolitan cities	34
Fig 4.1	Correlation plots of a) MODIS with AERONET for Pune b) MODIS with AERONET for Kanpur c) MERRA-2 with AERONET for Pune d) MERRA-2 with AERONET for Kanpur e) OMI with AERONET for Pune f) OMI with AERONET for Kanpur	39
Fig 4.2	Spatial distribution of AOD over Southern India a) 2000-2009 b) 2010-2019	40
Fig 4.3	Spatial Pattern of trend in AOD at 95% significance level for a) 2000-2009 b) 2010-2019 using Mann-Kendall Test	42
Fig 4.4	Spatial Pattern of trend in AOD at 95% significance level for a) 2000-2009 b) 2010-2019 using ITA	44
Fig 5.1	Time series plot of LWGNT, LWGNTCLN_f, LWGNTCLN_d for a) Goa b) Nanded c) Hyderabad d) Raipur e) Coimbatore for the year 2019	46
Fig 5.2	Spatial distribution of trend in ADRF	48
Fig 5.3	Variation of Parameters over the time period 2015-2020 in three timescales a) AOD b) ADRF c) Temperature (Error bar represents standard error in the parameter considered during timescale of each	49

year)

Fig 5.4	Spatial distribution of AOD for a) Pre-lockdown b) Lockdown c) Post-lockdown time periods (Left Average of 2015-2019, Middle 2020, Right Change)	51
Fig 5.5	Spatial distribution of ADRF in the atmosphere for a) Pre-lockdown b) Lockdown c) Post-lockdown time periods (Left Average of 2015-2019, Middle 2020, Right Change)	53
Fig 5.6	Spatial distribution of mean temperature for a) Pre-lockdown b) Lockdown c) Post-lockdown time periods (Left Average of 2015-2019, Middle 2020, Right Change)	53
Fig 6.1	Equal Value Plots of AOD and CF for a) light rain b) moderate rain c) heavy rain (The orange line shows the 1-1 line)	58
Fig 6.2	The effect of AOD on CF for various atmospheric stability states associated with light rain a) 5-year data b) 10-year data c) 15-year data	60
Fig 6.3	The effect of AOD on CF for various atmospheric stability states corresponding to moderate rain a) 5-year data b) 10-year data c) 15-year data	61
Fig 6.4	The effect of AOD on CF for various atmospheric stability states associated with heavy rain a) 5-year data b) 10-year data c) 15-year data	62
Fig 6.5	The overall effect of AOD on CF and precipitation for light rain a) 5-year data b) 10-year data c) 15-year data (Regression equations for precipitation and CF are given in the upper and lower part of each figure, respectively)	65
Fig 6.6	The overall effect of AOD on CF and precipitation for moderate rain a) 5-year data b) 10-year data c) 15-year data (Note: Regression equations for precipitation and CF are provided in the upper and lower parts of each figure, respectively)	66
Fig 6.7	The overall effect of AOD on CF and precipitation for heavy rain a) 5-year data b) 10-year data c) 15-year data (Note: Regression equations for precipitation and CF are provided in the upper and lower parts of each figure, respectively)	67
Fig 6.8	Spatial distribution of AOD and CF in the light rain region for	69

cumulative data a) 5-year b) 10-year and c) 15-year

Fig 6.9 Spatial distribution of AOD and CF in the moderate rain region for Cumulative data a)5-year b)10-year and c)15-year 71

Fig 6.10 Spatial distribution of AOD and CF in the heavy rain region for cumulative data a)5-year b)10-year and c)15-year 72

Fig 6.11 Mean Precipitation of Extreme Precipitation Events (EPEs) in the Study Area for the Years 2018, 2019, and 2020 77

Fig 6.12 Spatial Distribution of Precipitation(mm), AOD, K-index(oC), CF, CTP (hPa) and CTT (oC) (Left to Right) for EPEs in Mumbai on a) May 25, 2018 b) Oct 4, 2018 c) Dec 3, 2019 d) May 31,2020 e) June 22,2020 f) Nov 19, 2020 78

Fig 6.13 Spatial Distribution of Precipitation(mm), AOD, K-index(oC), CF, CTP (hPa) and CTT (oC) (Left to Right) for EPEs in Chennai on a) June 11, 2018 b) Aug 20, 2018 c) Sep 20, 2018 d) June 10,2020 e) Oct 10, 2020 79

Fig 6.14 Spatial Distribution of Precipitation(mm), AOD, K-index(oC), CF, CTP (hPa) and CTT (oC) (Left to Right) for EPEs in Hyderabad on a) May 03, 2018 b) June 03, 2018 c) June 28, 2020 d) Oct 11, 2020 e) Nov 26, 2020 80

Fig 6.15 Spatial Distribution of Precipitation(mm), AOD, K-index (oC), CF, CTP (hPa) and CTT (oC) (Left to Right) for EPEs in Bengaluru on a) June 07, 2019 b) June 02, 2020. 82

Nomenclature

r	Correlation coefficient
R^2	Coefficient of determination
D_i	Mahalanobis distance
x_i	i^{th} observation
μ	Mean of observations
S	Covariance matrix
y_i	Observed value from AERONET
$\widehat{y_i}$	Predicted value from satellite/ model product
n	Number of observations
x_b	Observed value at time b
x_a	Observed value at time a
H_0	Null hypothesis
H_i	Alternative hypothesis
D	The trend indicator
X_n	Normalised data
X_{min}	Minimum value
X_{max}	Maximum value
hPa	Hecto Pascal

Abbreviations

ACP	Aerosol- Cloud-Precipitation
ADRF	Aerosol Direct Radiative Forcing
AERONET	AErosol RObotic NETwork
AOD	Aerosol Optical Depth
ATSR	Along Track Scanning Radiometer
AVHRR	Advanced Very High Resolution Radiometer
CALIPSO	Cloud-Aerosol Lidar and Infrared Pathfinder Satellite Observations
CARSNET	China Aerosol Remote Sensing Network
CCN	cloud condensation nuclei
CER	Cloud Effective Radius
CERES	Clouds and the Earth's Radiant Energy System
CF	Cloud Fraction
COR	Cloud Optical Radius
COVID	COronaVIrus Disease
CTP	Cloud Top Pressure
CTT	Cloud Top Temperature
ECMWF	European Centre for Medium-Range Weather Forecasts
EPE	Extreme Precipitation Events
FOV	Fields of View
GEOS-5	Goddard Earth Observing System Model, Version 5
GHGs	Green House Gases
HYSPLIT	Hybrid Single-Particle Lagrangian Integrated Trajectory model
IMD	Indian Meteorological Department
IMERG	Integrated Multi-satellitE Retrievals for Global Precipitation Mission
IPCC	Intergovernmental Panel on Climate Change

ITA	Innovative Trend Analysis
ITA-CB	Innovative Trend Analysis Change Box
LPA	Long-Period Average
LUT	Look Up Table
LWGNT	Surface Net Downward Longwave Flux
LWGNTCLN	Surface Net Downward Longwave Flux Assuming No Aerosol
LWTUP	Upwelling Longwave Flux at TOA
LWTUPCLN	Upwelling Longwave Flux at TOA assuming no aerosol
MAE	Mean Absolute Error
MERRA-2	Modern Era-Retrospective Analysis for Research and Applications
MISR	Multiangle Imaging Spectroradiometer
MK	Mann-Kendall
MLR	Multiple Linear Regression
MODIS	Moderate Resolution Imaging Spectro-radiometer
NASA	National Aeronautics and Space Administration
OMI	Ozone Monitoring Instrument
OMI	Ozone Measuring Instrument
RMB	Root Mean Bias
RMSE	Root Mean Square Error
SBDART	Santa Barbara DISORT Atmospheric Radiative Transfer
SCIAMACHY	Scanning Imaging Absorption Spectrometer for Atmospheric Cartography
SWGNT	Surface Net Downward Shortwave Flux
SWGNTCLN	Surface Net Downward Shortwave Flux Assuming No Aerosol
SWTNT	Net Downward Shortwave Flux
SWTNTCLN	Net Downward Shortwave Flux assuming no aerosol

TOA	Top Of the Atmosphere
TOMS	Total Ozone Mapping Spectrometer
VIIRS	Visible Infrared Imaging Radiometer Suite

CHAPTER 1

INTRODUCTION

1.1 General

Global and regional climate variability, which is caused by an increase in urban emission concentrations, is one of the main concerns in the current scenario. Airborne aerosols are found to be the primary reason in influencing the Earth's radiation budget. (IPCC 2013). Atmospheric aerosols have attracted a lot of scientific attention due to their significant influence on the radiation budget, cloud microphysical characteristics, and hydrological cycle (Ramanathan et al. 2005). Furthermore, aerosols have the potential to impact human health and visibility (Guo et al.,2018,2019), which makes it crucial to accurately study properties of aerosols.

The industrialization and increased mobility in major cities result in higher concentrations of aerosols in the atmosphere. The precipitation of high intensity and shorter duration has become evident in most of the metropolitan cities, leading to submergence and flooding in low-lying areas (Jasmine et al., 2022). Despite recent scientific advancements in numerical weather prediction capabilities, accurately forecasting Extreme Precipitation Events (EPE's) at a regional scale and with longer lead times remains challenging due to uncertainties produced by various sources (Mao et al., 2018).

1.2 Aerosol Optical Depth

The most used relevant satellite-derived parameter is Aerosol Optical Depth (AOD), as it is the most easily measurable and useful parameter. According to NASA, AOD is the measure of aerosols (e.g., urban haze, smoke. particles, desert dust, sea salt) distributed within a column of air from the instrument (Earth's surface) to the Top of the Atmosphere (https://earthobservatory.nasa.gov). The major natural and man-made aerosol types are

sulphate, nitrate, sea-salt, carbonaceous matter (organic carbon and black carbon), mineral dust. Out of them, sea salt, sulphates account for a significant portion of the global natural aerosol abundance whereas dust and soot are obtained from anthropogenic activities.

It is a fundamental optical parameter that quantifies the extinction effect of atmospheric aerosols, is frequently utilized to determine the level of air pollution. Aerosols have also been examined in studies on atmospheric radiation balance and climate change. Aerosols are capable of by affecting cloud microphysical properties, optical properties, the life cycle, sedimentation efficiency and radiation properties, which is called the indirect radiation effect. As a result, aerosols have a significant effect on the water cycles, atmospheric radiation transmission in local, regional, and even global climate (Srivastava et al.,2017).

The two main techniques for the long-term monitoring of aerosol properties are satellite remote sensing and ground-based observations. A global ground-based solar photometer observation network (AERONET) has been established by NASA to monitor the variability of atmospheric aerosols to observe its characteristics over an extended period. The space-borne earth observation satellites have been used to understand aerosol properties on a global scale which include Scanning Imaging Absorption Spectrometer for Atmospheric Cartography (SCIAMACHY), Ozone Monitoring Instrument (OMI), Along Track Scanning Radiometer (ATSR), Multiangle Imaging Spectroradiometer (MISR), Total Ozone Mapping Spectrometer (TOMS), Advanced Very High Resolution Radiometer (AVHRR), Moderate Resolution Imaging Spectro-radiometer (MODIS), UVN (UV–VISNIR) Spectrometer and Visible Infrared Imaging Radiometer Suite (VIIRS).

1.3 Direct Effect of Aerosols on Climate System

Solar radiation is a fundamental source of energy on Earth which is crucial for supporting the life and it drives many of the Earth's natural systems, including weather patterns, ocean currents, and the water cycle. However, the human activities, such as the emission of aerosols into the atmosphere, have affected the quantity of solar radiation that reaches the surface. The distribution of solar radiation by aerosols can cause a reduction in the amount of direct sunlight that reaches the surface, while the absorption of radiation by aerosols can increase the amount of thermal energy in the atmosphere. This is one of the main reasons for understanding the effect of aerosols on the Earth's climate is important. Human activities have the potential to alter the natural systems that sustain life on Earth by reducing the amount of solar radiation that reaches the surface (Liu et al., 2019, https://ceres.larc.nasa.gov/).

In recent years, the number of anthropogenic aerosols in the atmosphere are increased significantly due to economic growth (Sarangi et al., 2016). These aerosols absorb and scatter the incoming solar radiation, which can alter the Earth's radiation budget (Srivastava et al.,2017, Mao et al., 2022). The impact of anthropogenic aerosols on solar radiation is of great importance because it affects the energy balance and hydrological cycle (Yang et al., 2018, Kumar et al., 2019; Sridhar et al., 2018; Valayamkunnath et al., 2018). Aerosols can influence the radiative flux at the Top Of the Atmosphere (TOA) and even more significantly at the surface, which can impact biological processes (Setti et al., 2020; Sridhar and Anderson, 2017). While aerosols are found globally, their forcing effects are typically regional compared to the global forcing effects caused by greenhouse gases (GHGs) (Niyogi et al., 2007).

There are two main effects of aerosols on the weather and climate system. The direct effect is that aerosols affect the Earth's radiation budget is through the direct effect of scattering and absorbing radiation as shown in Fig 1.1a. In contrast to scattering aerosols (sulfate, nitrate, etc.), which increase the Earth's albedo and decrease the amount of solar radiation that reaches the Earth, absorbing aerosols (black carbon, mineral dust, etc.) decrease the Earth's albedo and heat the atmosphere, creating a greenhouse effect close to the Earth's surface. This leads the Earth-atmosphere system to cool indirectly. (Rajesh et al., 2019).

The Aerosol Direct Radiative Forcing (ADRF) is a measure of the effect of aerosols on radiative forcing. Generally, the global net radiative forcing due to aerosols is negative (IPCC 2013). The most widely used methods for estimating ADRF are the Moderate Resolution Imaging Spectrometer (MODIS) and the Clouds and the Earth's Radiant Energy System (CERES) clear-sky radiation fluxes, using the SBDART model. There are uncertainties in these estimates due to factors such as inhomogeneity, mixing state, vertical profile of aerosols, and the contribution of different aerosol species to ADRF (Subba et al., 2020).

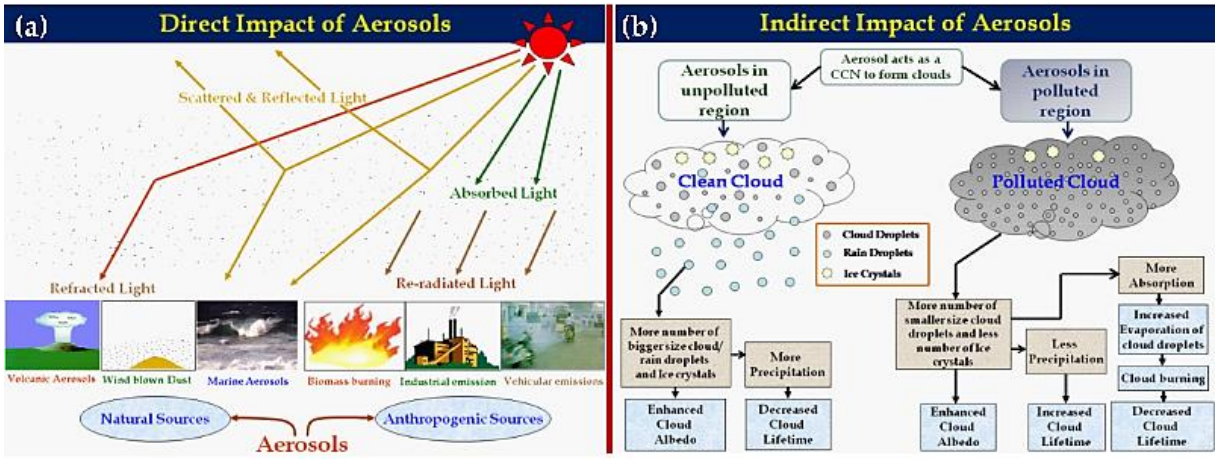

Fig 1.1: a) Direct Effect of Aerosols b) Indirect Effect of Aerosols on climate (Source: IPCC 2013)

1.4 Indirect Effect of Aerosols on Climate System

The indirect effect of aerosols is to impact the behavior of the clouds and increase the precipitation (Kant et al., 2019). The Aerosol–Cloud Precipitation (ACP) interaction is usually considered as an indirect effect of atmospheric aerosols in weather and climate perspectives. Because aerosols function as Cloud Condensation Nuclei (CCNs), variations in aerosol concentration can affect how well clouds precipitate, which in turn may result in variations in the quantity of cloud (Kant et al., 2019). The process of convective precipitation is suppressed mostly by collision process that reduces the size of cloud droplets. Consequently, delaying in the precipitation (downdraft) occurs resulting in the freezing of cloud droplets and thus leading to the release of latent heat causing more persistent and energetic updrafts.

Aerosols can influence cloud lifetime by influencing CCN and ice nuclei (Twomey 1977, Koren et al.,2010, Liu et al.,2020). The amount of water vapor gets distributed over many cloud droplets in the presence of large CCN concentrations. This results in smaller sizes of cloud, higher albedo (Twomey 1977), and less precipitation (Rosenfeld et al., 2008). The water supply and activation for convective clouds with a warm base originate in the warm region close to the cloud base. More latent heat is released when droplet condensation increases, which intensifies the updraft (Dagan et al., 2015; Pinsky et al., 2013; Seiki and Nakajima, 2014). As smaller droplets have smaller terminal velocity, they are lifted higher due to updrafts (Heiblum et al., 2016; Ilan et al., 2015). According to Rosenfeld and Woodley (2000), smaller droplets will freeze higher in the atmosphere, releasing the freezing latent heat into a comparatively colder environment.

As opposed to this, in low cloud fraction conditions, a high concentration of absorbing aerosols causes an aerosol semi-direct effect that inhibits cloud formation and, as a result, lowers surface rainfall (Ackerman et al., 2000; Koren et al., 2004; Rosenfeld, 1999). Accordingly, the net result of these conflicting aerosol effects on clouds is the aerosol–cloud associations that are observed over any given region as shown in Fig 1.1b (Koren et al., 2008; Rosenfeld et al., 2008).

The impact of aerosols on cloud lifetime and precipitation were extensively studied in recent years (Balakrishnaiah et al., 2012). Furthermore, the type of aerosols had a strong influence on the forcing phenomenon. For example, carbonaceous aerosols resulted in positive forcing whereas the sulphate aerosols resulted in negative forcings at the top of atmosphere (Grandey et al., 2013). The previous studies provided controversial results based on humidity and stability conditions in low and polluted regions (Remer et al.,2002, Koren et al.,2005).

Existing conditions in the study area such as biomass burning and anthropogenic emissions could result in such controversial results.

1.5 Research Motivation

The relationship between AOD, cloud and precipitation are highly challenging due to its intricacy. The prominent reason to choose this topic is climate change is an ever-challenging issue to cope up with the sustainability in the present scenario. The sudden change in the climate leads to extreme conditions and it is evident that lots of research is being carried out to know the reasons of prime importance resulting in such extremities**.** For the past 20 years, there has been a regular occurrence of extreme precipitation that has caused havoc in Southern India's major cities (TOI, Mumbai, 29 Sept 2019). This has led to analyze the impact of AOD on precipitation and temperature so that a clear understanding on the causes for the occurrence of extreme precipitation events are analyzed.

Most of the previous studies have concentrated on impact of AOD on climate system in Indo-Gangetic plains (Lau et al.,2016, Shreshta et al.,2017, Singh et al.,2018). Although the Southern India has different topography and climate regions, less research is carried out on this area. The Southern India has experienced an increase in the temperature and sudden downpour of rainfall over the past two decades (IMD annual report 2019). There is a need to study the impact of AOD on climate system of Southern India and this has motivated us to choose Southern India as area of interest to perform the present research work.

1.6 Aim and Objectives of the Study

The aim of the present research work was to understand the effect of AOD on precipitation and temperature in Southern India which helps in analysing the causes for extreme precipitation events. Based on the aim of research work, the objectives are framed which are as follows:

1. To assess the suitability of various satellite derived and model reanalysed Aerosol Optical Depth (AOD) products in the study area.
2. To analyse the influence of AOD on temperature using Aerosol Direct Radiative Forcing.
3. To evaluate the effect of aerosols on precipitation using atmospheric stability conditions.
4. To analyse the influence of AOD in causing extreme precipitation events in metropolitan cities.

1.7 Outline of the Thesis

This report is organized in seven chapters of this thesis report. The present chapter deals with Introduction of the work and formulated objectives. The review of literature is discussed in the Chapter 2. The methodology adapted for the entire research work and for each objective is discussed in Chapter 3. The results and discussions of validation and trend analysis is dealt in Chapter 4. The outcomes of analysis of AOD on temperature is dealt in Chapter 5. The Chapter 6 deals with the results corresponding to analysis of AOD on clouds and precipitation and the causes for the occurrence of EPE's in metropolitan cities of Southern India. The last chapter of the thesis deals with summary and conclusions of the research work.

CHAPTER 2

LITERATURE REVIEW

2.1 General

Based on the formulated objectives, the review of literature is carried out on validation of satellite data with ground truth data, trend analysis using Innovative Trend Analysis, AOD-Cloud-Precipitation interactions and AOD-Radiation diagnostics. The detailed explanation of the reviewed literature is given in the following sections.

2.2 Validation of Satellite and Model Re-analysis AOD with Observed Data

The necessity to validate the available satellite and model re-analysis AOD products with the observed data is to identify the suitable AOD product useful for a given area The following research works support the validation analysis.

Bibi et al. (2015) intercompared the AOD retrievals from MODIS (Moderate Resolution Imaging Spectroradiometer), MISR (Multi-angle Imaging Spectroradiometer), OMI (Ozone Measuring Instrument) and CALIPSO (Cloud-Aerosol Lidar and Infrared Pathfinder Satellite Observations) and validated them against the observed data from AERONET. They have performed the validation process on four sites for the data from 2007-2013. They converted AOD to the same wavelength for inter comparison using angstrom exponent. They used statistics like Root Mean Square Error (RMSE), Mean Absolute Error (MAE), Root Mean Bias (RMB) and expected error bound to validate the products. They concluded that MODIS standard retrievals were in good agreement with AERONET over bright surfaces and MISR retrievals were good at coastal areas. The MODIS deep blue algorithm and OMI retrievals were found in reasonable agreement with AERONET data.

Alyson and Aggarwal (2018) validated MODIS collection 6 AOD Dark Target product with combinations of Terra and Aqua platforms against two validation sites in Alaska for a period of 14 years from 2000-2014. Linear regression between MODIS AOD and AERONET AOD was performed using ordinary least squares equation. The correlation coefficient was in the range of 0.85-0.93 for different products. MODIS datasets were found to have negative bias at both 10-km and 3-km resolutions. Finally, it was concluded that all products show validity between April to October months.

Carlos et al. (2018) reported a comparison of MODIS retrieved AOD and AE with ground observations at an installed sun photometer site in Cuba for data from 2008 to 2014. All the three MODIS products i.e Dark Target, Deep Blue, combined dark target and deep blue were compared with the photometer observations. The statistics like RMSE, MAE, Bias were used to validate the products.

Vijaykumar et al. (2018) performed regression analysis between MODIS Terra and Aqua AOD, ECMWF reanalysis product and ground observations taken from AERONET station at Pune. The Terra, Aqua and reanalysis product underestimates the AOD at 550nm wavelength when compared to AERONET observations. The ECMWF overestimated the precipitable water content while others under estimated when compared to ground measured observations. Seasonal analysis shows that the MODIS AOD products are underestimated in the monsoon season while PWV values were under estimated by AERONET observations in the monsoon season. The RMSE and MAE was higher for Terra products and lower for reanalysis product.

Che et al. (2019) performed long term validation of MODIS C6 and C6.1 dark target aerosol products over China using CARSNET and AERONET. The MODIS C6 and C6.1 represent the 6 and 6.1 of aerosol data by Dark Target (DT) and Deep Blue (DB) algorithms. The performance of C6 data from DT algorithm was poor in some of the land areas globally. Hence, the algorithm was improvised and C6.1 data was released. The results showed that the C6.1 products performed better when compared to C6 products with higher correlation and lesser deviation of root mean bias from 1. The performance of C6 dark target algorithm retrievals was poor in urban areas when compared to C6.1 product. Also, there was an over estimation of AOD by 19% using C6 algorithm. The new reflectance scheme incorporated in C6.1 has less influence on AOD retrievals in China because of vegetation cover. The authors concluded that the C6.1 products performed better statistically.

Ogunjobi et al. (2019) correlated MODIS (Dark Target and Deep blue), MISR aerosol products with AERONET observations at six locations in West Africa. The Dark target product showed high correlation because of low vegetation cover while MISR product had higher correlation near oceans. The MODIS deep blue and CALIPSO retrievals were moderately correlated with ground observations. The seasonal analysis shows that the AOD was higher in December-January-February and March-April-May seasons due to North-easterly winds in Sahara desert.

Anoruou et al. (2022) correlated the MODIS AOD and Angstrom Exponent (AE) against the ground observations from AERONET during monsoon season over 7 sites in Italy. They used standardized anomaly and the standard deviation ratio method of analysis to address the robustness of AE for further classification of type of aerosols. The correlation was 0.95 for MODIS AOD. The AERONET and MODIS AODs' standardized anomaly records (-0.22 ± 0.13) in June had a corresponding correlation of ($r = 0.96$).

Gupta et al. (2022) compared the satellite and ground observations of AOD globally for a period of 20 years. They have used statistical measures for comparison. They have observed that all the satellite observations taken from MODIS Aqua and Terra platforms, MISR have a high spatial correlation (above 0.7) with AERONET. The observations from CALIOP overestimated the AOD across the high aerosol loaded regions.

2.3 Trend Analysis Using R Statistical Software

The AOD is dependent on anthropogenic emissions in a given region. With increase in urbanization, emissions might also increase. Thus, it is essential to observe trend in AOD. The following research studies discuss trend analysis on AOD and rainfall using non parametric tests.

Maghrabi and Alotaibi (2018) analysed AOD at 500nm wavelength from 1999-2015 in Arabian Peninsula. Annual, monthly, seasonal and hourly trends were studied and supported by Mann-Kendall test at different significance levels. It was concluded that trend in spring season is highly significant. Similarly significant increasing trends were observed in March, April, June, and December. It was also observed that early mornings and late afternoons have increasing trend during the study time period.

Caloiero et.al (2018) investigated temporal rainfall in Southern Italy with 559 rain gauges, consisting of 50 years of observed data. Trends in seasonal, annual rainfall was evaluated using graphical technique proposed by Sen called as Innovative Trend Analysis for low, medium and high values of series. In addition to that Mann-Kendall test was also performed.

The results obtained by ITA were in accordance with MK test. It was concluded that ITA method has some advantages over MK test in terms of details of evaluation for each categorical value.

Alashan (2018) proposed an Innovative Trend Analysis Change Box (ITCA-CB) approach by considering quantitative changes in two halves of time series of data. ITA is used to observe monotonic increasing or decreasing trends whereas ITA-CB approach is used to detect trend in non-parallel points which are further divided into low, medium and high groups for accurate interpretations. For each half of time series, statistical minimum, average and maximum changes for each group are evaluated and box plots are created for each group. Finally, it was explained that presence of negative trend is confirmed if mean line is close to minimum change and vice versa.

Caloiero et.al (2020) performed Sen's ITA on Calabria region of South Italy**.** The region was divided into five homogenous climate zones (RZ) based on principal component analysis. The first five components explained about 90% variance in the climate of the selected study area. The precipitation data in those five RZ's were collected for the period of 90 years (1916-2006). The annual trend of the rainfall anomalies showed a negative trend of the highest values. The seasonal analysis displayed a negative trend for the lowest values and a positive one for the highest values in the winter season. The results were compared with MK test and concluded that ITA is advantageous in terms of evaluating the different values of precipitation.

Roudbari et.al (2020) evaluated the spatio-temporal variability and trend in AOD using MODIS onboard Terra and Aqua satellite data over Iran. The purpose of their study was to detect aerosol hotspots and identify the seasonal trend using Mann-Kendall test. There was an increasing trend in autumn season accompanied by reduced precipitation. There was a massive decreasing trend in AOD over western Iran during winter. The trends were not significant during the time period of 2003-2017.

Mohammed et al. (2022) assessed the trend in AOD from MODIS over Jharkhand for a period of 18 years (2000-2017). They have used Mann-Kendall method and Sen's slope estimator method to analyse the trend in AOD. All the major cities of the state exhibited a notable positive trend in AOD by two methods. Pre-monsoon season observations showed that Sahibganj had the highest upward trend while Gumla had the lowest. Three periods were identified in the temporal variation of aerosol trends: 2000–2005, 2006–2011, and 2011–2017. These periods have exhibited a low positive trend in AOD towards west and south-west region while high trend was observed towards north-eastern border.

Yousefi et al. (2023) analysed the trends in winter AOD in Iran during 2000-2018 by least square method. The analysis revealed a significant trend over the dusty regions of Iran. The primary determinants of dust transport and atmospheric circulation patterns were wind direction and speed, which also showed a positive correlation with AOD. Winter AODs and dust emissions were linked to increased cyclones over the Middle East between 2000 and 2010, which was further aided by declining trends in precipitation and relative humidity as well as rising trends in temperature over the main dust sources in Iraq and southwest Iran. In contrast, the deceasing trend in AOD was associated with increase in rainfall and relative humidity during 2010-2018 over western part of Iran.

2.4 Effect of Aerosols on Temperature

Aerosols can modify the Earth's radiation budget and create an imbalance between inward and outgoing solar radiation. This results in net heating or cooling of the atmosphere. The following section discusses a few studies that support the idea of AOD affecting the temperature.

Penna et.al (2018) estimated the ADRF using MERRA-2 reanalysis products. They used two methods to calculate the ADRF. Procopio et al. (2004) developed the first method (M1), which uses AOD as a function to give ADRF via a two-degree linear equation. The equation works well in areas with a lot of vegetation, like the Amazon. The second method to calculate ADRF is using MERRA-2's net shortwave and longwave fluxes (M2). The AOD is considered in M1, but it is not included in M2, hence the Radiative Forcing (RF) by M1 and M2 are different. They have concluded that seasonal and decadal forecasting can be done with the M2. Understanding the effects of aerosols on the atmosphere requires a deeper examination of sensible and latent fluxes.

Shreshta et.al (2018) have developed a multiple regression model to compute ADRF in the Indo-Gangetic basin. The MODIS AOD and water vapour products were used to develop the model and the validation was performed using AERONET data available at 10 stations in the basin. The R^2 value for the developed model when performed on annual scale was 0.84 whereas the seasonal scale R^2 is in the range of 0.81-0.83. The stability of the developed model was tested by Jackknife method which deletes one station data at once and check the R^2. Also, the model developed ADRF was compared at Karachi and Lahore with the ADRF from SBDART taken from Alam et.al (2012) and found the statistics are in accordance with SBDART.

Feng et.al (2019) evaluated the effect of aerosol forcing on global temperature using satellite observations. Multiple regression analysis was performed for the framework that is designed

on the budget laws. The negative forcing was observed in North America and Western Europe whereas positive forcing was observed in South Australia. It was observed that enhancement of global warming is due to changes in aerosol forcing. Finally, it was concluded that multiyear mean of aerosol forcing has an increase of 0.005 K of surface temperature.

Kumar et.al (2019) examined aerosol characteristics and short-wave radiation in New Delhi from March 2010 to June 2012. The relationship between AOD and solar radiation was observed for different sky conditions like clear sky, haze/fog, dusty and cloudy sky days. However direct radiation forcing efficiency was obtained from the slope of best fit line between mean AOD and solar radiation. It was inferred that the relative cooling was more in dusty days accompanied by enhanced AOD and reduced Angstrom exponent values.

Pandey et.al (2020) studied the effect of aerosols in the Indo-Gangetic plains over the sub-weekly means compared against the weekends. The weekday means are 20% higher than that of the weekend means. The cloud macro-physical properties such as cloud optical depth and liquid water path were found to decrease at a significant level. The cloud effective radius did not show a significant change due to the narrow period of dataset. The shortwave cloud radiative effect at TOA and surface was in the range of 7-10% whereas the longwave radiative effect was double that of the shortwave effect. Thus, it was concluded that aerosol loading observed over a small time period can also influence the cloud properties.

Subba et.al (2020) analysed the trends in ADRF under clear sky conditions using satellite measurements over the period 2001-2017. They used CERES products to calculate ADRF under clear sky conditions. The trend was found to be decreasing at TOA and surface globally. The regional analysis shows that the atmospheric radiative forcing is decreasing in North America and Western Europe. There was a slight increasing trend in Africa and South Asia. The global distribution of AOD reveals that the loading in more in central and Eastern India, Africa. Thus, they concluded that the changes in ADRF is due to the emissions of anthropogenic aerosols.

Li et.al (2023) analysed the effect of brown carbon aerosols on temperature and precipitation. Brown Carbon heating causes tropical expansion and a decrease in deep convective mass fluxes in the upper troposphere. They have observed a clear shift in cloud fraction, liquid water path and precipitation with the inclusion of brown carbon in the models. On the other hand, the inclusion of brown carbon in climate models led to increase in temperature and precipitation on a global scale but vice-versa on a regional scale.

2.5 Impact of AOD on Cloud Fraction and Precipitation

Aerosols primarily act as cloud condensation nuclei and influence the cloud formations. The cloud microphysical properties are also susceptible to changes with variation in aerosol concentrations. The aerosol loading indirectly affects the precipitation efficiency because of its effect on cloud parameters. The literature related to the AOD-cloud-precipitation interactions are given below.

Adesina et.al (2014) studied the impact of aerosol-cloud-precipitation interactions in major cities of South Africa using MODIS data for a period of 10 years from January 2004 to December 2013. The spatial and temporal variations of AOD were found to be less significant in most of the stations considered for analysis. Although the relationship between AOD and Angstrom Exponent was strong enough in four of the six stations considered for the analysis. Other cloud parameters like cloud effective radius, cloud fraction and cloud top temperature were found to be negatively correlated with AOD.

Kang et.al (2015) evaluated the impact of aerosols on cloud formation by studying the correlation between AOD and cloud properties. Their findings showed that the AOD was high at low latitudes and vice versa over 12 major cities of China because of slant trajectories taken up by aerosol masses. The correlation between AOD and cloud fraction was low at urban regions than that of the coastal regions. Also, the CF was negatively correlated to AOD in the regions when AOD was lower than 0.3. The Cloud top temperature was also negatively correlated to the aerosol loading but the cloud effective radius was positively correlated to AOD over China. Further, the authors have concluded that the necessity of meteorological parameters in the regression analysis helps to understand the aerosol-cloud-precipitation interactions in an explicit manner.

Cheng et.al (2017) analysed the aerosol-cloud-precipitation interactions in central-eastern China using MODIS collection 5 data during 2000-2012. The results of the analysis were categorized into four patterns based on correlation values. Firstly, in the region where AOD is negatively correlated to Cloud Effective Radius (CER) but CER is positively correlated to precipitation validates the indirect effects of aerosols. Secondly in the region where AOD is negatively correlated to CER and CER being negatively correlated to precipitation implies that with an increase in AOD, there will be decrease in CER and further increase in precipitation. Thirdly in the region where AOD is positively correlated to CER and CER being positively correlated to precipitation implies that with increase in AOD, CER increases and results in accumulation of moisture along with CCN. This formation will further result in downpour of rainfall. Lastly in the region where AOD is positively correlated to CER and

CER is negatively correlated to precipitation infer that CER increases with increase in AOD but there will be reduction in precipitation. Finally, the authors deduced that the interactions have varied results in southern and northern part of study area considered during different seasons.

Kant et.al (2019) analysed the role of aerosols in governing the cloud properties is analysed through cloud optical depth for Odisha and Bhubaneswar during convective driven precipitation period. The probability at 95% confidence level was characterized by student's t-test technique. Aerosol-cloud-precipitation relationship was analysed by taking AOD, Cloud Optical Radius (COR), CER and rainfall into consideration. From the study it was observed that the near surface temperature is high during pre-monsoon season resulting in agglomeration of aerosols. Finally, the authors concluded that though AOD-Cloud Optical Depth (COD) variance is low in the study region, AOD-rainfall relationship was stronger.

Liu et.al (2020) studied the effects of meteorological conditions on the relationship between AOD and macro-physical properties of the warm clouds over Shanghai region of China. The low warm clouds were identified based on the properties of cloud top pressure and cloud top temperature. The authors found that the AOD is negatively related to cloud fraction due to the presence of absorptive aerosols in the atmosphere. They concluded that the effect of atmospheric stability on horizontal and vertical distribution of clouds was higher than that of the aerosols. The effect of aerosols was predominant when the atmosphere was stable and vice versa.

Salman et.al (2020) evaluated the aerosol-cloud-precipitation interactions over Iraq during the period 2008-2017. They used MODIS and HYSPLIT data to understand the effect of aerosols on macro-physical properties of clouds. The AOD has shown a negative correlation with COR, cloud fraction and positive correlation with CER and water vapor content. The trajectories analysed from HYSPLIT shows that the air masses are originated from west especially from Mediterranean Sea.

Eirund et.al (2022) investigated the impact of aerosol concentrations on surface precipitation using Consortium for Small-scale Modeling (COSMO) model. In contrast to the impact of the microphysics scheme, simulated variations in surface precipitation in response to aerosol perturbations continue to be modest. Increased cloud water and decreased cloud ice mass are caused by elevated concentrations of Cloud Condensation Nuclei (CCN), particularly in areas with significant convective activity south of the Alps. They also observed that further downstream, these modified cloud features result in more surface precipitation.

2.6 Analysis of the Causes for Occurrence of EPE In Urban Cities

There is an increasing trend in occurrence of EPE in urban cities according to the previous researchers. Some of the literature corresponding to EPE are discussed below.

Gryspeerdt et.al (2014) investigated that in high-aerosol environments, there is little effect on precipitation at the time of aerosol retrieval. They found that there was an increase in precipitation from cloud in the six hours that follow, which was consistent with the invigoration hypothesis. The authors detected that the invigoration effect was temperature-dependent, with CTT<0^{o}C. They concluded that the development of precipitation in warm clouds did not change much with an increase in aerosol concentration, which indicated the importance of ice processes in reviving precipitation.

Jasmine et.al (2018) confirmed the occurrence of higher altitude dust transport during heavy precipitation days and even before that, from the arid gulf region towards the Arabian Sea and near the Kerala coast, using CALIPSO aerosol vertical profiles, the OMI Absorbing Aerosol Index, and the HYSPLIT back trajectory analysis. AOD variations over the period together with changes in cloud properties such as Cloud Fraction (CF), Cloud Top Temperature (CTT), Cloud Water Liquid Water Path (CWLWP), and Cloud Condensation Nuclei (CCN) amply demonstrate the close relationship between aerosols and cloud properties over the region.

Choudhary et.al (2020) studied 17 years of rainfall, AOD and meteorological conditions that resulted in high precipitation at the foothills of Himalayas. Their findings show that strong and distinct correlations were observed between high aerosol loading, high moist static energy values, and high precipitation events. They concluded that average increase in low-level moist static energy (1000–850 hPa) and the average increase in AOD is 36% resulted in high precipitation events.

Wang et.al (2022) reviewed the role of atmospheric aerosols in extreme meteorological events. They have concluded that the aerosols can suppress the precipitation from low stratiform clouds and enhancing the precipitation and leading to floods in local areas due to invigoration effects. They have observed that strong convection and exceptionally heavy rainfall are produced by the orographic lifting of humid air mass under the influence of topography.

2.7 Critical Appraisal of Reviewed Literature

The recent literature related to the validation of satellite, model re-analysis AOD with ground truth data, trend in AOD using MK and ITA tests, aerosol-cloud-precipitation interactions, aerosol-radiation diagnostics are discussed in this chapter. Numerous satellite derived products provide columnar AOD for any region on the surface of the Earth. The validation of products with ground network helps to recognise the suitable product for the chosen study area. Most of the reviewed literature (Humera et al.,2015, McPhetres and Aggarwal 2018, Vijaykumar et al.,2018, Cheng et al.,2019) use linear regression and statistical analysis to select the data. In the present research work, an automatic method is developed by using R statistical software to fit a regression equation between satellite and ground observed data.

The trend in AOD helps to understand the accumulation in the atmosphere over the years. The trend is generally analysed by the conventional MK test. In the recent scenarios, ITA has gained importance because of its ability to ignore serial independency of the data and less importance to the distribution followed by the data. Also, the ITA has categorised the values into low, medium and high which is explicit on 1:1 plot of the data. Most of the researchers (Caloiero et al.,2020, Roudbari et al.,2020) have performed ITA on station data and have shown the trend in the form of 1:1 line plot.

The aerosol-radiation diagnostics is the direct effect of aerosols in the atmosphere. Most of the preceding researches have carried out analysis on interaction of aerosol with the net radiation in the atmosphere by using ADRF under clear sky conditions. The ADRF considered in the past works was mostly from CERES atmospheric data (Feng et al., 2019, Kumar et al.,2019, Pandey et al.,2020, Subba et al.,2020). In the current research, an attempt has been made to calculate ADRF under all-sky conditions using MERRA-2 reanalysis data. Also, the effect of aerosols on temperature based on the calculated ADRF is analysed for the normal years and pristine situation obtained in the lockdown of 2020 due to COVID pandemic.

The concentration and distribution of AOD is useful for analysing the effects of aerosols on the climate variables. The impact of aerosols on the formation of clouds is considered as the indirect effect of aerosols as they can act as CCN. Mere correlation analysis between AOD and cloud fraction does not help in understanding the interaction phenomenon properly (Adesina et al.,2016, Cheng et al., 2017, Kant et al., 2019). The indulgence of meteorological factors in the analysis helps to perform analysis effectively. The previous researchers have considered Water vapour and K-index as the suitable factors for correlation analysis. The

amount and vertical extent of low-level moisture in the atmosphere, along with the vertical temperature lapse rate, are the two factors that determine the thunderstorm potential measured by the K-index. In general, the likelihood of heavy rain increases with K-index values. However, heavy precipitation can occur under low moisture conditions due to a suitable lifting mechanism of unstable air.

The existent research is carried out on the same lines by considering K-index as the meteorological factor for performing correlation between aerosols and cloud fraction over the cumulative years.

CHAPTER 3
METHODOLOGY

3.1 General

Based on the aim and objectives of the research work, the overall methodology is proposed and it is explained in four parts of this chapter. The aerosols can alter the precipitation and temperature in each area. To study the effect of aerosols, it is required to have a satellite product with high resolution. The satellite and model reanalysis data are validated against the ground observations to identify the suitable AOD for the study area. The innovative trend analysis is applied for the raster data by using R statistical software. The AOD-radiation interactions are helpful to understand the influence of aerosols on temperature. The detailed study on AOD-cloud-precipitation interactions in the research was taken up in the study area. The influence of AOD in causing the extreme precipitation events is analysed.

3.2 Study Area

The current study focused on the terrestrial region of Southern India, which consists of nine states: Maharashtra, Orissa, Chhattisgarh, Goa, Andhra Pradesh, Telangana, Karnataka, Tamil Nadu, and Kerala. It has been found that the entrapment of aerosols in the atmosphere has increased in recent years, leading to a delay in the onset of the south-west monsoon season, which is a major source of rainfall in the region. Agriculture is the primary economic source in this region, while income from small and medium scale industries is the secondary source of livelihood for many people.

1

2

The terrestrial region of Southern India is situated in area of 1239 lakh ha. Nearly 40% of India's population lives in the chosen study area. The area is bound by Indian ocean to the South, Bay of Bengal to the East, Arabian Sea to West, Vindhya and Satpura region to the North. The geography of the study area comprises Deccan Plateau, Western and Eastern ghats. As shown in Fig 3.1, the study area is divided into five different climatic zones according to Koppen's Classification: monsoon climate (Am), tropical savanna climate (Aw), warm semi-arid climate (BSh), humid subtropical climate (Cwa), and subtropical oceanic highland climate (Cwb). The region of tropical monsoon climate (Am) has a mean temperature greater than 18^0C in every month of a year. In this region, the driest month has an average precipitation of less than 60mm but more than precipitation in Eq (3.1).

$$\text{Precipitation} = 100 - \frac{Total\ Annual\ Precipitation\ (mm)}{25} \qquad -(3.1)$$

The tropical monsoon climate regions have less variations in temperature. The metropolitan city of Kochi and Goa comes under Am region. The driest month of tropical savanna climate (Aw) region experiences an average precipitation less than 60mm and also less than the precipitation in Eq (3.1). The dry season is most pronounced in tropical savanna climate region. The cities of Mumbai, Chennai and Bengaluru comes under Aw climate region. The warm semi-arid climate (BSh) sees hot to extremely hot summers and warm to cool winters. The mean annual temperature in this region is 18^0C. The city of Hyderabad is in BSh climate region. The humid subtropical climate (Cwa) region witnesses an average precipitation in the range of 80-165cm. The region has a mean temperature in between 0^0C to -3^0C in the coldest month and greater than 22^0C in the warmest month. Raipur comes under Cwa climate region. The sub-tropical oceanic highland climate (Cwb) region tend to have dry winters and wet summers (Kottek et al.,2006). The climate zone of Coimbatore is Cwb. The Koppen's classification is shown in the Fig 3.1.

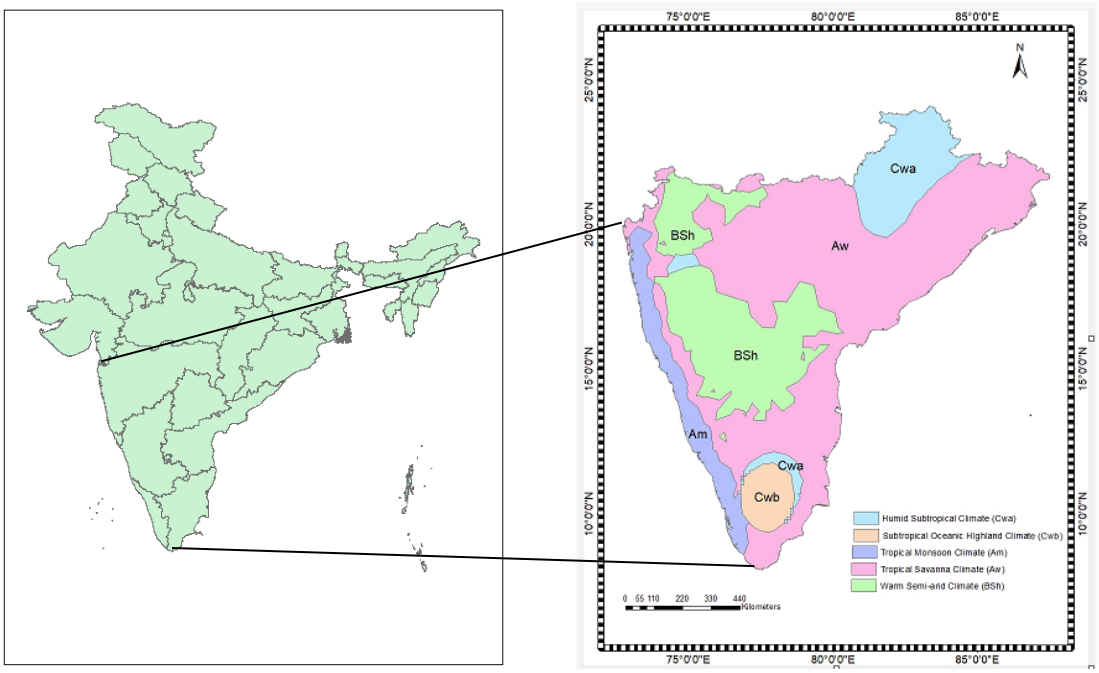

Fig 3.1: Location map of Study Area with Koppen's Climate Zones

3.3 Data Used in the Study

The data required for the current study consists of various parameters from different satellites. The spatial data consists of AOD data from Moderate Resolution Imaging Spectrometer (MODIS), Ozone Measuring Instrument (OMI), Modern Era-Retrospective Analysis for Research and Applications (MERRA-2). The multi satellite precipitation product comes from the Integrated Multi-satellitE Retrievals for Global Precipitation Mission (IMERG). The radiation fluxes used in this study are obtained from MERRA-2. The temperature data is taken from Indian Meteorological Department (IMD). The source and resolution of datasets used in the study is shown in Table 3.1.

3.3.1 MODIS Data Products

The datasets used for the current study are obtained from the MODerate Resolution Imaging Spectrometer (MODIS) on board Terra and Aqua Satellites. MODIS products are widely used for a variety of analyses due to their broad spectral coverage and high spatial resolution (Liu et al., 2020). The observation period constituted the monsoon season from 2005 to 2019. All three products were obtained from the NASA website. Details of the data products used in the present study are given as follows:

Table 3.1: Details about the satellite data, parameters, and spatial resolution used in this study

S.No	Source of AOD	Parameter	Spatial Resolution
1	Moderate Resolution Spectrometer (MODIS) Terra (MOD04_L2) (https://ladsweb.modaps.eosdis.nasa.gov/)	Optical Depth Land and Ocean	10kmX10km
2	Ozone Monitoring Instrument (https://aura.gsfc.nasa.gov/)	Near UV Aerosol Optical Depth	$1^{o}X1^{o}$
3	Modern Era-Retrospective Analysis for Research and Applications (MERRA-2) (https://gmao.gsfc.nasa.gov/)	Hourly Aerosol Optical Depth	$0.5^{o}X0.625^{o}$
4	Moderate Resolution Spectrometer (MODIS) Terra (MOD06_L2) (https://ladsweb.modaps.eosdis.nasa.gov/)	Cloud Top Pressure (CTP)	1kmX1km
5	Moderate Resolution Spectrometer (MODIS) Terra (MOD06_L2) (https://ladsweb.modaps.eosdis.nasa.gov/)	Cloud Top Temperature (CTT)	1kmX1km
6	Moderate Resolution Spectrometer (MODIS) Terra (MOD06_L2) (https://ladsweb.modaps.eosdis.nasa.gov/)	Cloud Fraction (CF)	1kmX1km
7	Moderate Resolution Spectrometer (MODIS) Terra (MOD07_L2) (https://ladsweb.modaps.eosdis.nasa.gov/)	K-index	5kmX5km
8	GPM IMERG Final Precipitation L3 (GPM 3IMERGDF)	Precipitation	10kmX10km
9	Modern Era-Retrospective Analysis for Research and Applications (MERRA-2) (https://gmao.gsfc.nasa.gov/)	Radiation Flux	$0.5^{o}X\ 0.625^{o}$
10	IMD Temperature Data	Temperature	$1^{o}X1^{o}$

MOD04_L2: It denotes the aerosol product generated by the dark target/deep blue algorithm. The parameter used is Optical Depth Land and Ocean and the spatial resolution is 10kmX10km. MODIS aerosols retrievals are based on a Look Up Table (LUT) procedure in which satellite-measured radiances are matched to pre-calculated values in the LUT and the values of the aerosol properties used to create the calculated radiances are retrieved (Vijaykumar et al., 2018). The estimated satellite radiances at 470 and 670 nm wavelengths are used to calculate AOD at 550 nm using the Angstrom exponential law. The satellite product is validated against ground truth data, and the results are satisfactory. The algorithm of MOD04_L2 product has three quality flags for obtaining AOD. The quality flag of '0' indicates bad, '1' indicates marginal, '2' indicates good and '3' indicates 'very good'. The product used for the research has a quality flag '3' for land. For retrieval in fog and cloud dominated sites, MODIS uses lookup table approach to match the fine mode fraction and coarse mode fraction of the AOD.

MOD06_L2: It refers to cloud data. The macro-physical cloud parameters used in the study are Cloud Top Pressure (CTP), Cloud Top Temperature (CTT) and Cloud Fraction (CF). The three parameters are all measured with a spatial resolution of 1kmX1km. CTP and CTT are measured using infrared and CO_2 absorption bands, respectively, whereas CF is collected using visible bands (Platnick et al., 2015).

MOD07_L2: It denotes the atmospheric profile data. From this the K-index parameter data is used. It is a measure of thunderstorm potential based on vertical temperature lapse rate, lower atmosphere moisture content, and the vertical extent of the moist layer. The temperature difference between 850 hPa and 500 hPa is used to parameterize the vertical temperature lapse rate. The dew point at 850 hPa indicates the moisture content of the lower atmosphere. The vertical extent of the moist layer is represented by the difference of the 700 hPa temperature and 700 hPa dew point. This is called the 700 hPa temperature-dew point depression. The index is derived arithmetically. MODIS satellite provides K-index at 5km spatial resolution when at least 9 Fields of View (FOV) are clear (Borbas et al., 2015). The k-index is shown in Eq (3.2)

$$K = (T_{850} - T_{500}) + T_{d_{850}} - (T_{700} - T_{d_{700}}) \quad \text{-(3.2)}$$

Where T_{850} is temperature at 850 hPa, T_{500} is temperature at 500 hPa, T_{700} is temperature at 700 hPa, $T_{d_{850}}$ is dew point temperature at 850 hPa, $T_{d_{700}}$ is dew point temperature at 700 hPa.

3.3.2 Precipitation Data

The multi satellite precipitation product comes from the Integrated Multi-satellitE Retrievals for Global Precipitation Mission (IMERG). This dataset is the GPM Level 3 IMERG Final Daily 10 km x 10 km (GPM_3IMERGDF) derived from the half-hourly GPM_3IMERGHH. The derived result represents the final estimate of daily accumulated precipitation. PrecipitationCal, also known as complete calibrated precipitation, is the parameter used in this study. It displays the daily accumulated precipitation in millimetres.

3.3.3 Radiation Flux Data

The radiation fluxes used in this study are obtained from the Modern-Era Retrospective analysis for Research and Applications (MERRA-2), a NASA atmospheric reanalysis that began in 1980. This reanalysis has been upgraded using the Goddard Earth Observing System Model, Version 5 (GEOS-5) data assimilation system, and has replaced the original MERRA

reanalysis (Rienecker et al., 2011). The net shortwave and longwave fluxes are found in the M2T1NXRAD_5.12.4 data set of MERRA-2, and are at a resolution of 0.5° × 0.625°.

3.3.4 Temperature Data

High-resolution temperature datasets allow for the analysis of extreme climate conditions from the past. One such dataset is provided by the India Meteorological Department (IMD), Pune, India. The IMD operates 550 observatories where daily maximum and minimum surface air observations are recorded. These observations are then processed using Shepard's angular distance weighing algorithm and converted into 1° x 1° gridded locations. The IMD currently offers data from 1969 to 2020 (Srivatsava et al., 2009).

3.3.5 AERONET

The ground observations for AOD is obtained from various sun photometer sites of Aerosol Robotic Network (AERONET). It is a global ground-based network of automatic sun photometers that measure direct radiances at several wavelengths (Holben et al., 1998). AOD is obtained from direct sun measurements with an accuracy to within ±0.015 (Buchard et al.,2015). The AERONET sun photometer makes direct spectral solar radiation measurements at 440, 670, 870 and 1020 nm wavelengths. The instrument is calibrated annually to ensure accuracy in measurements. As satellite derived AOD product is obtained at 550nm wavelength, the ground observed AOD at 440 and 670 nm wavelength is interpolated using Angstrom exponent law to obtain AOD at 550 nm wavelength.

3.4 Overall Methodology

Present research work was to study the impact of aerosols on the precipitation and temperature on the terrestrial region of Southern India. The overall methodology is shown in the Fig 3.2. The first step of the methodology was to select a suitable satellite AOD product which helps to study the impact of aerosols in the study area. The satellite product selected based on the statistical validation with ground observations. The second step was to find the trend in AOD for the past two decades. It was executed by the Mann-Kendall test and Innovative Trend Analysis. The lockdown period due to COVID-19 pandemic had led to a pristine situation where the emissions were minimum from the industries. Hence, the Aerosol-radiation-Interactions were compared between the average of 2015-2019 and 2020 for three different timescales namely pre-lockdown (Jan 1 to Mar 23), lockdown (Mar 24 to May 31) and post-lockdown (Jun 1 to Aug 31). The fourth step was to observe the influence of aerosols on cloud fraction and precipitation for each of the instability states in the atmosphere. The Aerosol-Cloud-Precipitation analysis was performed for the past cumulative 5,10 and 15

years of data. The final step was to assess the causes for occurrence of extreme precipitation events in and around metropolitan cities.

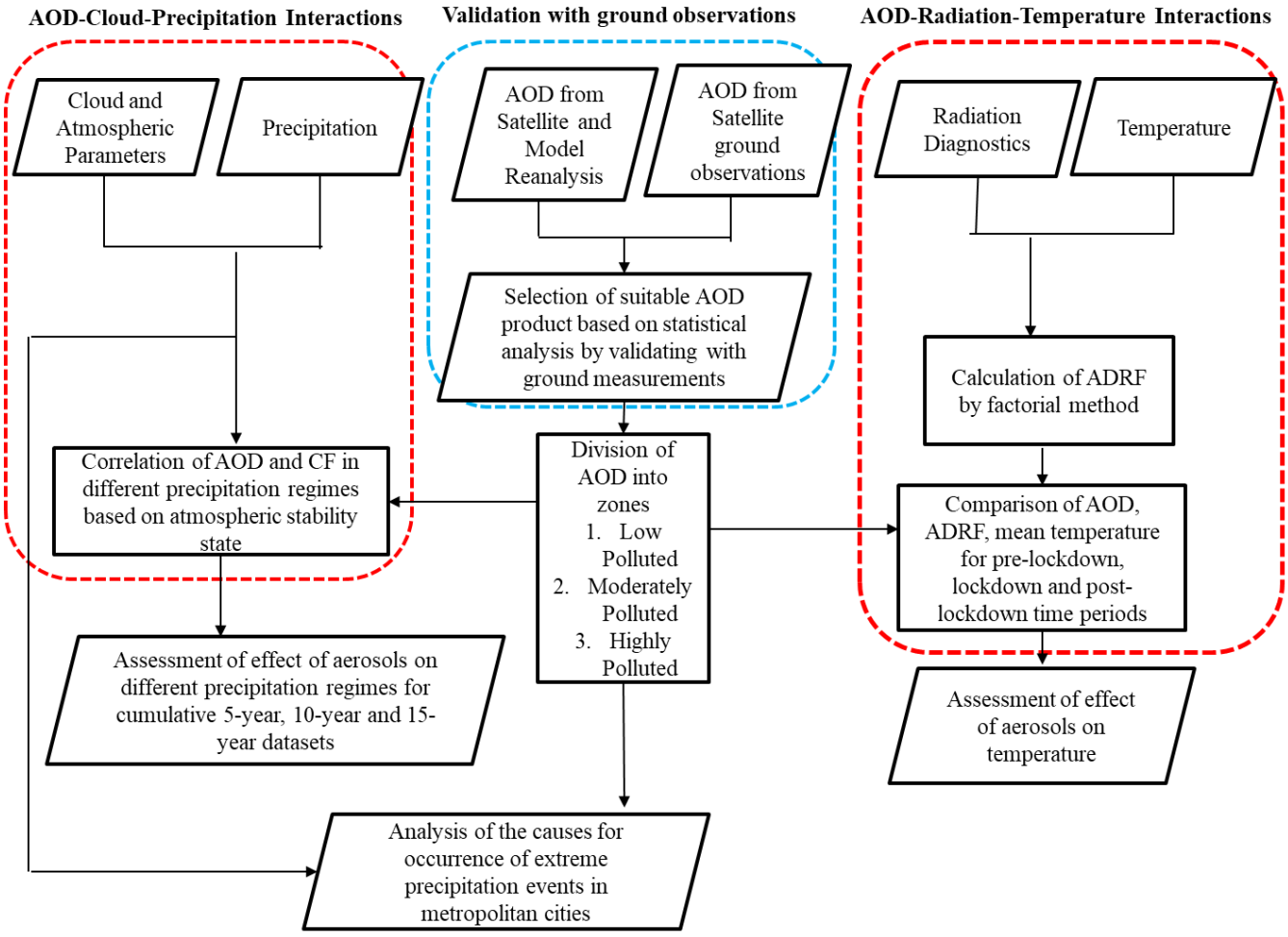

Fig 3.2: Overall Methodology for the Present Study

3.5 Validation of Various Satellite Derived AOD Data with Ground Observations

Aerosol Optical depth (AOD) obtained by various satellite sources namely MODIS, OMI and reanalysis dataset MERRA-2 was validated against ground data over a time period. The validation holds its own prominence in a situation when there are numerous sources of data. It is highly essential to check the suitability of data for analysis in any type of research. Global distribution of spectral AOD, inversion products, and precipitable water in diverse aerosol regimes are provided by AERONET. A wide set of ground observations are available for Pune and Kanpur over a time period of 15 years (2004-2018). Limited observations of daily data are available for Goa, Trivandrum and Visakhapatnam for 2000, 2007 and 2008 respectively. Therefore, validation was carried out with Pune and Kanpur AERONET

datasets. The Fig 3.3 shows the methodology adopted for statistical validation and trend analysis.

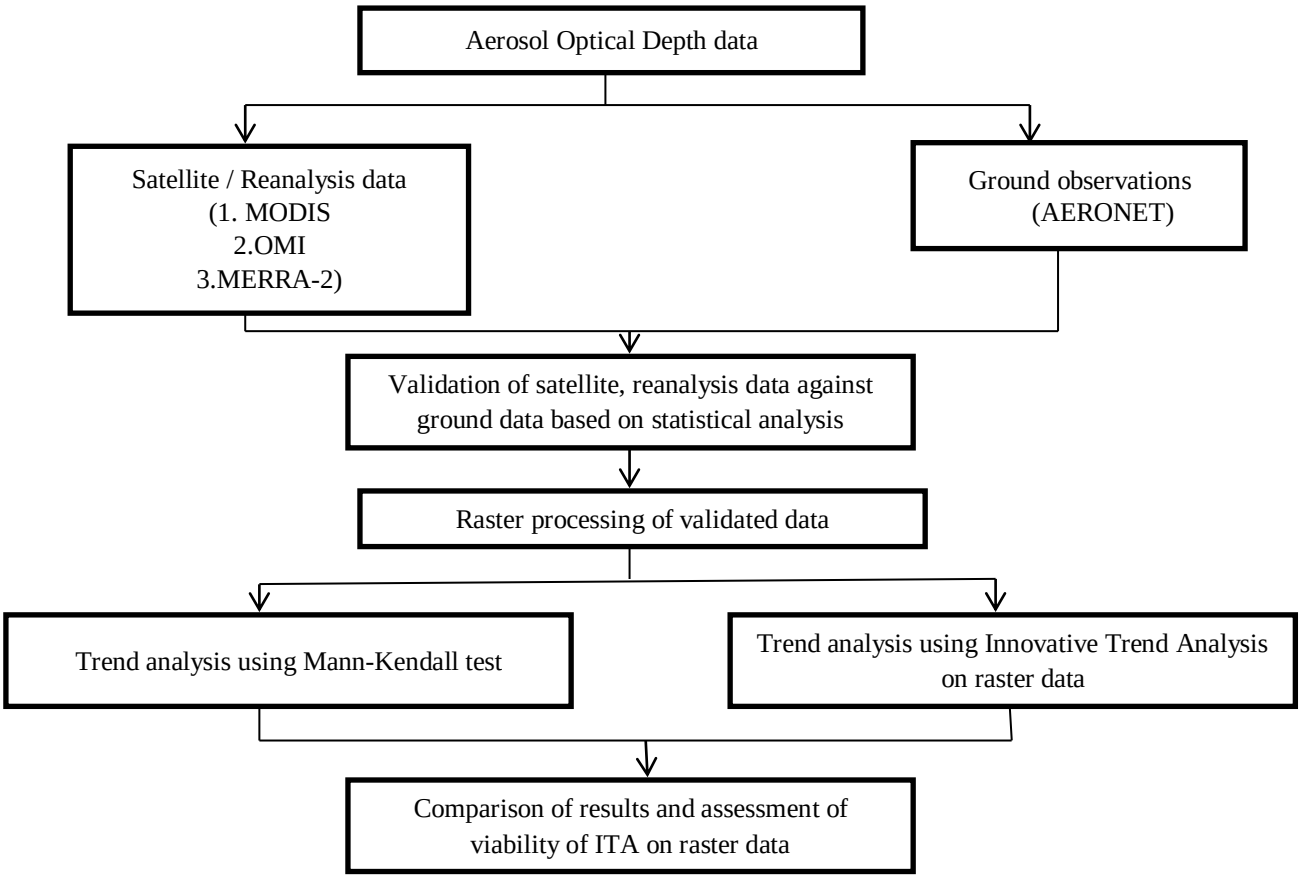

Fig 3.3: Flowchart for the methodology of validating satellite and re-analysis AOD data with ground observations

The satellite AOD observations are provided at 550nm wavelength. The ground observations for AOD are provided at 440nm and 675nm wavelengths. AOD at 550nm wavelength is to be calculated using angstrom exponent from Angstrom law (Angstrom 1929) in order to validate satellite AOD as shown in the following equation (3.3).

$$\tau_3 = e^{[\ln(\tau_1) - \ln\left(\frac{\lambda_3}{\lambda_1}\right) * \alpha]} \quad \text{- (3.3)}$$

Where τ_3 = AOD at 550nm, τ_1= AOD at 440nm, λ_3= 550nm, λ_1= 440nm, α = angstrom exponent. The angstrom exponent is an important parameter that describes the spectral behaviour of the atmospheric extinction and transmission due to aerosols. The uncertainty in AE determined from MODIS satellite observations is ±0.03+20% over land.

For the present study the R code developed was used to validate MODIS, OMI and MERRA-2 datasets with ground data using 'raster' and 'ggplot' packages. Initially, satellite derived AOD product was read in R software and data was extracted on excel sheet for the required

point location along with date. A buffer zone of 5 km was created around the point location and the averaged pixel value within the buffer was considered for evaluation. Next the ground observations which are stored in excel format are read into R software along with date. The two datasets are compared using the date column to exclude no data values and a scatter plot along with coefficient of determination and correlation coefficient was obtained using R software. The R scripts used in the analysis are given in Appendix-A.

The surface reflectance measures at 440nm and 670nm wavelength are given as inputs to lookup table continental algorithm to obtain AOD at 440nm and 670nm wavelengths. These two values are interpolated based on Angstrom law to obtain AOD at 550nm wavelength. MODIS data is available in GeoTiff format whereas OMI and MERRA-2 data are available in NetCDF format. The hourly observations are averaged to daily data while evaluating MERRA-2 data. There was a provision in the script to detect the outliers and remove them to improve coefficient of determination. The outliers are detected by using Mahalanobis distance concept (Ghorbani 2019). For the most parts of the Southern India, there are not many extreme events of biomass burning or dust storm (Sahu et al.,2015, Rastogi et al.,2016). Hence, in the present study the outliers detected may not represent the extreme events. In view of this Mahalanobis distance sounds to be suitable for outlier detection and removal for the current study. The Mahalanobis distance measures relative distance between two points with respect to the centroid. Mahalanobis distance is given by Eq (3.4).

$$D_i = \sqrt{(x_i - \mu)^T S^{-1} (x_i - \mu)} \quad \text{- (3.4)}$$

Where x_i = ith observation, μ = mean of observations, S = covariance matrix. In the present study an outlier loop was written down to detect outliers and to improve the coefficient of determination. The execution was such that the loop exits out when the coefficient of determination was more than or equal to 0.5. Also, the data was considered for further analysis only when the number of iterations for removing the outliers was less than or equal to 5. In addition to coefficient of determination, statistical errors like Root Mean Square Error (*RMSE*), Mean Absolute Error (*MAE*) and Bias were also calculated for all the three products considered in the present study. *RMSE* is the measure of error between observed and predicted data. Mean Absolute Error is the vertical distance between data and identity line. In general, it is a measure of difference between continuous variables. Bias is defined as the difference between estimated and true observation taken from a phenomenon The statistics are given in Eq (3.5) to Eq (3.7) (Vijaykumar et al.,2018).

$$RMSE = \sqrt{\frac{1}{n}\sum_{i=1}^{n}(y_i - \hat{y}_i)^2} \quad - \quad (3.5)$$

$$MAE = \frac{\sum_{i=1}^{n}|y_i - \hat{y}_i|}{n} \quad - \quad (3.6)$$

$$Bias = \frac{\sum_{i=1}^{n} y_i - \hat{y}_i}{n} \quad - \quad (3.7)$$

Where y_i = observed value from AERONET, $\hat{y}_i$ = predicted value from satellite/ model product n = Number of observations. The files are stacked month-wise for 2000-2019 and clipped to the required region. The pixel values are multiplied by 0.001 to obtain AOD in the range of 0-1. Basic statistics like mean and standard deviation for the stacked files are calculated and written to an excel file. The Trend in AOD is calculated using non-parametric Mann-Kendall test and Innovative Trend Analysis test using R statistical software.

3.6 Trend Analysis

In the present study, two methods are used to perform trend analysis on AOD data. The details are given in the following section.

3.6.1 Mann-Kendall Test

The non-parametric MK test is a widely used statistical method for analyzing trends in time series data. The test is used to determine if there is a monotonic trend in the data, without making any assumptions about the underlying distribution of the data. The test begins by determining the S statistic given by Eq (3.8), which is a measure of the total deviation between the data points. This value is then utilized to compute the p-value, which indicates the statistical significance of the observed trend. The p-value represents the probability that the observed trend could have occurred by chance. Additionally, Sen's method is used to calculate the magnitude of the change in the ADRF data, which provides information about the rate of change in the data over time. This information can be utilized to enhance the underlying patterns in the data and make informed decisions based on the results. The Mann-Kendall method does not assume any specific underlying distribution for the data, which makes it suitable for analyzing a wide range of time series data. This statistic is then used to determine whether there is a significant trend in the data (Mann 1945, Kendall 1975) represented as follows.

$$S = \sum_{a=1}^{n-1}\sum_{b=a+1}^{n} sgn(x_b - x_a) \quad -(3.8)$$

where x_b represents the observed value at time b, while x_a represents the observed value at time a. It is important to note that a should be less than b, and n represents the total amount

of data points in the set. The sign of the value is determined according to Eq (3.9), as proposed by Mann (1945) and Kendall (1975).

$$sgn(x_b - x_a) = \begin{cases} 1 & if\ (x_b - x_a) > 0 \\ 0 & if\ (x_b - x_a) = 0 \\ -1 & if (x_b - x_a) < 0 \end{cases} \quad \text{-(3.9)}$$

The numerous trials on the test disclosed that when the number of samples is greater than 8, the S statistic conforms to normal distribution which has mean as in Eq (3.10) and variance as in Eq (3.11) (Mann 1945, Kendall 1975).

$$E(S) = 0 \quad (3.10)$$

$$Var(S) = \frac{n(n-1)(2n+5) - \sum_{i=1}^{r} t_p(t_p-1)(2t_p+5)}{18} \quad (3.11)$$

Where i denotes the number of measurements, r denotes frequency of the occurrence of a specific value in the dataset and the value of t represents the number of data points with the same value in the pth group. The Z score is used to check the statistical significance of S. The Z statistic follows a normal distribution with zero mean and unit variance as shown in Eq (3.12) (Chakraborthy et al., 2011).

$$Z = \begin{cases} \frac{S-1}{\sqrt{var(S)}} & ; S > 0 \\ 0 & ; S = 0 \\ \frac{S+1}{\sqrt{var(S)}} & ; S < 0 \end{cases} \quad \text{-(3.12)}$$

The MK method is used to test whether there is a trend in a set of data. The hypothesis that there is no trend is denoted as null hypothesis H_0 whereas the hypothesis that there is presence of trend is considered as alternative hypothesis H_i. The null hypothesis is rejected based on the two-tailed test. The Z test statistic value is used to test H_0. If Z is negative, it elucidates a decreasing trend, and vice versa. In this study, the hypothesis is tested at a confidence level of 95%. The slope of the trend in dataset is calculated by linear regression method. The Sen's slope estimator, on the other hand, is a robust non parametric trend operator that is resistant to such errors. In this study, the magnitude of the trend in time series data is estimated using Eq(3.13).

$$Q_i = \frac{x_b - x_a}{(b-a)} \quad \text{-(3.13)}$$

The present study incorporates MK test to test the trend of Q_i, which is the slope between data points $x_b$and x_a. The test was performed using the 'spatialEco' and 'raster' packages in R software (Evans et al., 2019). We specifically focused on the trend during the 2015-2019 time period, and our results were considered with 5% significance level.

3.6.2 Innovative Trend Analysis Method

Innovative Trend Analysis (ITA) is a novel method to capture the trend in data irrespective of type of distribution of data. It is non-parametric in nature where the data is subdivided into two parts equally and plotted on a Cartesian coordinate scale. The approach is based on the fact that the plot of two identical time series against each other results in scatter of points along 45^o line. The data is said to have a positive trend if the scatter points are above the 45^o line and vice versa. R statistical software facilitates ITA using *trendchange* (Sandeep et al.,2019) package. The source code of ITA is designed such that trend indicator and magnitude of trend was calculated and returned as result (Sen, 2012). As ITA was applied to raster data, pixels having significant trend are obtained by p-value which was incorporated in the designed code. The trend indicator (D) is calculated using Eq (3.14) (Sen, 2012).

$$D = \frac{1}{n} \sum_{i=1}^{n} \frac{10(X_j - X_i)}{\mu} \qquad \text{-(3.14)}$$

Where X_j= data in the second half series, X_i= data in the first half series, n=length of data, $\boldsymbol{\mu}$ = mean of the first half series. The properties of the trend indicator are similar to Z statistic of Mann-Kendall test. In the present study significant positive and negative trends were studied from the Innovative Trend Analysis for raster data. The results are further compared to check the viability of ITA application to raster data.

3.7 AOD-Radiation-Temperature Interactions

The methodology adopted in this study is illustrated in Fig 3.4. The initial step is to calculate the ADRF at the Top of the Atmosphere ($ADRF_{TOA}$), at the Surface ($ADRF_{SUR}$), and in the atmosphere ($ADRF_{ATM}$) using MERRA-2 radiation flux data under all-sky conditions. The second step is to analyze the trend in ADRF over the period of 2015-2019 using the Mann-Kendall analysis method. The final step is to evaluate the effect of aerosols on temperature for each Koppen's climatic zone in the study area.

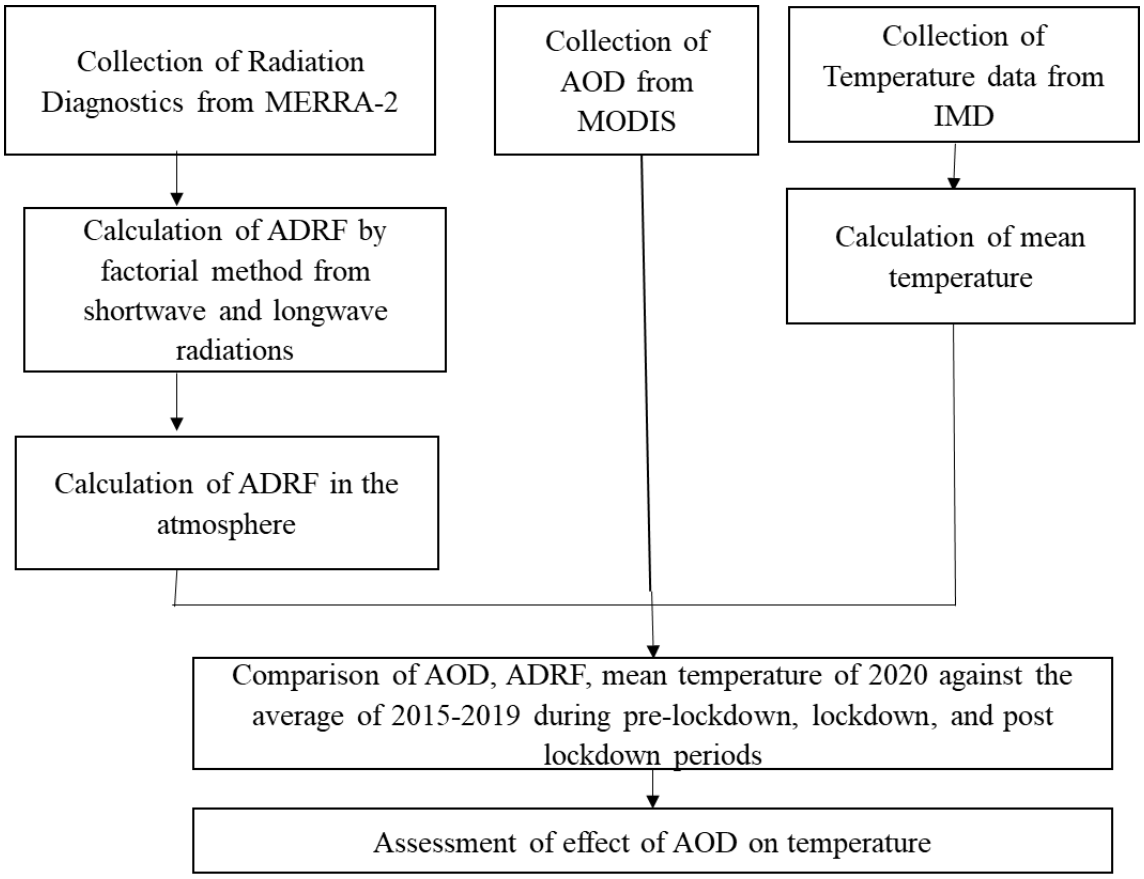

Fig 3.4: Methodology adapted for understanding AOD-Radiation-Temperature Interactions

3.7.1 Calculation of ADRF

The ADRF calculation requires several parameters, including the Surface Net Downward Shortwave Flux (SWGNT), the Surface Net Downward Shortwave Flux assuming no aerosol (SWGNTCLN), the Surface Net Downward Longwave Flux (LWGNT), the Surface Net Downward Longwave Flux assuming no aerosol (LWGNTCLN), the TOA Net Downward Shortwave Flux (SWTNT), the TOA Net Downward Shortwave Flux assuming no aerosol (SWTNTCLN), the Upwelling Longwave Flux at TOA (LWTUP), and the Upwelling Longwave Flux at TOA assuming no aerosol (LWTUPCLN). While six of these parameters can be directly obtained from MERRA-2, the LWGNTCLN and LWTUPCLN need to be calculated. The following equations are generally used to calculate the ADRF: Eq (3.15) (ADRF at surface) and Eq (3.16) (ADRF at TOA).:

$$ADRF_{SUR} = (SWGNT + LWGNT) - (SWGNTCLN + LWGNTCLN) \quad \text{-(3.15)}$$

$$ADRF_{TOA} = (SWTNT + LWTUP) - (SWTNTCLN + LWTUPCLN) \quad \text{-(3.16)}$$

The atmospheric ADRF ($ADRF_{ATM}$) was calculated by subtracting the ADRF at the surface from the ADRF at the top of the atmosphere (TOA). According to standard conventions, a positive $ADRF_{ATM}$ warms the atmosphere while a negative ADRFATM cools it. The current

study aims to determine the missing parameters using two methods: the factored method and the difference method. The factored method involves dividing SWGNTCLN by SWGNT to obtain a factor, which was then used to calculate LWGNTCLN using Eq(3.17). The difference method, on the other hand, uses the difference between SWGNTCLN and SWGNT to calculate LWGNTCLN using Eq(3.18).

$$LWGNTCLN = \frac{SWGNTCLN}{SWGNT} * LWGNT \quad \text{-(3.17)}$$

$$LWGNTCLN = SWGNTCLN - SWGNT + LWGNT \quad \text{-(3.18)}$$

As part of the analysis, five grid points in each climate zone were considered and plotted a time series of long wave flux data for 2019, calculated using both the factored and difference methods. The grid points chosen were Goa (Am), Nanded (Aw), Hyderabad (BSh), Raipur (Cwa), and Coimbatore (Cwb). The plot showed that the factored method produced more accurate results compared to the difference method. Therefore, we used the factored method to calculate the ADRF at the surface, TOA and within atmosphere for the gridded study area.

3.7.2 Effect of Aerosols on Temperature

To assess the effect of aerosols on the Earth's energy balance, Kumar et.al 2019, Mao et.al 2022 analysed the temperature changes caused by aerosols in each climate region of the study area. This helps in understanding the impact of aerosols on the Earth's radiation budget. The annual mean temperature and the annual average daily radiation flux (ADRF) for the year 2020 and the average of the years 2015-2019 are calculated for the study area. The comparison was then made between the year 2020, which was impacted by the COVID-19 pandemic, and the average of the years 2015-2019 over three time periods: the pre-lockdown period (from 1st January to 23rd March), the lockdown period (from 24th March to 31st May). and the post-lockdown period (from 1st June to 31st August).

3.8 AOD-Cloud-Precipitation Interactions

The methodology used to understand aerosol-cloud-precipitation interactions is shown in Fig 3.5. Cloud formation begins with the activation of Cloud Condensation Nuclei (CCN). Aerosols are important in the formation of CCN. MODIS provides the aerosol index, which is calculated as the product of the angstrom exponent and the AOD. Previous research on the effect of aerosols used the aerosol index as the primary parameter. Some researchers, however, have stated that the aerosol index was not reliable over land (Kourtidis et al., 2015, Liu et al., 2020). Because the majority of the current research area is land, AOD was used as the primary parameter to characterize aerosols and study their effect on cloud formation.

Cloud parameters are used to identify low warm clouds. Low warm clouds were defined as pixels with CTP greater than 680 hPa and CTT greater than 0°C according to Liu et.al (2020). MODIS products are available in a variety of spatial resolutions. Using R statistical software, all cloud parameters were resampled to a resolution of 10km×10km. The files were cropped to the required size for the study.

The atmospheric stability states are classified into four categories based on the values: isolated thunderstorms (20<K<25), widely scattered thunderstorms (20<K<25), scattered thunderstorms (30<K<35), and numerous thunderstorms (K>35). Rainfall was classified into three types based on its intensity: light, moderate, and heavy (Soni et al.,2020). The effect of aerosol on macrophysical properties of clouds was investigated using linear regression slopes of AOD-CF for different atmospheric stability states The R code is scripted to identify the parametrical data corresponding to pixels with light rain and to average the corresponding cloud parameters for 11 AOD bins. AOD bins range from 0 to 1 with a 0.1. The correlation plots and trendlines are then prepared

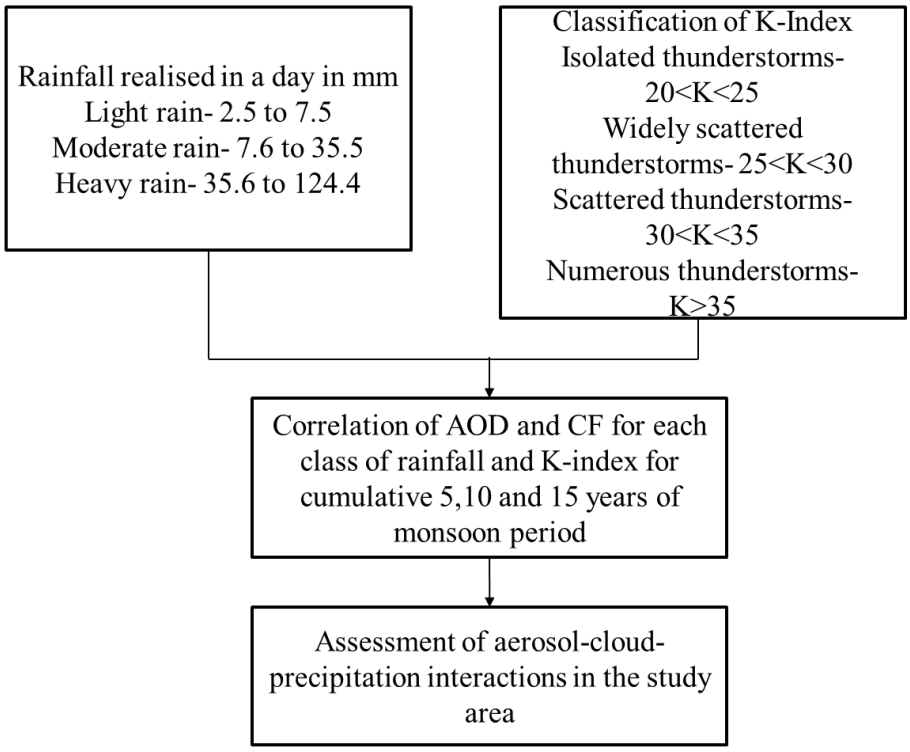

Fig 3.5: Flow chart showing the methodology adopted for AOD-Cloud-Precipitation Interactions

Also, the significance of correlation was evaluated using the p-value. If the p-value is less than 0.05, the correlation is said to be significant at 95% confidence level. The analysis is performed for three cumulative datasets namely cumulative datasets, namely 5,10 and 15 years of data. The cumulative five years indicate the dataset from 2015 to 2019, the ten years indicate the dataset from 2010 to 2019 and the fifteen years indicate dataset from 2005-2019. The cumulative periods for the analysis are considered with a goal of understanding the behaviour of AOD and CF for different atmospheric stability states as the number of samples increases.

The spatial distribution of AOD for the three cumulative datasets in light, moderate and heavy rain conditions was investigated by categorising the study area into three classes based on the pixel values i.e 0-0.5 (low polluted), 0.5-1 (moderately polluted) and greater than 1 (highly polluted). Similarly, the CF was classified into three groups based on pixel values: 0.7-0.8 (low), 0.8-0.9 (moderate) and 0.9-1 (high). In order to obtain a better picture of the distribution of AOD and CF, Koppen's world climate classification was considered for the study area. The effect of AOD on CF and precipitation under different atmospheric stability states was analysed.

3.9 Analysis of the Causes for Extreme Precipitation Events in and around Urban Cities

To understand the impact of aerosols on precipitation on a closer note, urban cities were selected for the study. The urban areas chosen for this analysis are Mumbai, Chennai and Bengaluru from Aw, Hyderabad from BSh (Fig 3.6). The abovesaid places are chosen based on the land use and land cover map imposed over the study area. Extreme Precipitation Events (EPEs) pose a serious risk to human life, agriculture, and infrastructure by causing flash floods and landslides (Sujatha and Sridhar, 2021). With enhanced atmospheric moisture transport brought on by a warming climate, EPEs are anticipated to occur more frequently (Hamada et al., 2015; Kumar et al., 2019).

The methodology used for the analysis of EPEs in metropolitan cities is depicted in Fig 3.6. EPEs are identified based on percentile calculations of precipitation data. The data was sorted in ascending order to compute percentiles, and the resulting distribution represents the frequency-intensity relationship of precipitation. The 95th percentile of precipitation was calculated using the R statistical software. This study utilizes daily GPM precipitation data from 2015 to 2021 for percentile calculations. Precipitation exceeding the 95th percentile

threshold was considered an extreme event. Extreme events are identified for the metropolitan cities of Peninsular India from 2018 to 2020.

For each identified extreme event in the metropolitan cities, the data corresponding to aerosol and cloud properties for a period of 10 days prior to the event are visualized using ArcMap 10.2. In the present study, we have analyzed 6 events from Mumbai, 5 events from Chennai, 5 events from Hyderabad, and 2 events from Bengaluru, and the results are presented.

3.9.1 Percentile Calculation

The percentile helps to compare a score with other scores in the dataset, aiding in the identification of a threshold value. Data above this threshold value was considered an extreme event of precipitation. The steps involved in percentile calculation are as follows: Initially, the daily precipitation data from 2015-2021 are sorted in ascending order. The second step involves multiplying the required percentile, which is the 95th percentile for this study, with the total number of values and rounding it to the nearest integer.

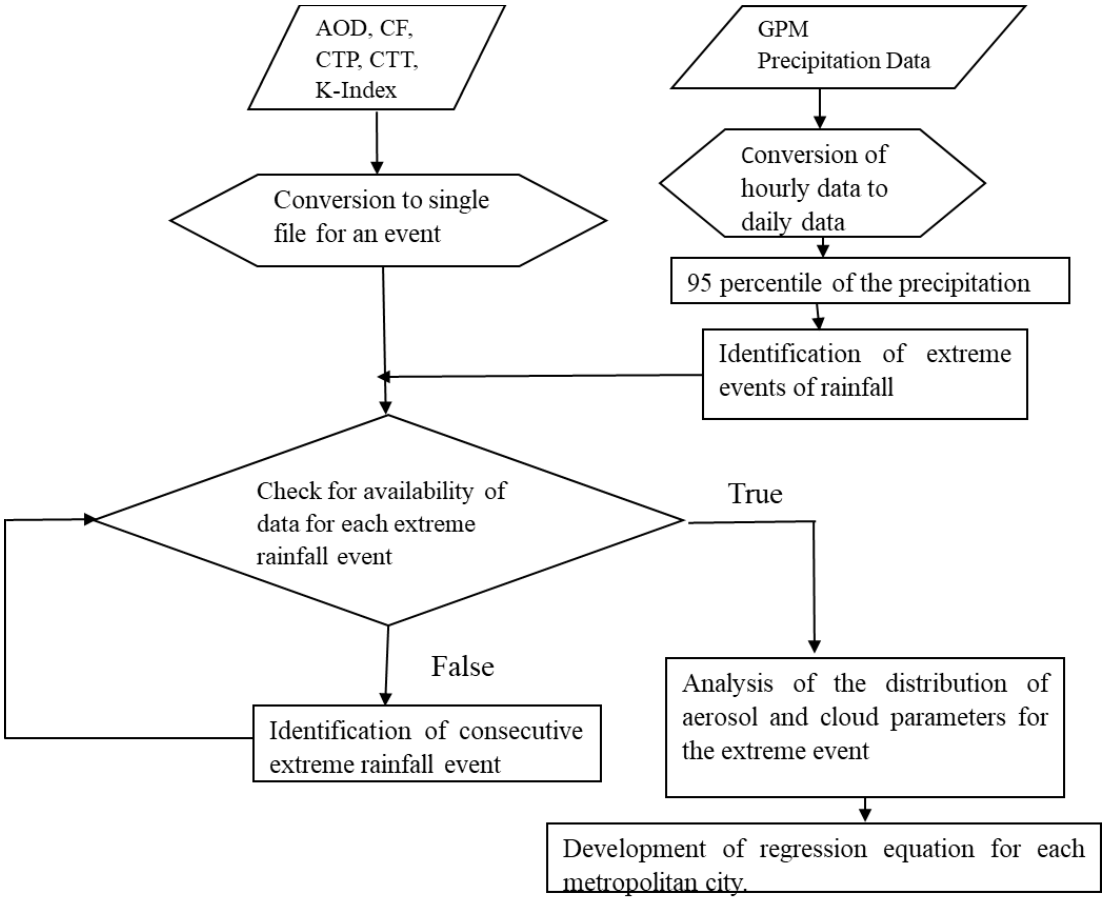

Fig 3.6: An Overview of the Research Approach for understanding the causes influencing the occurrence of EPE in metropolitan cities

This gives us the threshold value. In the third step, we count the values from left to right in the dataset until we reach the number obtained in the previous step. The corresponding value is the 95th percentile of the dataset. Percentile calculation was performed over raster images corresponding to the metropolitan cities. This means that each pixel covering the metropolitan city has a different 95th percentile value.

3.9.2 Identification of Events

The series of raster data corresponding to precipitation was aggregated to match the resolution of the AOD data. The 95th percentile values are also aggregated to the same resolution. Each cell in the daily precipitation raster was then compared to the corresponding cell in the 95th percentile of precipitation using R statistical software. If the precipitation value is greater than the 95th percentile value, the data was retained; otherwise, the pixel value is classified as 'NA' (not available). The raster was saved to a folder if more than half of the pixels covering the area contain valid data.

3.9.3 Analysis of Parameters

For each identified extreme event in the metropolitan cities, the aerosol data for the 10 days leading up to the event was visualized. If aerosol data was available, other parameters, namely CF, CTP, CTT, and K, are averaged for the 10 days prior to the extreme event. The analysis includes examining the distribution of cloud properties and atmospheric stability during the extreme event. Additionally, the number of pixels experiencing moderate and heavy precipitation in the area was observed. The behavior of cloud properties and atmospheric stability in these pixels was analyzed, and the combination of parameters influencing precipitation occurrence was observed for each metropolitan city.

3.9.4 Multiple Regression Analysis

The statistical analysis was conducted using Multiple Regression Analysis (MRA), which is a type of analysis that examines the linear relationship between a dependent variable and two or more independent variables (Zain et al., 2008). In this study, MRA is employed with precipitation as the dependent variable and AOD, CF, CTP, CTT, and K as the independent variables. The regression was performed by extracting pixel values of each variable corresponding to Extreme Precipitation Events (EPEs) for each metropolitan city. The general form of MRA is represented by Eq. (3.18):

$$y = \propto + \beta_1 x_1 + \beta_2 x_2 + \cdots + \beta_n x_n \qquad (3.18)$$

Where y is dependent variable, $\propto$ is intercept, $x_1, x_2, x_3 \ldots . x_n$ are independent variables, $\beta_1, \beta_2, \beta_3 \ldots . \beta_n$ are coefficients

3.10 Closure

In this chapter, the selected study area and datasets required for the research work are discussed in the first three sections. The fourth section of the chapter deals with overall methodology of the research work. The fifth section deals with validation of satellite AOD data and model re-analysis data against the ground truth data. The trend in AOD with the conventional Mann-Kendall test and Innovative Trend Analysis (ITA) method are dealt in sixth section of the chapter, The innovativeness lies in implementation of ITA for the raster data. The methodology for AOD-radiation-temperature interactions is dealt in the seventh section of this chapter. The long wave radiation under all-sky and no aerosol condition are calculated based on the factored method which is explained in the sixth section of this chapter. The ADRF under all-sky conditions is calculated based on the methodology and the variables of 2020 are compared against the average of 2015-2019 for time periods prior to lockdown, during the lockdown and post lockdown. The eighth section of the chapter presents with the methodology to relate AOD, cloud fraction and precipitation based on K-index meteorology. The methodology for better understanding of the impact of AOD in causing EPEs in and around metropolitan cities is presented in ninth section of this chapter. The analysis is performed based on the methodology and the results corresponding to the framed objectives are presented in Chapter 4-6.

CHAPTER 4

VALIDATION OF SATELLITE AND RE-ANALYSIS AOD PRODUCTS WITH GROUND OBSERVATIONS

4.1 General

Based on the methodology proposed in the previous chapter, following are the results corresponding to validation analysis. The validation holds its own prominence in a situation when there are numerous sources of data. It is highly essential to check the suitability of data for analysis in any type of research. The present chapter deals with the validation of satellite and re-analysis observations with ground data and trend analysis using MK-test and ITA method.

4.2 Datasets for Validation

A wide set of ground observations were available for Pune and a minor set of observations are available for Trivendram, Visakhapatnam and Goa in the considered study area. The validation of satellite and re-analysis AOD product with ground observations obtained from AERONET helps us to select a suitable data required for the analysis. The ground data used for validation is corresponding to Pune and Kanpur for a period of 15 years from 2004-2018The validation was performed using the R Statistical software. The code facilitated the extraction of satellite and re-analysis product at the sun photometer location with a buffer of 5km. The data was averaged for a day and written to the excel sheet and compared with the ground observations. The excel was then read in R and the columns are compared based on Date to exclude the days with no data. Finally, a scatter plot was prepared by comparing the satellite and re-analysis data with ground observations. The Coefficient of Determination is also shown in the plot. If the $R^2$was less than 0.5, the outlier detection loop of the code was

activated and the outliers in the data are removed by Mahalnobis distance method. The data was filtered until the R^2 is greater than 0.5. The scatterplots are shown in Fig 4.1. The loop was initiated thrice for the improvement in co-efficient of determination corresponding to Pune. Almost, 120 observations were treated to be outliers. The R^2 for Kanpur is 0.7 and it is obtained without initiating the outlier loop. It implies that the outliers were less in Kanpur data. Similarly, the R^2 is 0.25 and 0.58 with MERRA-2 data for Pune and Kanpur respectively. With the execution of loop for improvement of R^2 for Pune, it was found to be very negligible after 5 iterations, but for Kanpur the outlier loop is not initiated. The coefficient of determination is found to be at lower end with OMI data for both locations of the order of 0.33 and 0.39 even after execution of outlier loop.

4.2.1 Statistics of Validation

The other statistical measures evaluated to validate satellite AOD with ground AOD are Root Mean Square error (RMSE), Mean Absolute Error (MAE) and bias. The errors and number of samples that are coincident with satellite data and ground data are shown in Table 4.1. The RMSE, MAE and bias for validating MODIS with AERONET was found to be minimum for both Pune and Kanpur whereas all the errors were found to be at higher end while validating OMI data. From the table it is evident that MERRA-2 is statistically more reliable than OMI but less reliable than MODIS. Thus, it can be concluded that MOD04_L2 (Optical depth Land and Ocean) is a suitable product for further analysis over the study area.

Table 4.1: Statistical errors for evaluation of MODIS, OMI, MERRA-2 with AERONET

	MODIS		**OMI**		**MERRA-2**	
Parameter	**Pune**	**Kanpur**	**Pune**	**Kanpur**	**Pune**	**Kanpur**
No. of samples (NS)	1692	1625	902	2462	1415	3336
Coefficient of determination (R^2)	0.51	0.7	0.33	0.39	0.25	0.58
RMSE	0.17	0.22	0.46	0.31	0.2	0.21
MAE	0.12	0.14	0.42	0.25	0.15	0.14
Bias	0.02	-0.08	0.42	0.23	0.1	0.08

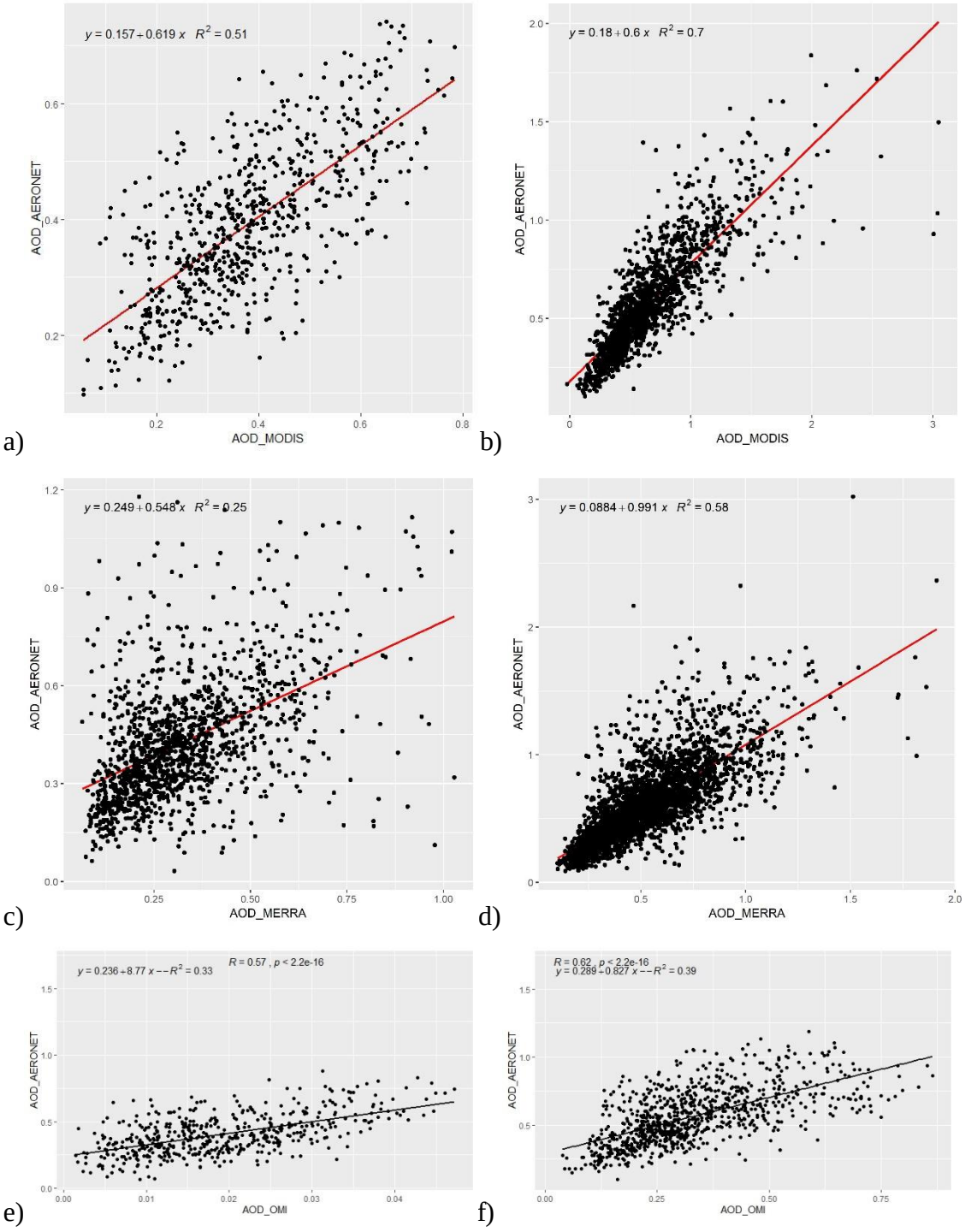

Fig 4.1: Correlation plots of a) MODIS with AERONET for Pune b) MODIS with AERONET for Kanpur c) MERRA-2 with AERONET for Pune d) MERRA-2 with AERONET for Kanpur e) OMI with AERONET for Pune f) OMI with AERONET for Kanpur

4.3 Spatial Distribution of AOD

The averaged observations of AOD during time period of 2000-2019 are disaggregated to 0.1º resolution. The spatial plot was classified into 9 classes based on the distribution to observe the distribution of AOD over study area. AOD observations greater than 1 are limited because of the cloud contamination (Chung et al., 2015). Nearly 50% of study area was found to have AOD between 0.24-0.42. AOD in between 0.18-0.24 which was considered as Zone 3 is found to hold second place in the distribution. The southern part of study area was dominated by lower AOD of the range of 0-0.18. Higher AOD was found to be dominant towards the coastal boundaries near Maharashtra and Orissa. The spatial distribution is shown in Fig 4.2.

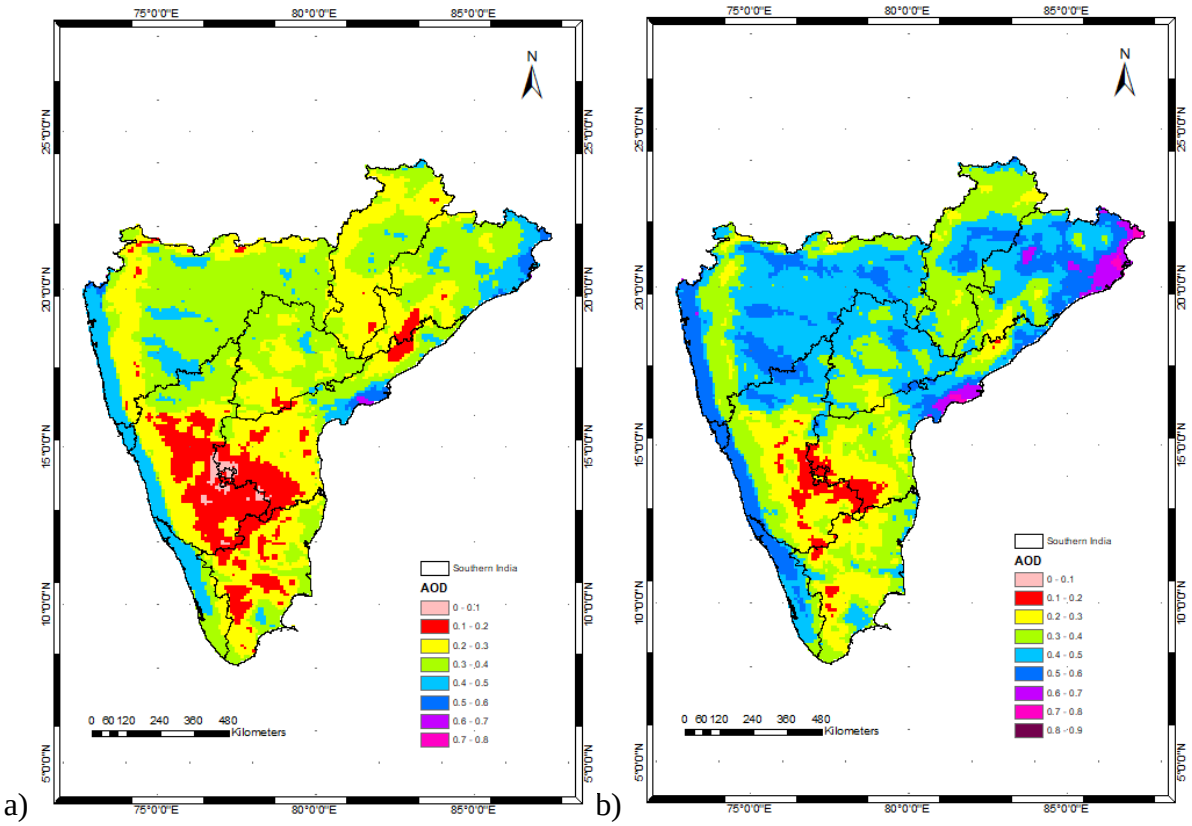

Fig 4.2: Spatial distribution of AOD over Southern India a) 2000-2009 b) 2010-2019

4.4 Decadal Trends in Aerosol Optical Depth

The trend in AOD was studied to know the changes over a period of 2000-2019. As aerosols are the anthropogenic emissions, their concentration is directly related to rate of industrialization (Chung et al.,2015). On a general note, the emissions have reduced due to implementation of remedial measures from IPCC during the period 2010-2019. In the present study, trend in AOD using MK-test and ITA was carried out.

4.4.1 Trend in MODIS AOD using Mann-Kendall Test

The satellite observations from MODIS AOD were divided into two parts by decade. The first decade referred to observations from 2000-2009 and second decade referred to observations from 2010-2019. Annual averaged raster observations were obtained using R statistical software. The code was written down such that each pixel has a value that is equal to average of observations obtained in a particular year at that pixel. Firstly, stack of observations was performed and stacked data was used to calculate trend from Mann-Kendall test.

The magnitude of trend as given by Sen's slope was calculated at pixels with trend at 95% significance level. In the first decade, it was observed that there was no decrease in magnitude. Nearly 66.46% of study area shown increasing trend as in Fig 4.3. The magnitude was divided into six classes namely no change, very low positive change, low positive change, moderate change, high positive change, very high positive change. Several research studies have been carried out to investigate the AOD trend over different Indian regions using satellite data and ground-based observations (Banerjee et al.,2014, Ramachandran et al.,2008, Babu et al., 2013).

The area of change in AOD is shown in Table 4.2. Majority of study area of the order of 374 lakh ha has shown a moderate increase in AOD. Nearly 296 lakh ha of study area has shown a low positive change in AOD. In the second decade, 40.26% of study area has shown no trend. The magnitude for second decade was divided into eight classes namely very low negative change, low negative change, no change, very low positive change, low positive change, moderate change, high positive change, very high positive change. But significant negative change of the order of 0.19 lakh ha was observed in the second decade.

Comparatively, 253.56lakh ha of study area was found to have moderate positive change in the second decade. The area for each classified was found to decrease in second decade with respect to first decade. Overall, it can be depicted that there was decrease in trend of AOD. between first decade and second decade in the study area. From Fig 4.2 and Fig 4.3a, magnitude of trend was found to be higher in regions of higher AOD. On the contrary magnitude of trend was maximum towards Orissa and Chattisgarh.

Table 4.2: Area of significant change obtained in both the tests (Lakh ha)

Test	Mann-Kendall Test		ITA	
Change	**First Decade**	**Second Decade**	**First Decade**	**Second Decade**
Very low negative change	-	0.0965	-	0.0965
Low negative change	-	0.0965	-	0.0965
Very low positive change	10.625	3.863	23.667	4.926
Low positive change	296.65	110.507	215.605	96.790
Moderate positive change	374.895	253.560	199.763	183.921
High positive change	119.970	112.430	60.566	73.703
Very high positive change	18.933	16.800	17.773	14.103

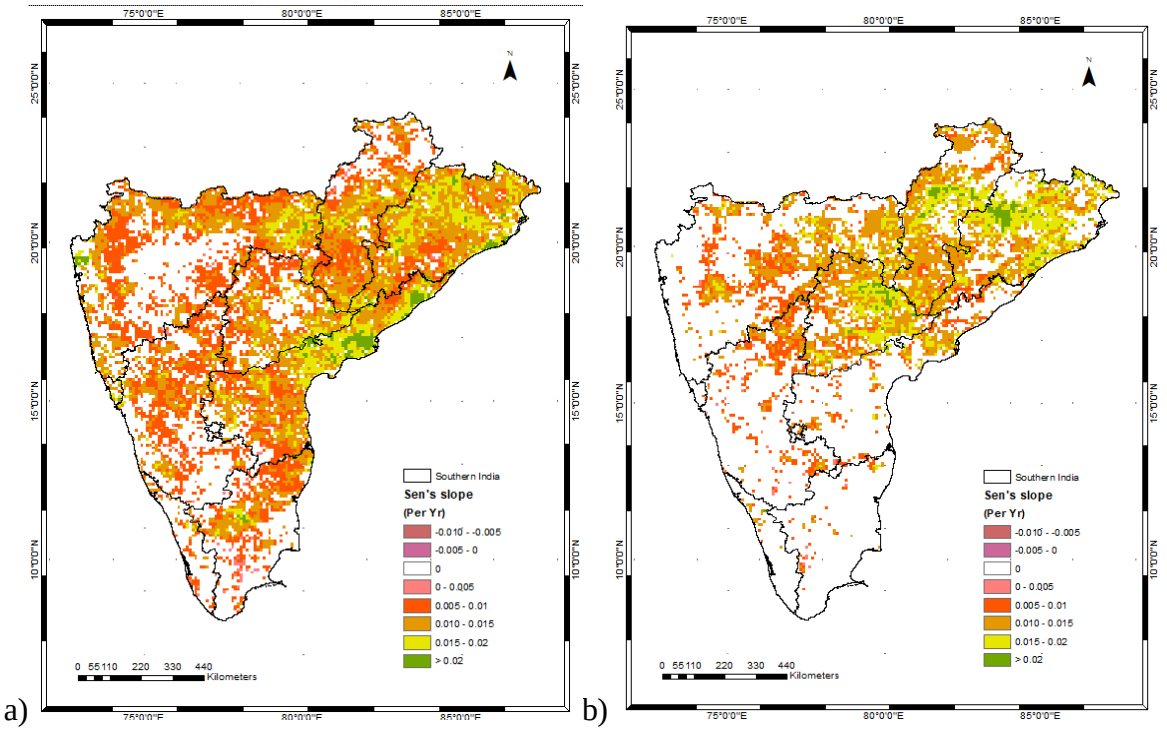

a) b)

Fig 4.3: Spatial Pattern of trend in AOD at 95% significance level for a) 2000-2009 b) 2010-2019 using Mann-Kendall Test.

4.4.2 Trend in MODIS AOD using Innovative Trend Analysis Method

As it was already discussed in the previous section that trend was observed on the basis of decade, the same dataset with annual averaged observations was considered for trend using Innovative Trend Analysis method (ITA). The methodology as described by Sen (2012) is to divide the dataset into two equal halves and thus calculate significant trend by plotting values on 1:1 scatter plot. In the present study, a novelty has been brought by calculating ITA on raster data using R statistical software which was previously confined to point/grid data. The first five years of a decade are considered as first half of data series and consecutive five years of data was considered as second half of series. The data of each pixel consists of 10 values in a decade which was sorted out corresponding to each series. The trend and magnitude of it was calculated for each pixel according to ITA methodology and written to an excel file. According to methodology explained by Sen (2012) trend indicator was similar to Z statistic of Mann-Kendall test and slope was same as Sen's slope. The slope was categorized into eight classes as discussed in previous section. It was observed that 41.84% of total study area was showing a positive trend which was less when compared to Mann-Kendall test as in Fig 4.4. Most of the study area of the order of 517 lakh ha and 373 lakh ha showed a positive change in AOD in first and second decades respectively.

The same process was applied for second decade which showed that 30% of the study area was found to have significant trend. On the contrary the significant negative change was observed in second decade which conforms to Mann-Kendall test. Nearly 41.84% of study area showed a significant positive change, out of which 215 lakh ha showed a low positive change which was mildly less when compared to first decade. The areas corresponding to each change using two different processes was shown in Table 4.2. Overall, it can be illustrated that trend in AOD has been reduced in the second decade when compared to first decade in both the methods. The decreasing trend might be due to decrease in the emissions by adaptation strategies of IPCC (Metz et al., 2001; Edenhofer et al., 2015). From Fig 4.2 and Fig 4.4a, it was evident that trend was maximum in regions of higher AOD.

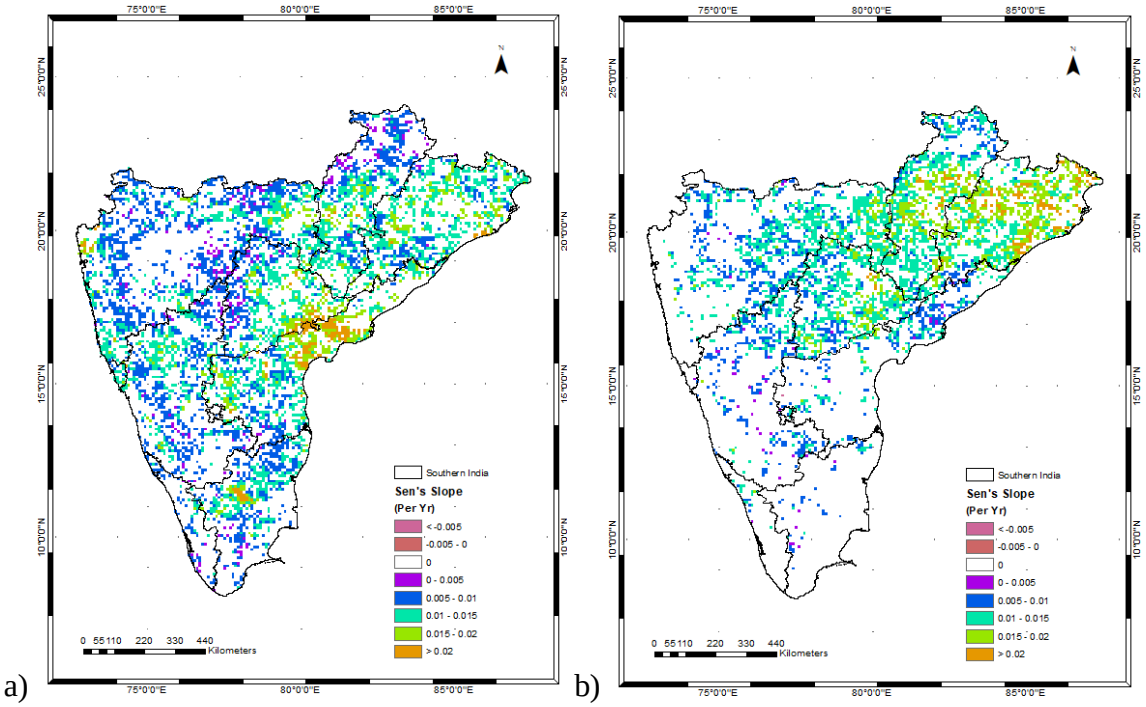

Fig 4.4: Spatial Pattern of trend in AOD at 95% significance level for a) 2000-2009 b) 2010-2019 using ITA

Increased aerosol concentration may have several important implications on regional climate, human health and hydrological cycle over the Indian subcontinent (Ramanathan et al.,2005 Lau et al., 2006). The economy of Southern India is mostly dependent on agricultural production which is in turn dependent on monsoon rainfall. Aerosol abundance strongly affects Indian summer monsoon rainfall through solar dimming mechanism and elevated heat pump mechanism (Ramanathan et al., 2005, Lau et al., 2010). The raise in concentration of aerosol may thus lead to climate imbalance and also affect the health of people in Southern India.

4.5 Closure

The validation of satellite and model re-analysis AOD data against ground observations showed that MODIS provides the suitable AOD data for the study area. The trend analysis using MK-test and ITA reveal that the trend was under estimated by ITA. The impact of AOD on temperature is dealt in fifth chapter.

CHAPTER 5
IMPACT OF AOD ON RADIATION DIAGNOSTICS AND TEMPERATURE

5.1 General

The COVID-19 lockdown has led to a pristine situation as the emissions were minimum during that period. It has helped us to compare the spatial distribution of ADRF and temperature against the average of 2015-2019. The effect of AOD on temperature is dealt in the following sections.

5.2 Calculation of Aerosol Direct Radiative Forcing

The ADRF time series plot for all five grid points is depicted in Fig 5.1. The flux was higher in most of the monsoon and post-monsoon seasons for all the five chosen grid points in the study area. The overall flux in the year 2019 ranged from -200 W/m^2 to 100 W/m^2. It can be seen that the LWGNTCLN calculated using the factored method follows a similar pattern to that of the LWGNT. The location of peaks and dips in LWGNTCLN exactly matches that of LWGNT in all the grid points. However, while the peaks and dips of the LWGNTCLN calculated using the difference method align with those of the LWGNT, the disparity in the amount of flux appears to be significant. The data for the grid points from the five different climate zones show a resemblance in their time series plots. The LWGNT for Goa (Fig. 5.1a) was in the range of -180 to -9.5 W/m^2. The LWGNTCLN by factored and difference method for Goa was in the range of -135 to -21 W/m^2 and -188 to 115 W/m^2, respectively. The minimum value of LWGNTCLN_d was close to LWGNT, whereas the maximum value was higher than that of LWGNT.

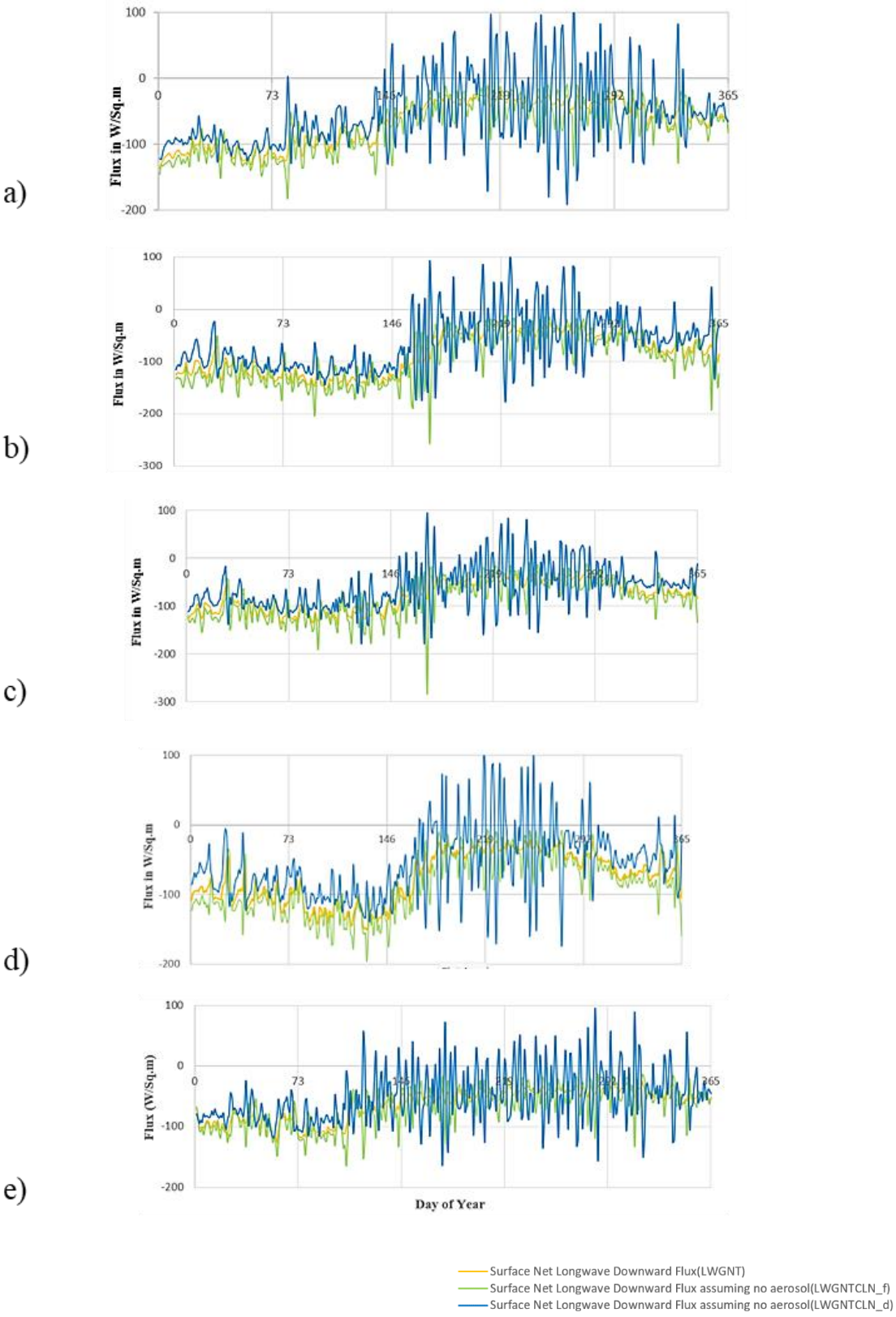

Fig 5.1: Time series plot of LWGNT, LWGNTCLN_f, LWGNTCLN_d for a) Goa b) Nanded c) Hyderabad d) Raipur e) Coimbatore for the year 2019

The LWGNT, LWGNTCLN_f, and LWGNTCLN_d for Nanded (Fig. 5.1b) are between -153 to -25, -254 to -10, and -175 to 101 W/m^2, respectively. From Fig. 5.1b, it was evident that the occurrence of the dip matches for LWGNTCLN_f, but the values at those particular locations are lower than that of LWGNT. On the other hand, the values at peaks are near to that of LWGNT. The LWGNT, LWGNTCLN_f, and LWGNTCLN_d for Hyderabad (Fig. 5.1c) are between -138 to -24, -282 to -9, and -178 to 94 W/m^2, respectively. Although the pattern of LWGNTCLN_d matches that of the LWGNT, the flux values appear to be higher, and the distribution is vague when compared to that of the LWGNT.

The values at dips are on a higher note for LWGNTCLN_f, but they are on par at peaks with respect to the LWGNT. The LWGNT, LWGNTCLN_f, and LWGNTCLN_d for Raipur (Fig. 5.1d) are between -150 to -20, -196 to -7, and -173 to 102 W/m^2, respectively. The pattern and distribution are the same as those of the other three locations. The LWGNT, LWGNTCLN_f, and LWGNTCLN_d for Coimbatore (Fig. 5.1e) are between -127 to -25, -165 to -14, and -164 to 95 W/m^2, respectively. The values at dip locations are lower for LWGNTCLN_f and LWGNTCLN_d, but the values of LWGNTCLN_f at peak locations are on par with LWGNT and that of LWGNTCLN_d are higher. On the whole, it can be said that LWGNTCLN obtained by the factored method appears to be in consonance with LWGNT.

5.2.1 Trend in ADRF

Over the period of 2015-2019, the trend in ADRF in the atmosphere was calculated using the non-parametric Mann-Kendall test as described in section 3.5.1. The magnitude of the trend at a 5% significance level was then determined using the Sen's slope formula, which divides the magnitude into four classes: very low positive change, low positive change, moderate change, and high change. Most of the study area exhibited a low positive change in ADRF. The areas experiencing very low positive change and high change were roughly equal in the monsoon climate. This might be due to the emissions from water bodies in different seasons of a year. The tropical savanna climate region showed a very low positive change, followed by moderate and high changes. The area with high change was more in Aw. This might be due to the industrial emissions in that time period. The humid subtropical climate exhibited low and moderate positive changes significantly. The subtropical oceanic highland climate region showed only a very low positive change in the trend. The areas corresponding to these four classes were calculated for all five climate zones and presented in a Table 5.1. The trend in ADRF was depicted in Fig 5.2.

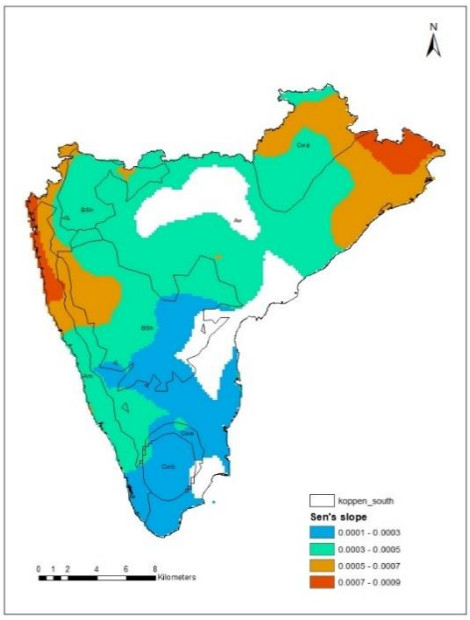

Fig 5.2: Spatial distribution of trend in ADRF

Table 5.1: Area of significant change in each climate zone (in lakh hectares)

Magnitude / Climate Zone	Very low positive change	Low positive change	Moderate change	High change
Am	13.42	41.30	19.07	13.90
Aw	104.28	328.26	97.67	33.73
BSh	64.50	166.00	38.72	-
Cwa	9.78	74.66	49.16	0.67
Cwb	39.78	2.20		

5.3 Yearly variations in the AOD, ADRF and temperature for the three different timescales

The variations in the AOD, ADRF and temperature for the period of 2015-2020 over the timescale of pre-lockdown (Jan 1 to Mar 23), lockdown (Mar 24 to May 31) and post-lockdown (Jun 1 to Aug 31) are shown in Fig 4.16. The error bar in the figure represents standard error in the parameter considered during timescale of each year. The AOD from Jan 1 to Mar 23, Mar 24 to May 31, Jun 1 to Aug 31 of 2018 was 0.425, 0.449 and 0.526 respectively. The AOD in all the three timescales was found to be maximum in the year 2018 (0.425,0.449 and 0.526) (Fig 5.3a). The average AOD in the period (2015-2019) prior to lockdown timescale was ~0.7 while it was ~0.6 in the year 2020. The AOD in the lockdown

timescale of the year 2020 has also seen a decrease by ~0.1 compared to the average of the past five years (2015-2019). On the contrary, a significant increase of about ~0.8 was seen in the post-lockdown of the year 2020 when compared to the mean of the period 2015-2019. Similar observations were recorded by Pandey et al.,2020.

Fig 5.3: Variation of Parameters over the time period 2015-2020 in three timescales a) AOD b) ADRF c) Temperature (Error bar represents standard error in the parameter considered during timescale of each year)

The Fig 5.3b corresponds to the variation of ADRF over the period 2015-2020. The ADRF in the months of January to March of the years 2016,2017 and 2020 was almost the same and have the low values. The period March-May of 2017 (which is lockdown period in 2020) has seen a lower ADRF of -2.49 W/m^2 while the higher was in the year 2020 with a value of -1.09W/m^2. This may be because of higher amount of radiation reaching the Earth's surface which results in higher radiative forcing in the atmosphere. The post-lockdown timescale of the year 2020 has witnessed a higher ADRF of 2.34 W/m^2 which was close to that of seen in the year 2018 (2.39W/m^2). This may be due to relaxation of COVID restrictions across the country. Overall, it was observed that ADRF has shown an increasing trend in lockdown and post-lockdown period of 2015-2020 while it has shown the decreasing trend in the pre-lockdown period.

The Fig 5.3c shows the variation of temperature over the period 2015-2020. The temperature (25.96^{o}C) in the period of January 1 to March 23 of 2016 (which is pre-lockdown of 2020) was found to be maximum. In the year 2019 the temperature in the periods March 24 to May 31 (Lockdown period in the year 2020) and June 1 to August 31 (post-lockdown period in the year 2020) was 31.85^{o}C and 28.49^{o}C respectively. Those were the maximum values over a period of 2015-2020. The temperature was minimum in all the three timescales of 2020 when compared to the past five-year data. This may be due to the moderation in the COVID-19 restrictions across the country. This is in agreement with the annual report of 2020 provided by the Indian Meteorological Department (https://mausam.imd.gov.in).

5.4 COVID-19 Lockdown: Pristine situation

The COVID-19 pandemic that began at the end of 2019 has led to a complete shutdown of industrial and human activities in India from March 24, 2020 to May 31, 2020. During this time, there was a notable decrease in the accumulation of aerosols in the atmosphere worldwide (Muhammed et al., 2020; Chauhan and Singh, 2020). This decrease was also seen in satellite data from MODIS. To understand the impact of aerosols on temperature in a normal situation, the average of all variables from 2015-2019 was also analysed.

5.5 Spatial Distribution of AOD in the Atmosphere

The spatial distribution of aerosol optical depth (AOD) in the study area is shown in Fig 5.4. According to research conducted by Abin et al. (2021), the aerosol loading has decreased during the lockdown period in the study area. In fact, about 56% of the study area saw a decrease in AOD during the pre-lockdown period of 2020 compared to the average from 2015-2019. This decrease in AOD ranged from 0 to 0.43, while the increase fluctuated

between 0 to 0.48 which was in accordance with the results exhibited by Rani et al.,2022. The majority of the decrease was observed in the tropical monsoon region covering Goa and the humid subtropical region covering cities like Chennai and Bengaluru. On the other hand, the increase was predominantly seen in and around cities such as Pune, Mumbai, and Hyderabad. Approximately 84% of the study area experienced a decrease in AOD, which ranged from 0 to 0.56 which is in accordance with the observations made by Srivastava et al.,2021.

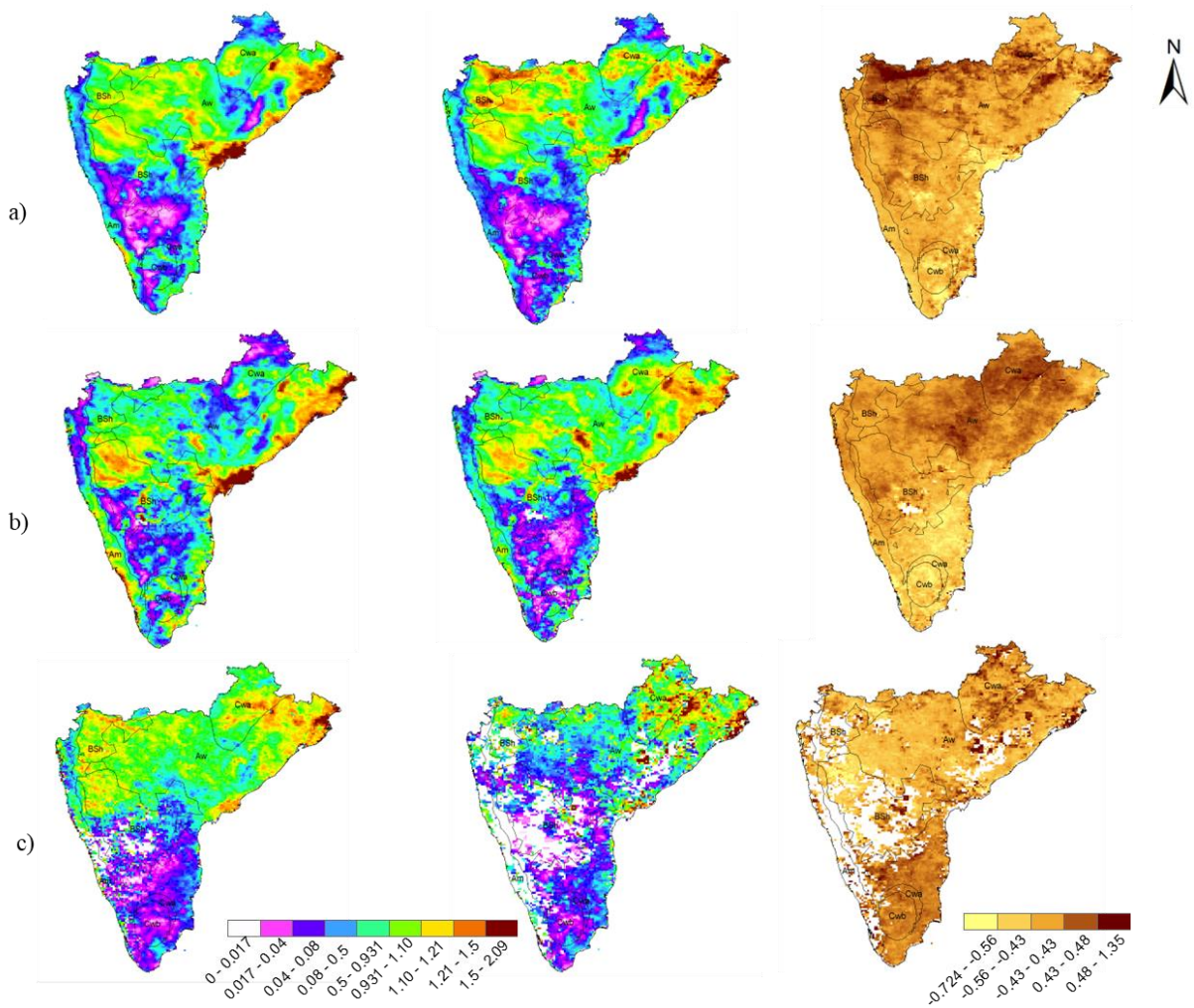

Fig 5.4: Spatial distribution of AOD for a) Pre-lockdown b) Lockdown c) Post-lockdown time periods (Left: Average of 2015-2019, Middle: 2020, Right: Change)

During the lockdown timescale, the spatial distribution of AOD shows that 15% of the area saw an increase in AOD ranging from 0 to 0.43, primarily in the states of Orissa and Chattisgarh which was in accordance with the results given by Gaouda et al.,2022. The decrease in AOD was distributed in the tropical savanna and warm semi-arid climate regions, which includes metropolitan cities like Hyderabad, Mumbai, and Bengaluru. In the post-lockdown timescale, there was a decrease in AOD that stretched from 0 to 0.72, while the increase ranged from 0 to 1.35. The distribution indicates that the decrease was observed in parts of the tropical savanna region with metropolitan cities like Bengaluru and Mumbai, while the increase was seen in parts of the humid subtropical climate region with places such as Raipur and Idukki.

5.6 Spatial Distribution of ADRF in the Atmosphere

The reduction in aerosol loading has resulted in a downfall in ADRF in the atmosphere (Abin et al., 2021, Subba et al.,2020). The ADRF in the atmosphere for the year 2015 was -1.5±0.006 W/m^2, and in 2019, it was -1.42±0.005 W/ m^2. Over a period of five years, there has been an atmospheric warming of 0.08±0.001 W/ m^2, which was in accordance with Rutan et al., 2015. The ADRF prior to the lockdown timescale in the year 2015 was -3.64±0.007 W/ m^2, and in 2019, it was -4.10±0.008 W/ m^2. However, the average ADRF (2015-2019) for pre-lockdown lies closer to that of 2019 with a value of -4.06±0.009 W/ m^2. The ADRF was lower in most of the Aw region and high in the BSh region (Fig 5.5). The ADRF in the atmosphere during the lockdown timescale for the year 2015 was -1.74±0.009 W/ m^2, and in 2019, it was -2.09±0.006 W/ m^2. The ADRF was low in the northern parts of BSh and high in the southern parts of the BSh region in the study area.

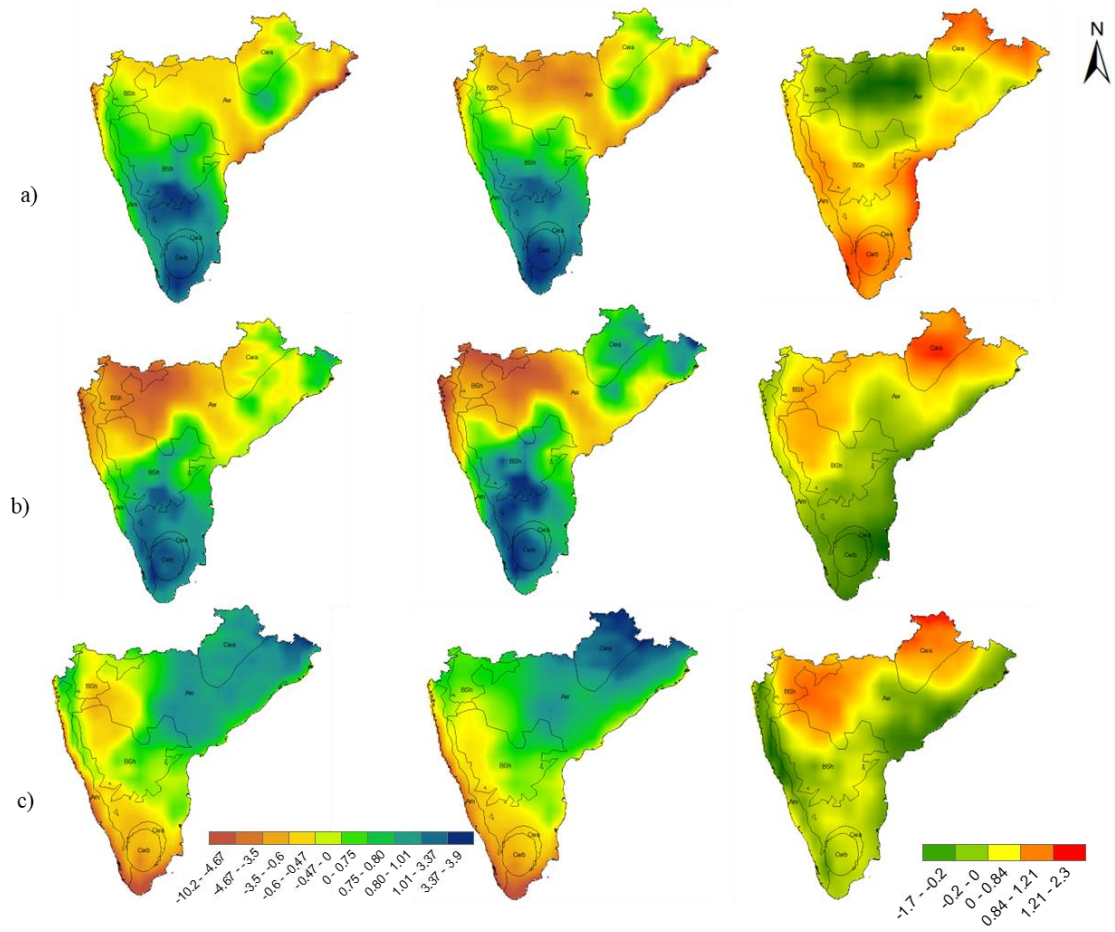

Fig 5.5: Spatial distribution of ADRF in the atmosphere for a) Pre-lockdown b) Lockdown c) Post-lockdown time periods (Left: Average of 2015-2019, Middle: 2020, Right: Change)

Atmospheric warming was observed in the post-lockdown timescale with 1.74±0.004 W/ m^2 (2015) and 1.97±0.003 W/ m^2 (2019). The average ADRF in that timescale was found to be 1.98±0.007 W/ m^2. The spatial distribution shows that the lower values are towards the Am and Cwb regions, while higher values are in the BSh and Aw climate regions. The distribution might be attributed to the occurrence of monsoon precipitation and the trapping up of heat due to the dispersion of clouds without precipitation. The ADRF during the pre-lockdown, lockdown, and post-lockdown of 2020 was found to be -4.41±0.06, -1.09±0.04, and 2.34±0.02 W/ m^2, respectively. It was observed to have an atmospheric warming of approximately 0.4 W/ m^2 in the period after the lockdown of 2020 compared to the average of 2015-2019. The ADRF for the entire year of 2020 has shown warming of approximately 1.32 W/ m^2 in the study area compared to the average of the past five years. This may be due to the dilution of aerosols in the atmosphere or the excess formation of cloud condensation nuclei.

According to Fig 5.6, nearly 74% of the study area experienced a decrease in ADRF during the pre-lockdown period of 2020 compared to the average of 2015-2019. The decrease in

ADRF ranged from 0 to 1.7 W/m^2, while the increase in the remaining 26% of the study area ranged from 0 to 0.83 W/m^2. The decrease was more prominent in tropical savanna and warm semi-arid regions, such as Amravati, Medak, Adilabad, and Nagpur. In contrast, the increase was seen in humid regions and a part of the tropical monsoon region, including Kochi, Goa, Coimbatore, and Idukki.

However, the situation changed drastically during the lockdown period. Almost 98% of the study area showed an increase in ADRF during the lockdown of 2020 compared to the average of 2015-2019. The rise in ADRF fluctuated between 0-2.32 W/m^2, while the fall fluctuated between 0 to 0.23 W/m^2. The spatial distribution of ADRF shows that the increase was distributed across all five climate zones of the study area, but the decrease was concentrated only in the small coastal part of the tropical savanna region, including Tirupati, Visakhapatnam, Araku, and Chennai. A part of the fall was also distributed to the humid subtropical region. During the post-lockdown period, nearly 93% of the study area experienced an increase in ADRF ranging from 0 to 1.21 W/m^2, while the remaining part saw a decrease in ADRF ranging from 0 to 0.21 W/m^2. The reduction in ADRF was seen in most of the western and eastern ghats, while the increase was seen in the landlocked part of the study area, which consists of most of the Telangana state. The decrease in the coastal parts of the tropical monsoon and savanna regions might be attributed to the onset of the south-west monsoon season.

5.7 Spatial Distribution of Temperature in the Atmosphere

Theoretically, temperature is supposed to follow the trend of ADRF. The average temperature in the pre-lockdown timescale of 2019 in the study area was 25.20±0.005 °C, which was higher than that of 2015 (24.34±0.006 °C). The increase in temperature during the lockdown timescale between 2015 and 2019 was ~1.3 °C, which was contrary to the context of ADRF. From the analysis, ADRF during the abovementioned two timescales was found to result in the cooling of the atmosphere, but the temperature did not follow the pattern of ADRF. This might be due to the formation of aerosol nuclei that support cloud formation and precipitation. There was a minimum uplift of temperature of the order of ~0.15 °C corresponding to an increase in ADRF of ~0.35W/m^2 in the post-lockdown timescale of 2019 compared to 2015. The overall temperature was found to increase by 0.43 °C with respect to a change in ADRF by ~0.08W/m^2 in 2019 against the dataset of 2015.

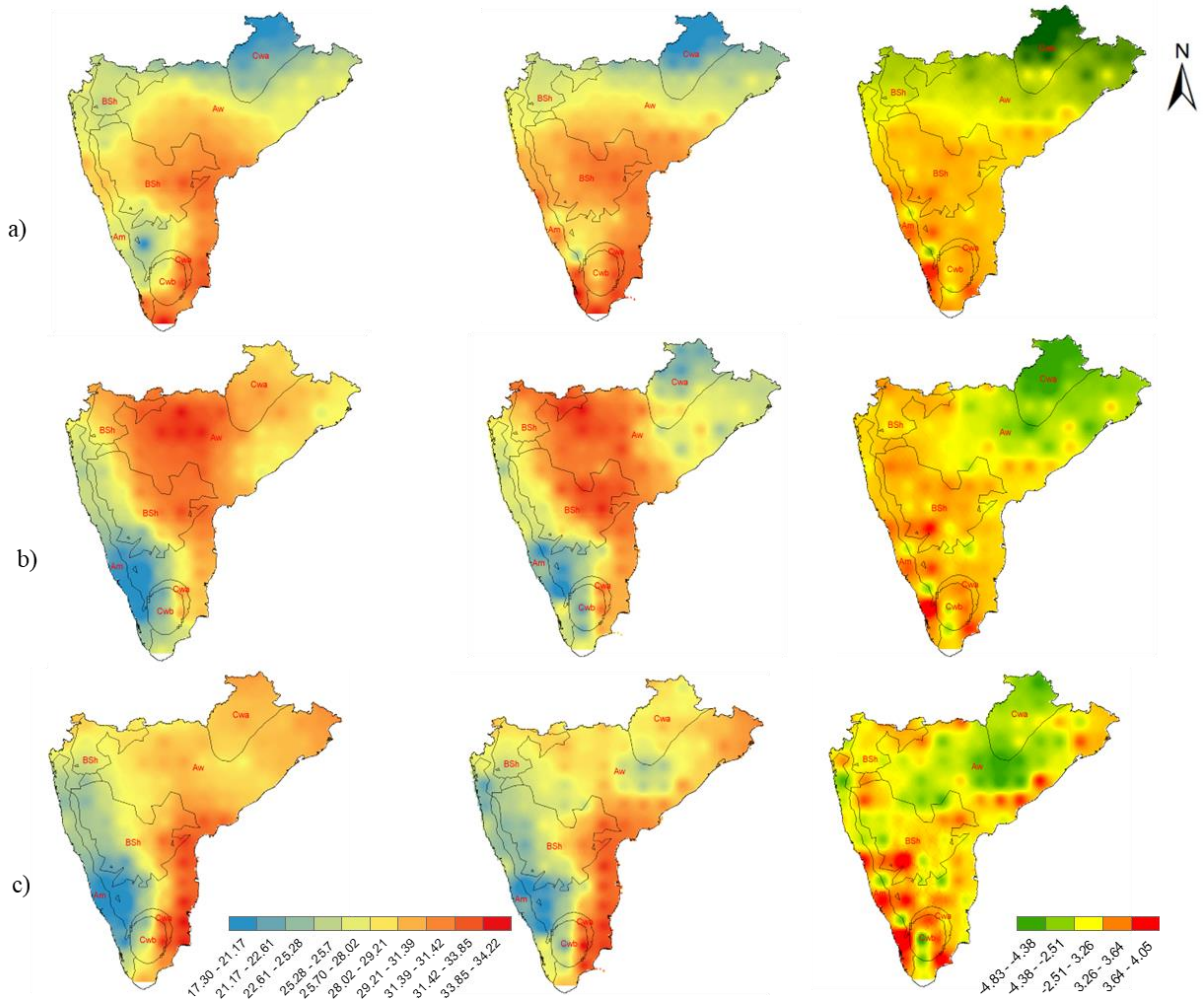

Fig 5.6: Spatial distribution of mean temperature for a) Pre-lockdown b) Lockdown c) Post-lockdown time periods (Left: Avg of 2015-2019, Middle: 2020, Right: Change)

The decline in temperature by ~0.6 °C was in accordance with the decrease in ADRF in the period prior to the lockdown of 2020 compared to the average of 2015-2019. The temperature in the lockdown timescale was 31.40±0.009 °C and 30.77±0.009 °C for the average of 2015-2019 and 2020, respectively. It shows a decrease of 0.63 °C, which was in consonance with the pattern of ADRF. The post-lockdown of 2020 witnessed a mild decrease in temperature by ~0.50 °C compared against the average of 2015-2019. On the contrary, ADRF was found to escalate in the same timescale. The overall temperature in 2020 was 26.64±0.004 °C and in the average of 2015-2019 was 27.02±0.008 °C. There was a mild reduction in overall temperature in 2020 which might be attributed to the lockdown restrictions due to the COVID-19 pandemic. However, the ADRF was found to uplift by ~1.3W/m^2 in 2020 compared against the average of 2015-2019. This might be due to the entrapment of aerosols in the upper layers of the atmosphere. The presence of absorbing aerosols in the upper layers

of atmosphere leads to absorption of solar radiation which in turn warms up the atmosphere. The increase in radiative forcing might be attributed to such phenomenon in 2020.

During the pre-lockdown period, about 56.7% of the study area experienced a decrease in temperature in 2020 compared to the average of 2015-2019 (Fig 5.6). The decrease ranged from 0-4.8°C, while the increase in the rest of the study area ranged from 0-4.04°C. The decrease was most prominent in the tropical savanna region, including major cities like Mumbai and Bengaluru, as well as a part of the warm semi-arid region covering Hyderabad and the humid subtropical region covering Raipur and Korba. Nearly 73% of the study area experienced a decline in temperature during lockdown in 2020 compared to the average of 2015-2019, with a range of 0-4.38°C. The remaining part of the study area saw an increase in temperature ranging from 0-3.64°C. The increase was most prominent in the warm semi-arid region around Hyderabad and a part of the tropical monsoon region including Pune and Goa. Meanwhile, the decrease was most prominent in the tropical savanna region including Vizianagaram and Srikakulam, as well as a part of the humid subtropical region covering Raipur and Raigarh.

During the post-lockdown period, an 85% decrease in temperature was observed, mainly in the tropical savanna and humid subtropical regions including Salem and Raipur. The temperature decrease ranged from 0-2.51°C, while the increase in the 15% of the study area ranged from 0-3.26°C. The increase was seen in parts of the tropical monsoon region including Uttara Kannada and Goa, the tropical savanna region including Kadapa, Khammam, and Warangal, and the warm semi-arid region including Nashik, Kurnool, and Mahboobnagar.

5.8 Closure

The longwave fluxes by factorial method are used to calculate ADRF in the study area. The AOD, ADRF and temperature of 2020 are compared against the average of 2015-2019 to identify the high and low changes in five climate regions of the study area. The climatic conditions and topography led to significant changes in ADRF and temperature in Tropical Savanna and Warm Semi-arid climate regions. Further, the study is extended to understand the effect of AOD on precipitation and also the factors causing EPEs in metropolitan cities which is presented in the consecutive chapter.

CHAPTER 6

IMPACT OF AOD ON CLOUD FRACTION AND PRECIPITAION

6.1 General

The AOD can change the lifetime of clouds by suppression of cloud droplets or by invigorating the formation of CCN. The greater number of aerosols lead to smaller cloud droplets which in turn results in less precipitation. If the same situation is encountered with favourable uplift and climate conditions, it results in more precipitation. The impact of AOD on cloud fraction in different precipitation regimes based on the atmospheric stability conditions is presented in this chapter. The parameters that cause EPEs in and around metropolitan cities is analysed and presented in this chapter.

6.2 Comprehensive Effect of AOD on CF

The changes in CF for different ranges of AOD was analysed by means of equal value plots. The AOD data was divided into 30 bins. The data ranges from 0 to 1.5 and each bin was incremented by 0.05. The average of AOD and CF data corresponding to each bin was calculated. The data was normalised by min-max scale. Expression used for the normalisation of the data is as shown in equation 6.1:

$$X_n = \frac{(X_i - X_{min})}{(X_{max} - X_{min})}, i = 1,2,3 \ldots..30 \quad (6.1)$$

Where X_n is the normalised data, X_i is the existing data, X_{min} is the minimum value, X_{max} is the maximum value. The AOD and CF are normalised by using the Eq (6.1). The scatterplot of normalised data with reference line is then plotted to obtain the equal value plot between

AOD and CF. The reference line is the 1:1 line which is obtained by joining the corresponding minimum and maximum of AOD and CF. Although the equal value plots are prepared for each cumulative dataset of three rainfall regimes, the plots that have points closer to the reference line are shown in this chapter.

The equal value plots for different rainfall regimes which possess points closer to the reference line are shown in the Fig 6.1. The equal value plots were better for cumulative 10-year dataset for all the three rainfall regimes. The Fig 6.1a corresponds to the equal value plot of light rain regime. The scaled values of AOD have a widespread in the range of 0-1 but the scaled values of CF are much concentrated in the range of 0.4-0.6. The plot appears to be closer towards the reference line when AOD was in the range of 0.6-0.8 and CF being greater than 0.5. Most of the points are biased towards cloud fraction. The equal value plot of moderate rain regime is shown in Fig 6.1b.

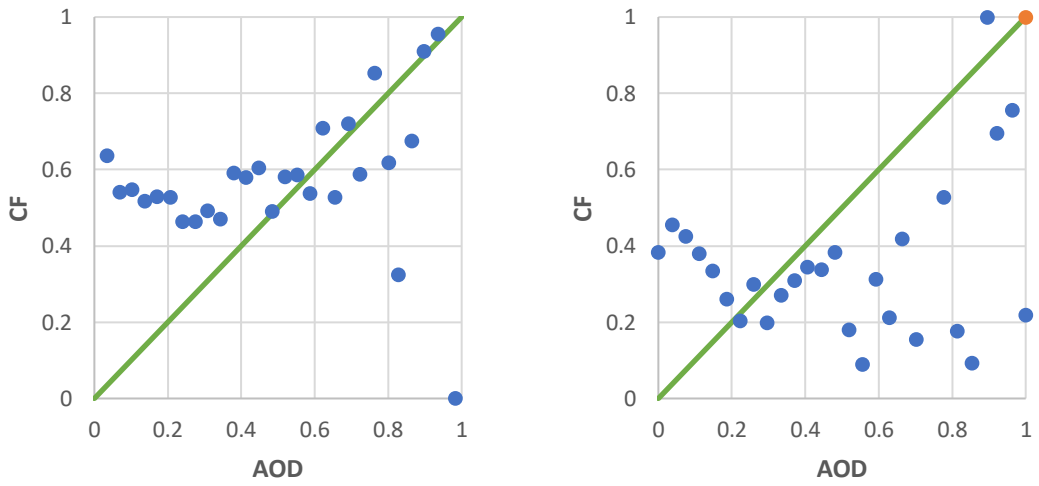

a) b)

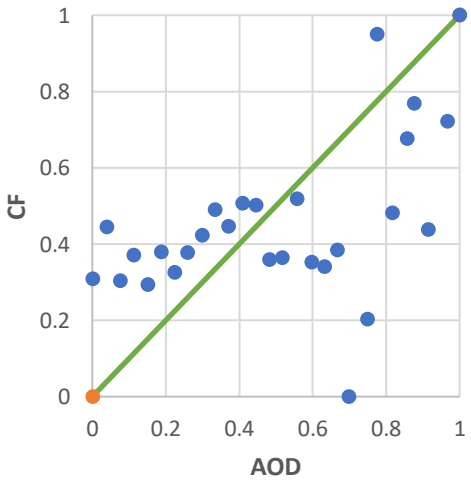

c)

Fig 6.1: Equal Value Plots of AOD and CF for a) light rain b) moderate rain c) heavy rain (The orange line shows the 1:1 line)

The scaled values of CF are in the range of 0.2-0.4 for moderate rain regime which says that the vertical development of clouds does not influence the intensity of moderate rain. The plot showed that the points with AOD and CF in the range of 0.2-0.4 are much closer to the reference line and the CF appears to be staggered with increase in AOD. It was observed that low AOD might result in low CF and increase in AOD does not influence the formation of clouds for moderate rain regime. Equal value plot for heavy rainfall regime is shown in Fig 6.1c. The cluster of points closer to the reference line has the AOD and CF in the range of 0.2-0.6. The CF does not follow a pattern once the AOD crosses 0.6. It was difficult to assess the development of clouds at various ranges of AOD greater than 0.6 in moderate and heavy rainfall regimes. Therefore, an attempt was made in this study to understand the relationship between AOD and CF based on atmospheric stability.

6.3 Observed relationship between AOD and CF based on atmospheric stability

The Fig 6.2 depicts the effect of AOD on CF for cumulative monsoon data corresponding to light rain. The atmospheric stability conditions had a greater impact on cloud coverage in the region than aerosol loadings. Furthermore, as AOD increased, the CF was found to have reached a maximum level at various K-indices. The K-index meteorology states that there are higher chances of precipitation when the atmosphere is highly instable i.e. when the K-index is on the higher range (https://www.weather.gov/lmk/indices). When the AOD is greater than one, the CF at $20^{o}C<K<25^{o}C$ was found to be the smallest for cumulative satellite observations. This could imply that the absorbing aerosols are in the lower layers of atmosphere. It could also indicate that the aerosols in the upper levels have absorbed solar radiation and heated up the atmosphere, thereby making the atmosphere stable (Constantino et al., 2013, Jing et al.,2018).

Cloud coverage at $K>35^{o}C$ was found to be greater for different bins of AOD. This indicates that when the atmosphere is unstable, clouds that could lead to precipitation are visible. The effect of AOD on CF for cumulative monsoon data corresponding to moderate rain is shown in Fig 6.3. The cumulative 5-year data shows that there was no data corresponding to the scattered and widely scattered thunderstorm states. An abrupt increase in CF was observed for AOD greater than one which might be attributed to the presence of absorbing aerosols. However, the CF was found to decrease for numerous thunderstorm state (K>35) when AOD was greater than one for cumulative 10-year and 15-year data. This indicates that the type of aerosol has influenced cloud formation (Varpe et al.,2022, Takahashi et al.,2018). When

compared to light rain, the CF corresponding to moderate rain followed an opposite order for all atmospheric stability states.

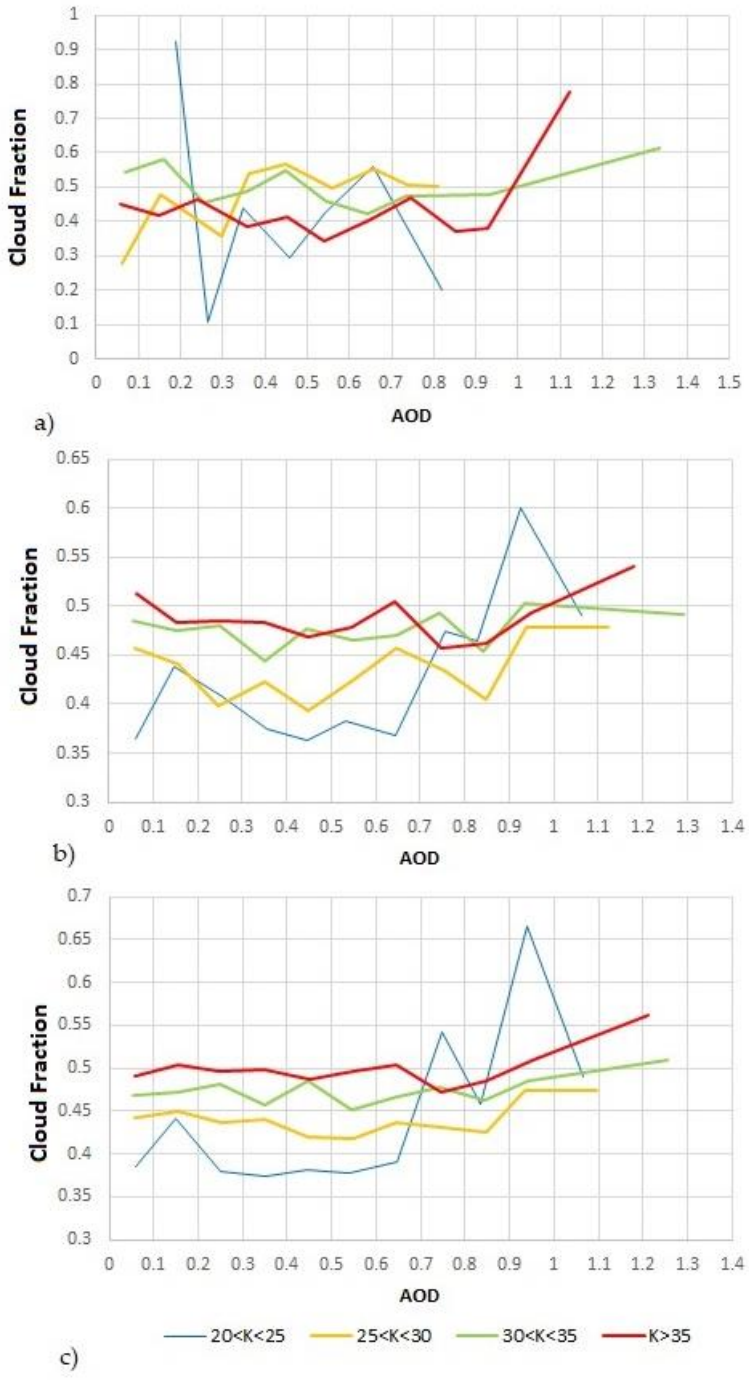

Fig 6.2: The effect of AOD on CF for various atmospheric stability states associated with light rain a) 5-year data b) 10-year data c) 15-year data

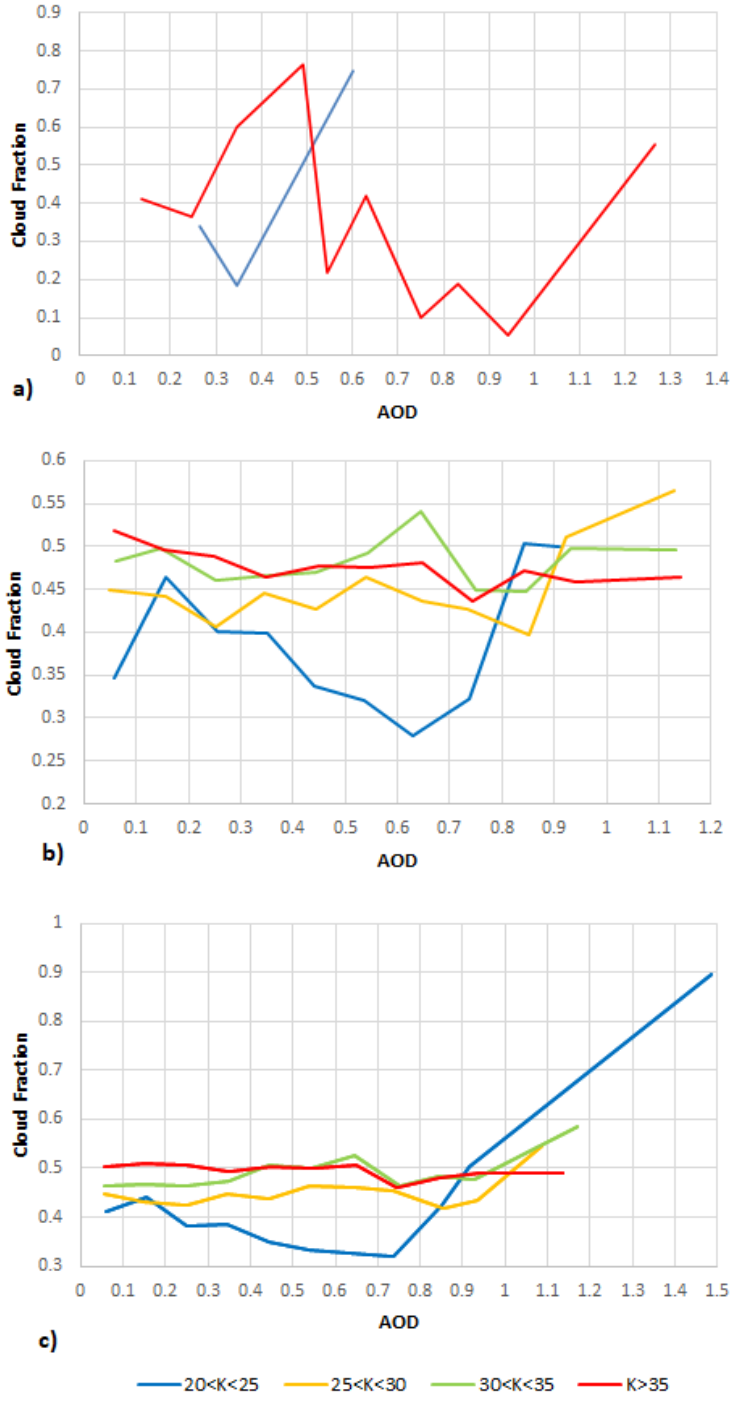

Fig 6.3: The effect of AOD on CF for various atmospheric stability states corresponding to moderate rain a) 5-year data b) 10-year data c) 15-year data

Fig 6.4: The effect of AOD on CF for various atmospheric stability states associated with heavy rain a) 5-year data b) 10-year data c) 15-year data

The Fig 6.4 shows the effect of AOD on CF for cumulative datasets from heavy rain regime. For the cumulative 5-year dataset, it was observed that there was a drop in CF for isolated, widely scattered and scattered thunderstorm state in the AOD range of 0.2-0.3. On the contrary, the CF has a peak that corresponds to a number of thunderstorm states in the same range of AOD. When AOD is in the range of 0.5-1, the CF decreases for the isolated thunderstorm state and rises for all the other three atmospheric stability states. The CF is found to increase abruptly for a variety of thunderstorm states with AOD greater than one. The cumulative 10-year dataset revealed similar results. The analysis on cumulative 15-year period shows that the CF increases gradually for all the atmospheric stability states in low range of AOD. There was no fixed pattern in the moderate range of AOD. But, for higher AOD there was an increase in CF corresponding to scattered and numerous thunderstorm states.

The Table 6.1 shows the correlation between AOD and CF at different K-indices for cumulative datasets. There is a positive significant correlation between AOD and CF regardless of atmospheric stability (Varpe etal.,2022, Zhang etal.,2022). Also, at higher values of K-index, the correlation between AOD and CF was found to be the highest for all the three cumulative datasets. This indicates that aerosol have an influence on the process of cloud development, which may result in precipitation. The table shows that the correlation between AOD and CF has gotten stronger as the number of samples increased, regardless of atmospheric stability. The correlation between AOD and CF was found to be highest and most significant in isolated thunderstorm states, indicating an appreciable increase in cloud cover in the light rain regime. The correlation was nearly identical but insignificant for scattered thunderstorm state and numerous thunderstorm states in light rain regime.

Table 6.1: AOD and CF correlation coefficients for various atmospheric stability states

K-index	**Light rain**			**Moderate rain**			**Heavy rain**		
	5 years	**10 years**	**15 years**	**5 years**	**10 years**	**15 years**	**5 years**	**10 years**	**15 years**
20<K<25	-0.35	**0.669**	**0.653**	0.878	0.200	**0.703**	-0.422	-0.383	-0.464
25<K<30	**0.628**	0.386	0.351	-	0.540	0.476	**0.764**	**0.596**	**0.662**
30<K<35	0.131	0.287	0.509	-	0.080	**0.633**	0.28	0.306	0.283
K>35	0.401	0.208	0.499	-0.250	**-0.711**	-0.555	0.385	0.083	-0.061

Note: Bold values indicate statistically correlated values at 5% level of significance)

This stipulates the vertical formation of clouds, which might or might not result in precipitation (Constantino et al., 2013, Liu et al., 2020). When K>35 for all cumulative datasets, there was a negative correlation between AOD and CF in the moderate rain regime.

For cumulative 15-year data, the correlation was strongest and most significant for isolated thunderstorm states and widely scattered thunderstorm states. This indicates that the atmospheric stability conditions influenced cloud formation. For isolated thunderstorm states, the correlation between AOD and CF for heavy rain regimes was found to be negative. For all three cumulative datasets in the heavy rain regime, the correlation corresponding to widely scattered thunderstorm state was maximum and significant. For scattered and numerous thunderstorm states in the heavy rain regime, the correlation decreases as the time period increases.

6.4 Overall effect of AOD on CF and Precipitation

The Fig 6.5 depicts the overall effect of AOD on CF and Precipitation in the light rain regime for three cumulative datasets. For three cumulative datasets, it was observed that for a constant bin of AOD, precipitation was greater while CF falls, and vice versa. This suggests that AOD influences the vertical development of clouds. When AOD is greater than one, the maximum values of CF and precipitation have been discovered. This means that the effect of aerosols on clouds was dominated by the local weather conditions. Precipitation is found to be inversely proportional to CF in the cumulative 5-year dataset. However, as the number of samples increases, precipitation becomes more positively correlated with AOD. According to the overall analysis, precipitation was nearly statistically independent of AOD but dependent on CF. The correlation of precipitation with AOD was observed to be weak when compared to that of CF.

The overall effect of AOD on CF and Precipitation in moderate rain regime for three cumulative datasets is shown in Figure 6.6. When AOD is in between 0.5 and 1, precipitation and CF have an inverse relationship, which meant that when precipitation is higher, CF falls. Precipitation and CF were found to increase when AOD was greater than one for a cumulative 5-year dataset. The observation was, however, inverse for the cumulative 15-year dataset. Precipitation increased in the moderate rain regime, while CF decreased in the cumulative 5-year and 10-year datasets before increasing in the cumulative 15-year dataset. The correlation of precipitation and CF with AOD was observed to be weak.

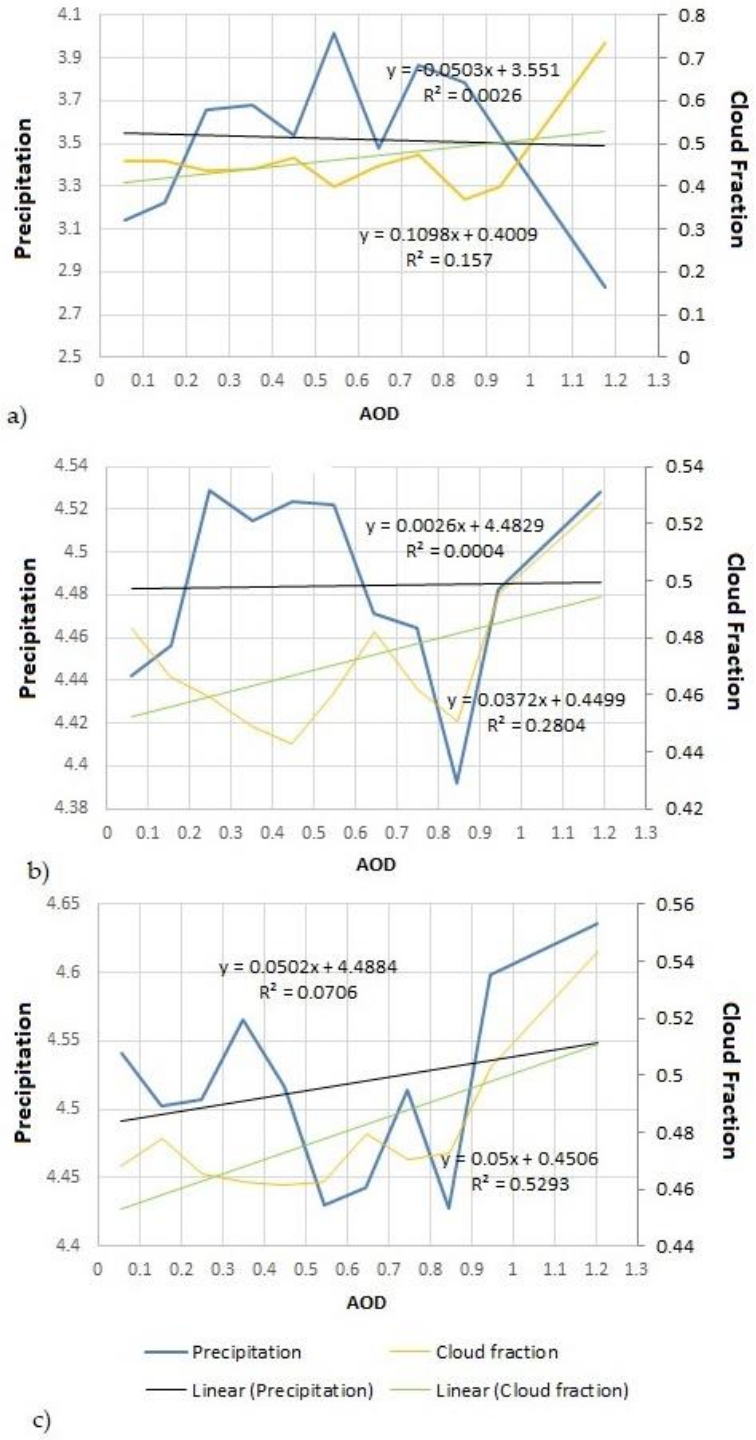

Fig 6.5: The overall effect of AOD on CF and precipitation for light rain a) 5-year data b) 10-year data c) 15-year data (Regression equations for precipitation and CF are given in the upper and lower part of each figure, respectively)

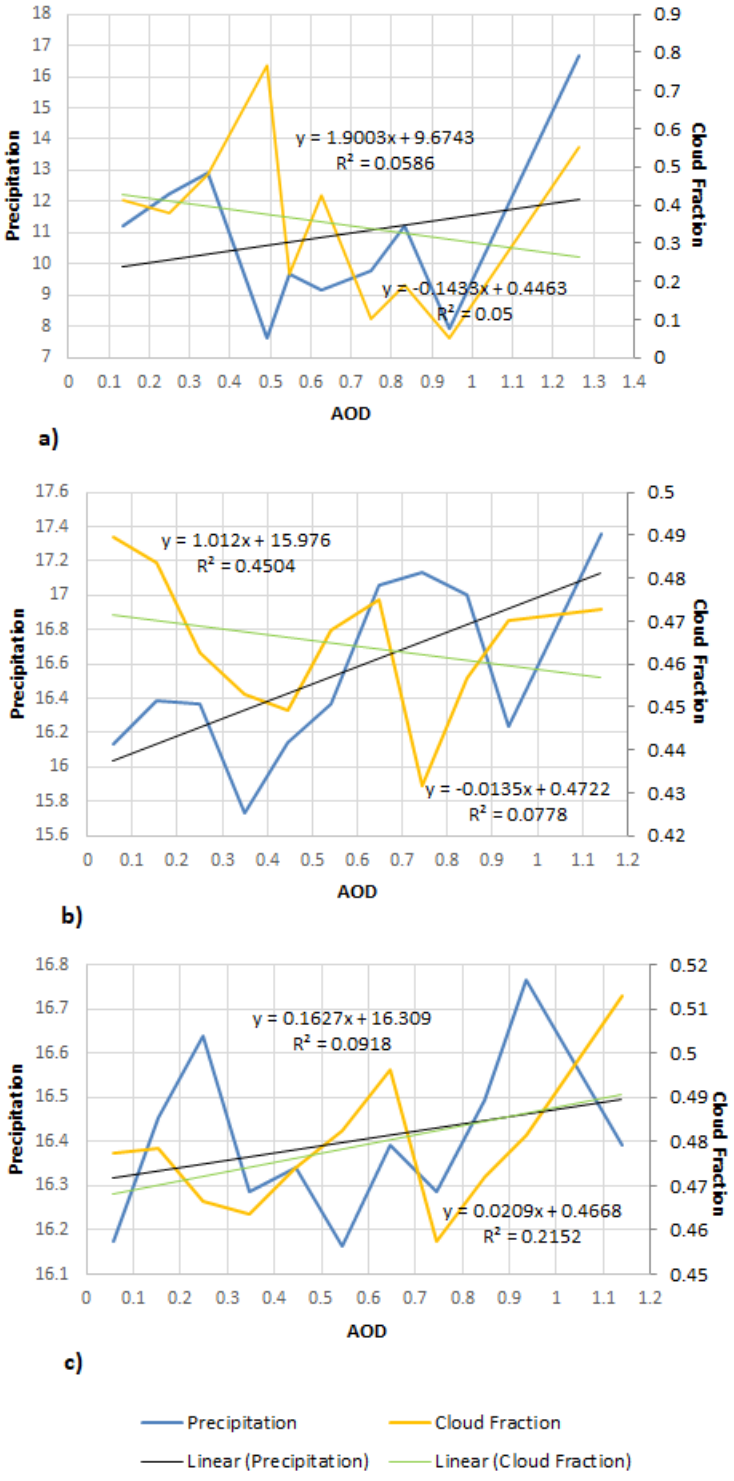

Fig 6.6: The overall effect of AOD on CF and precipitation for moderate rain a) 5-year data b) 10-year data c) 15-year data (Note: Regression equations for precipitation and CF are provided in the upper and lower parts of each figure, respectively)

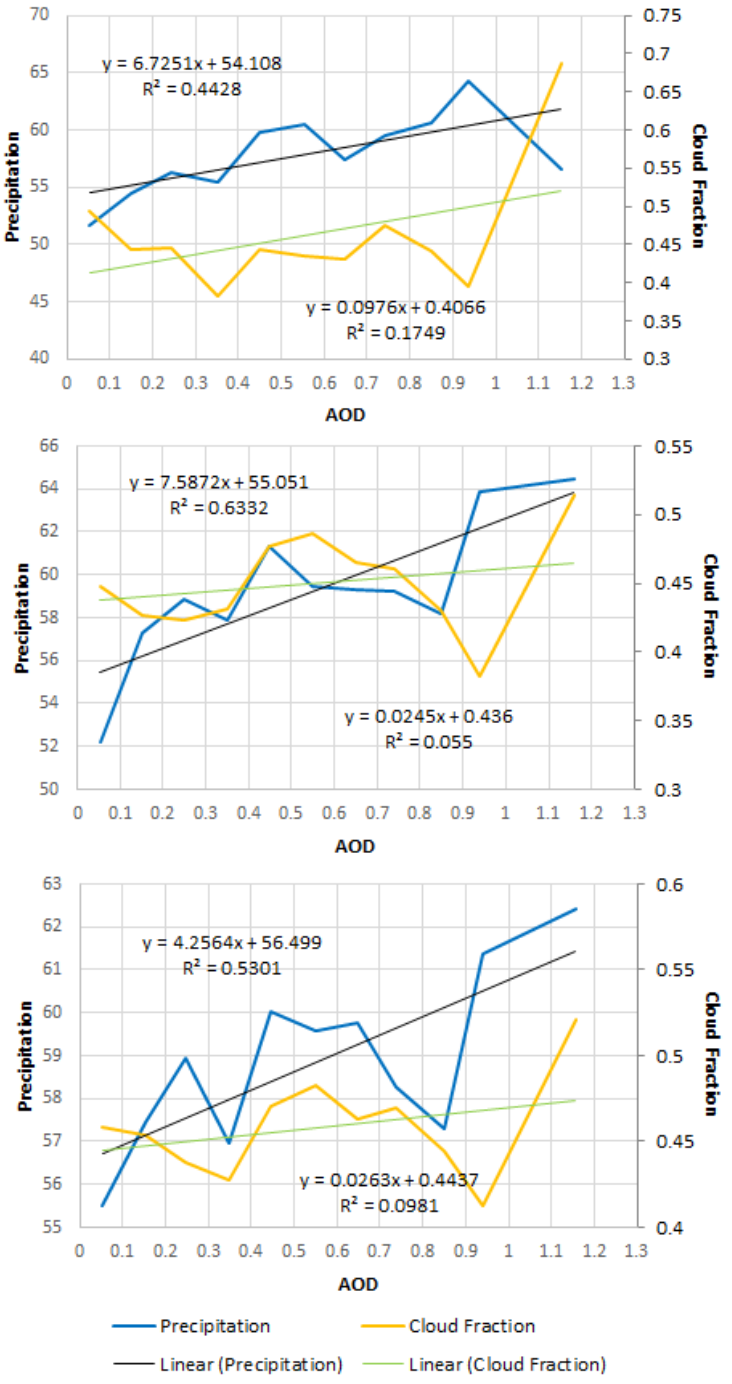

Fig 6.7: The overall effect of AOD on CF and precipitation for heavy rain a) 5-year data b) 10-year data c) 15-year data (Note: Regression equations for precipitation and CF are provided in the upper and lower parts of each figure, respectively)

Figure 6.7 depicts the overall effect of AOD on CF and precipitation in the heavy rain regime for three cumulative datasets. Precipitation and CF had a direct relationship over a 5-year period, corresponding to a low range of AOD. In the moderate and high ranges of AOD, the relationship has become inverse. In the cumulative 10-year period, precipitation and CF follow a similar pattern for low and moderate AOD ranges. However, for higher AOD, both parameters were discovered to have an inverse relationship. In the cumulative 15-year dataset, precipitation has a peak and CF has a dip for a constant bin in the moderate range of AOD. In the cumulative 15-year dataset, the parameters have a direct relationship for a wider range of AOD. The correlation of precipitation with AOD was strong when compared to that of CF.

6.5 Spatial distribution of AOD and CF

The Fig 6.8 depicts the distribution of AOD and CF in the study area's light rain regime. From Fig 4.2, the majority of the study area was classified as low polluted. Nearly 173 lakh ha of low-polluted land was covered by tropical savanna climate, while 107 lakh ha was covered by warm semi-arid climate. The cumulative 10-year and 15-year data show a similar pattern. The distribution of AOD increased with the number of samples collected in low-polluted areas. On the contrary, AOD distribution has decreased in moderately polluted areas. In the humid subtropical region, the AOD distribution corresponding to the low polluted region has nearly quadrupled, according to the Koppen climate classification. However, in the moderately polluted region, AOD has decreased by 50% over a 15-year period.

Nearly 182 lakh ha of the region in tropical savanna climate had moderate CF based on 5-year data. Fig 6.8 shows that the majority of the low-polluted region has a tropical savanna climate, followed by a warm semi-arid climate. The CF, on the other hand, has a moderate to high distribution in the majority of tropical savanna regions, followed by warm semi-arid regions. Fig 6.8 shows that the majority of the low and moderately polluted regions had moderate CF. For a cumulative 10-year analysis, nearly 427 lakh ha of the study area was classified as tropical savanna climate region, followed by 220 lakh ha classified as warm semi-arid climate region. According to Fig 6.8, the majority of the humid subtropical and tropical savanna region has lower AOD. Nonetheless, some areas in the monsoon region have seen low and high distributions of AOD and CF, respectively. Fig 6.8 shows that the majority of the area has a low AOD. Overall, it can be concluded that as the number of samples increased, the majority of the study area exhibited AOD in the range of 0-0.5. Similarly, the CF was in the 0.8-0.9 range.

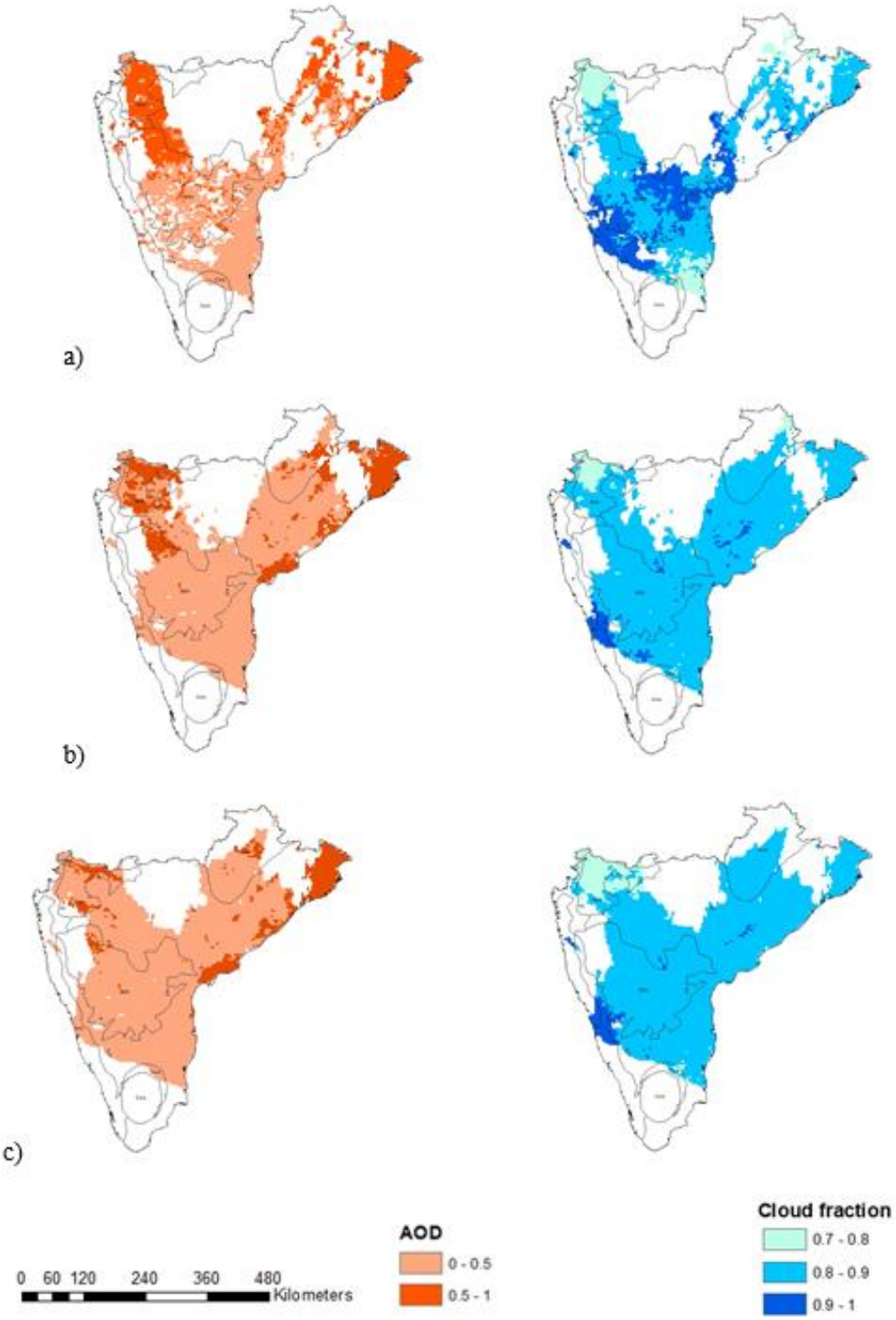

Fig 6.8: Spatial distribution of AOD and CF in the light rain regime for cumulative data a) 5-year b) 10-year and c) 15-year

Fig 6.9 depicts the spatial distribution of AOD and CF in the moderate rain regime. In a 5-year period, the majority of the tropical savanna region of 158 lakh ha experienced low pollution, followed by humid subtropical climate and subtropical oceanic highland climate. The cumulative 10-year and 15-year time periods were treated in the same manner. For all three cumulative time periods, moderate pollution was observed in tropical savanna climate and humid subtropical climate regions. Fig 6.9 also shows that the area with low pollution for cumulative 10-year and 15-year data has increased, while the area with moderate pollution has decreased significantly. The main reason for changes in AOD distribution can be attributed to mitigation and adaptation measures implemented by the Indian government, as mentioned in the IPCC climate change reports from 2001 and 2014. (Metz et al., 2001; Edenhofer et al., 2015) The moderate CF was nearly the same for all climate regions with 10-year and 15-year data.

The spatial distribution of AOD and CF in the heavy rain regime is depicted in Fig 6.10. Tropical savanna climate has the lowest AOD distribution across all three cumulative datasets, followed by subtropical oceanic highland climate. For all five climate regions corresponding to heavy rain, the area with moderate AOD distribution was the smallest. In the spatial distribution, the higher range of CF was limited. The majority of the population in the study area had moderate CF and low AOD. For all three cumulative datasets, the distribution of CF was most noticeable in the tropical savanna region, followed by the humid subtropical climate region.

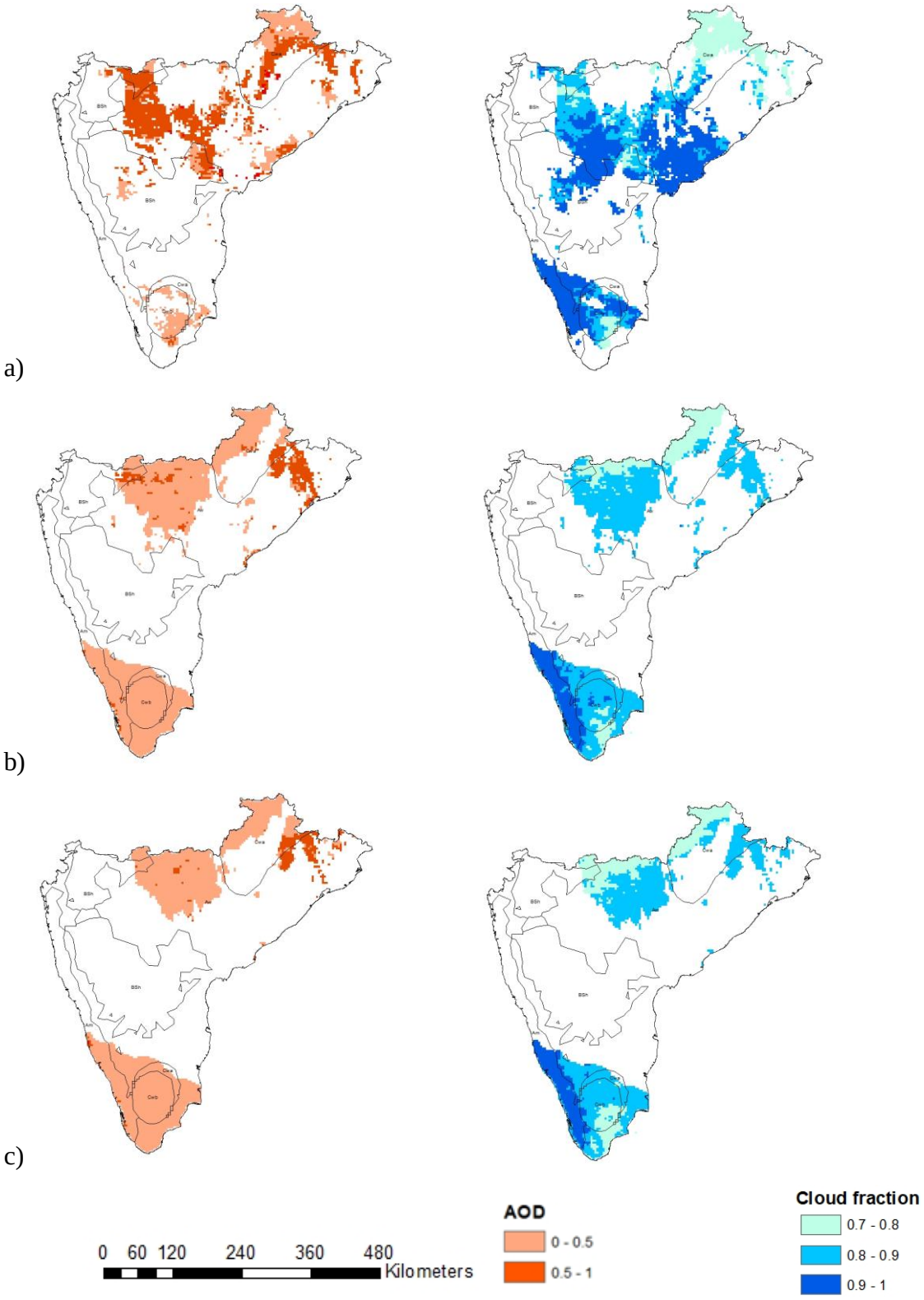

Fig 6.9: Spatial distribution of AOD and CF in the moderate rain regime for Cumulative data a)5-year b)10-year and c)15-year

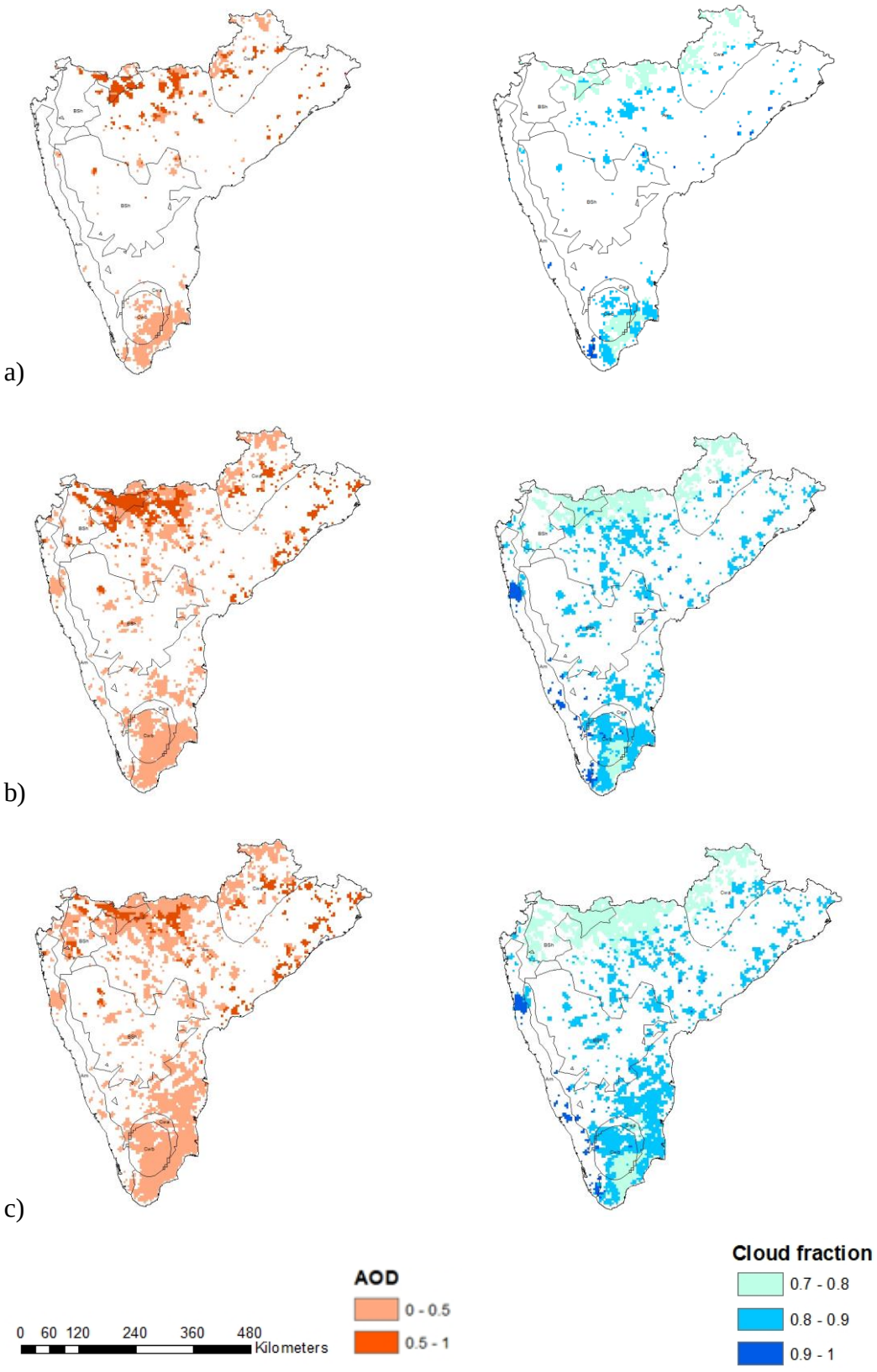

Fig 6.10: Spatial distribution of AOD and CF in the heavy rain regime for cumulative data a)5-year b)10-year and c)15-year

1

The Table 6.2 depicts the area under each climate region corresponding to light rain for cumulative data analysis. For low AOD distribution, the tropical savanna climate experienced an 11% and 13% increase in distribution for cumulative 10 and 15-year data, respectively. The tropical savanna climate, on the other hand, has seen a decrease of 47% and 75% distribution for cumulative 10 year and 15-year data, respectively, for the moderate distribution of AOD. For both cumulative periods, the increase in moderate CF is on the higher end of the order of 35% for warm semi-arid climate. In contrast, the higher CF range has seen a decline of the order of 13% and 19% for cumulative 10 and 15-year data, respectively.

The areal distribution of AOD and CF in the study area for moderate rain is shown in Table 6.3. For cumulative 10-year and 15-year data, the tropical savanna climate has seen an increase in lower AOD of about 50% and 70%, respectively. For the same climate region, moderate AOD has decreased by 35% and 39%, respectively. Lower AOD has increased by 26 percent and 42 percent for cumulative 10-year and 15-year datasets in the humid subtropical climate region. The moderate AOD decreased by 40% and by 55%, respectively. The cumulative 10-year and 15-year datasets revealed a 35 percent increase in moderate CF in the tropical savanna climate region. The higher end of CF, on the other hand, has declined by approximately 8%. The humid subtropical climate region, on the other hand, has seen a 1% and a 20% decrease in the cumulative 10-year and 15-year datasets, respectively.

The Table 6.4 shows the areal distribution of AOD and CF in the study area's heavy rain regime. For the cumulative 10-year and 15-year datasets, the tropical savanna climate has seen three and five times lower AOD, respectively. For the cumulative 10-year and 15-year datasets, the humid subtropical climate has increased twice and nearly three times. A similar observation was made for the moderate distribution of AOD. Lower CF in the tropical savanna climate region increased by 72% over a 10-year period. Lower CF have increased by 56% and 89% in the humid subtropical climate region, respectively. When compared to a cumulative 5-year dataset, moderate CF increased nearly threefold in all climate regions.

Table 6.2: Areal distribution of AOD and CF for each climatic region under light rain in 100,000 ha

Climatic region			Cwb	Cwa	BSh	Am	Aw
5-year	**Low**	**AOD**	1.256	15.75	107.6	173	5.023
10-year			-	54.867	193.388	356.252	11.302
15-year			-	60.18	219.566	406.966	11.302
5-year	**Moderate**		-	21.348	76.216	103.07	1.159
10-year			-	12.075	48.878	93.313	0.29
15-year			-	6.762	20.672	73.028	0.29
5-year	**Low**	**CF**	0.869	15.069	28.593	38.736	0
10-year			-	5.892	21.058	4.443	0
15-year			-	3.961	37.19	19.416	0
5-year	**Moderate**		0.386	22.121	120.84	181.6	1.159
10-year			-	61.146	220.05	427.73	0.193
15-year			-	63.078	200.73	449.47	0.193
5-year	**High**		-	0.097	71.29	79.02	11.21
10-year			-	-	2.222	20.479	11.592
15-year			-	-	2.995	13.524	11.592

Table 6.3: Areal distribution of AOD and CF for each climatic region under moderate rain in 100,000 ha

Climatic region			Cwb	Cwa	BSh	Am	Aw
5-year	**Low**	**AOD**	17.87	34.39	14.39	0.966	39.32
10-year			43.566	60.76	5.892	35.065	185.27
15-year			56.799	56.799	4.347	36.707	165.86
5-year	**Moderate**		0.29	26.47	24.15	0.097	105.9
10-year			0	6.472	3.961	1.835	336.26
15-year			5.892	5.892	0.097	1.352	19.609
5-year	**Low**	**CF**	5.796	53.23	7.341	0	32.75
10-year			5.12	38.156	3.381	0	31.298
15-year			10.529	30.525	4.057	0	44.918
5-year	**Moderate**		13.62	12.36	29.08	0.483	89.74
10-year			33.036	30.428	6.375	4.443	178.61
15-year			30.718	33.519	0.386	4.54	133.79
5-year	**High**		18.16	8.984	34.39	28.79	157.1
10-year			5.409	0.193	0.097	34.292	10.626
15-year			2.318	0.193	0	34.582	8.018

Table 6.4: Areal distribution of AOD and CF for each climatic region under heavy rain in 100,000 ha

Climatic region			Cwb	Cwa	BSh	Am	Aw
5-year	**Low**	**AOD**	17.19	15.46	4.057	2.029	41.83
10-year			30.332	29.076	23.473	10.626	123.84
15-year			34.679	40.474	44.628	11.688	200.83
5-year	**Moderate**		-	6.569	10.43	-	23.57
10-year			-	8.018	18.74	0.483	47.719
15-year			-	7.631	14.393	0.29	36.128
5-year	**Low**	**CF**	8.211	17.29	9.66	-	29.27
10-year			7.824	27.144	21.831	-	50.327
15-year			10.626	32.747	33.713	-	81.239
5-year	**Moderate**		8.79	4.83	4.637	0.193	33.52
10-year			21.155	10.143	19.996	2.125	117.17
15-year			23.473	15.552	25.212	2.608	152.33
5-year	**High**		0.193	-	0.193	1.835	2.898
10-year			1.352	-	0.386	8.984	4.25
15-year			0.58	-	0.097	9.37	3.381

6.6 Analysis of Causes for Extreme Precipitation Events in Urban Cities of Peninsular India

6.6.1 Mean Precipitation

The mean precipitation during EPEs in the metropolitan cities for the years 2018, 2019, and 2020 is depicted in Fig 6.11. Precipitation was highest in 2018 for all three cities, except for Mumbai. There was a decreasing trend in the magnitude of precipitation for Chennai and Bengaluru. However, mean precipitation was higher in 2019 for Mumbai and Hyderabad, and then it decreases in 2020. The increase in precipitation in 2019 in Hyderabad was also reflected in the increased number of EPEs in the city. The number of EPEs increased in 2019 compared to 2018 for all three cities, except for Hyderabad. However, EPEs also increased in Hyderabad in 2020. Most of the EPEs in 2019 occurred during the months of July, August, September, and October in the selected study area. In that year, a total of 110% of the "long-period average" (LPA), which is 880 mm, representing the national average of monsoon rains received in the 50 years prior to 2010, fell between June and September 2019 (Source: Mausam 2019).

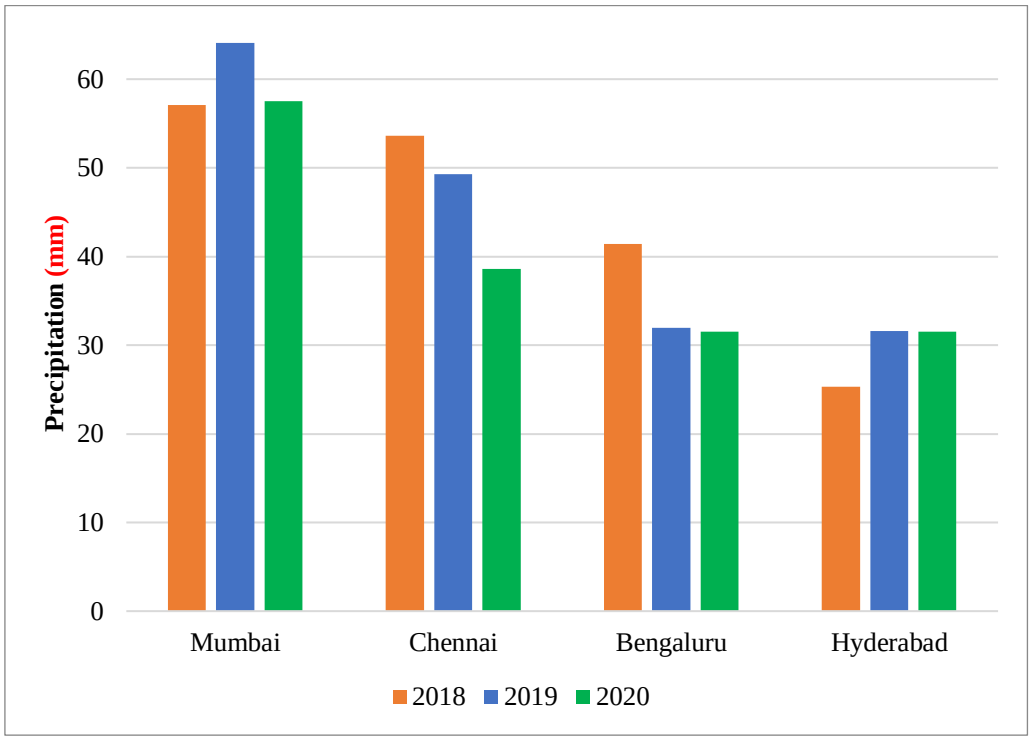

Fig 6.11: Mean Precipitation of Extreme Precipitation Events (EPEs) in the Study Area for the Years 2018, 2019, and 2020

6.6.2 Spatial Distribution Maps

6.6.2.1 Mumbai

The spatial distribution of precipitation, AOD, cloud properties, and the K-index is shown in Fig 6.12 for the selected Extreme Precipitation Events (EPEs). The precipitation map indicates that EPEs typically have precipitation in the range of 30-250 mm/day. All the other parameters in the area represent averaged values for the 10 days prior to the occurrence of the extreme event.

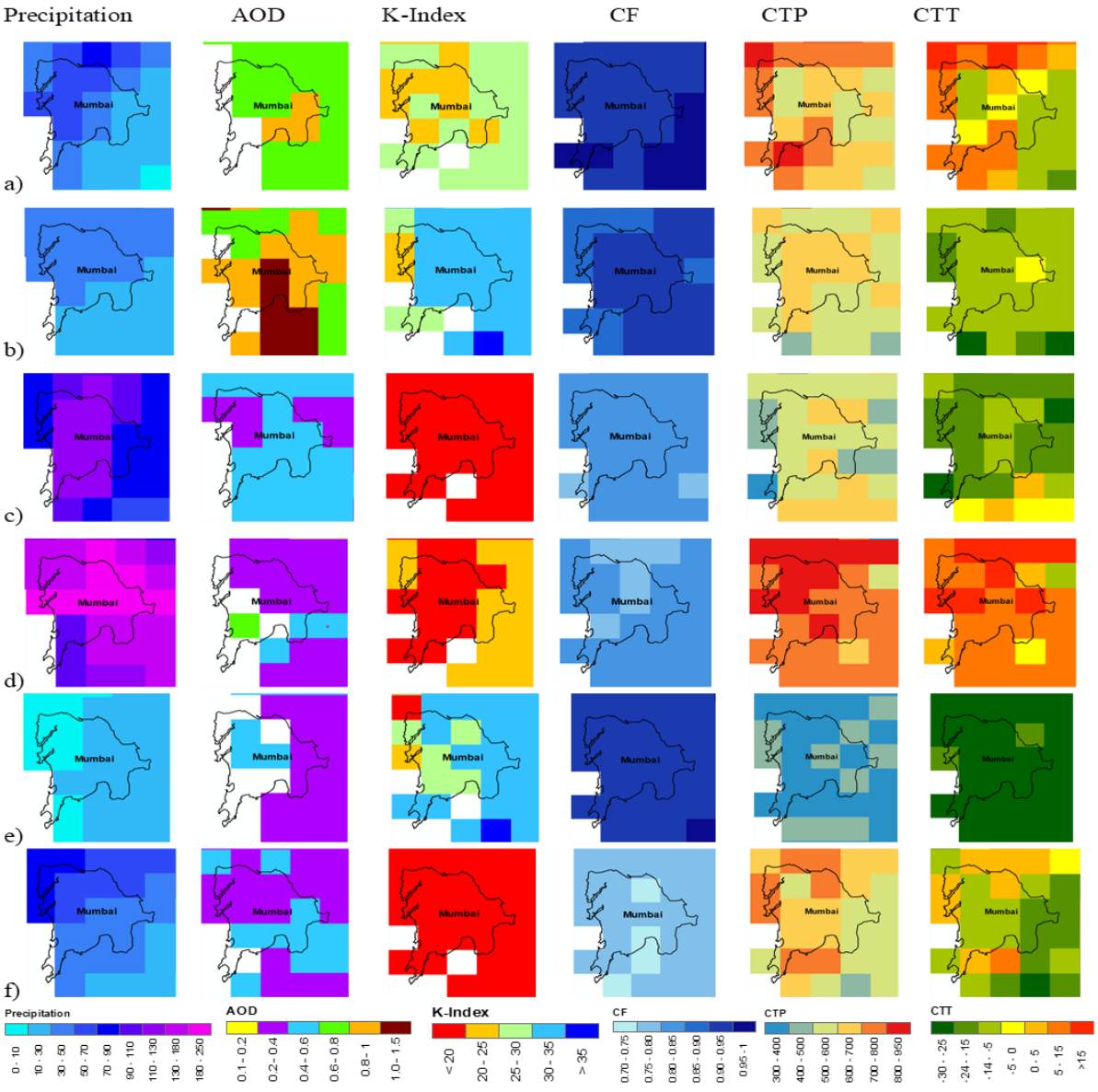

Fig 6.12: Spatial Distribution of Precipitation(mm), AOD, K-index(°C), CF, CTP (hPa) and CTT (°C) (Left to Right) for EPEs in Mumbai on a) May 25, 2018 b) Oct 4, 2018 c) Dec 3, 2019 d) May 31,2020 e) June 22,2020 f) Nov 19, 2020

For example, isolated thunderstorm conditions (20°C < K < 25°C) accompanied by AOD in the range of 0.2-0.6 resulted in precipitation exceeding 110 mm in Mumbai. Additionally, a

Cloud Top Temperature (CTT) greater than zero and a Cloud Fraction (CF) greater than 0.8 were observed in most of the EPEs in Mumbai. The distribution also shows that scattered thunderstorm conditions (30°C < K < 35°C) along with AOD in the range of 0.2-0.4 led to precipitation levels below 30 mm/day. From Fig 6.12, it can be inferred that low-level clouds (CTP > 680 hPa), CTT > 0°C, AOD in the range of 0.2-0.6, and isolated thunderstorm conditions resulted in high precipitation levels exceeding 100 mm/day in the metropolitan region of Mumbai.

6.6.2.2 Chennai

The spatial distribution of precipitation, AOD, cloud properties, and the K-index is shown in Fig 6.13 for the selected EPEs. Three out of five EPEs have experienced numerous thunderstorm states (K > 35°C) over most of Chennai city.

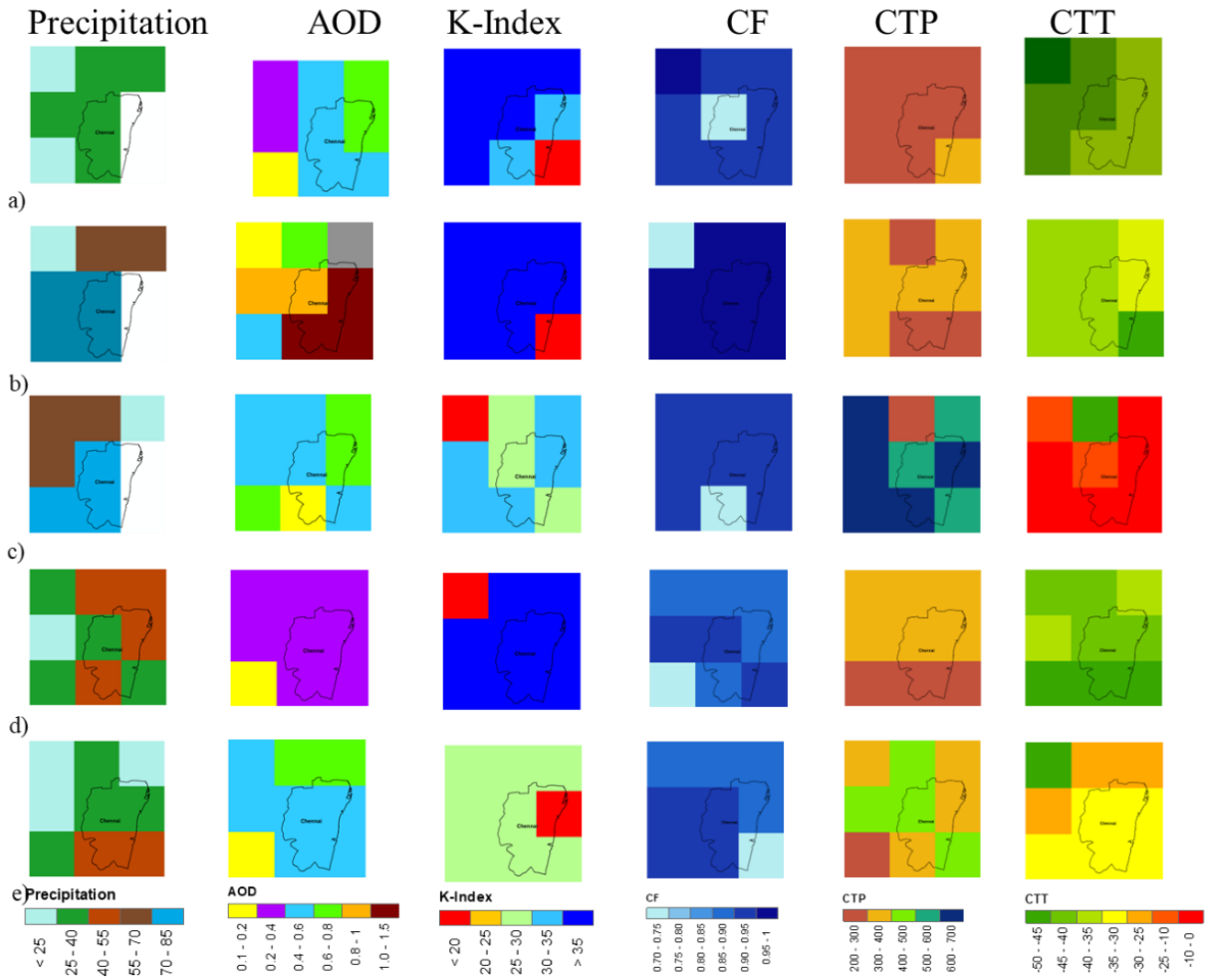

Fig 6.13: Spatial Distribution of Precipitation(mm), AOD, K-index(°C), CF, CTP (hPa) and CTT (°C) (Left to Right) for EPEs in Chennai on a) June 11, 2018 b) Aug 20, 2018 c) Sep 20, 2018 d) June 10,2020 e) Oct 10, 2020

The precipitation during those three events falls in the range of 25-85 mm per day, and AOD was in the range of 0.2-0.6. The CF appears to be greater than 0.9 in all the EPEs in Chennai. However, the CTP was low, implying that the area was covered by high-level clouds as the region extends toward the East coast of India. The CTT was less than zero in all five EPEs. But, the CTT was significantly lower in the observed three out of five EPEs that have experienced numerous thunderstorm states. Overall, it can be concluded that EPEs might take place during numerous thunderstorm states if AOD was in the range of 0.2-0.6, accompanied by low CTP and CTT being less than zero.

6.6.2.3 Hyderabad

The city of Hyderabad experienced 3, 9, and 22 EPEs in the years 2018, 2019, and 2020, respectively. AOD data was visualized for the 10 days prior to each event using ArcMap. If the data was available on those days, a stack of images was created, and the mean value was reported. The process of stacking and calculating the mean was carried out for both cloud and atmospheric products

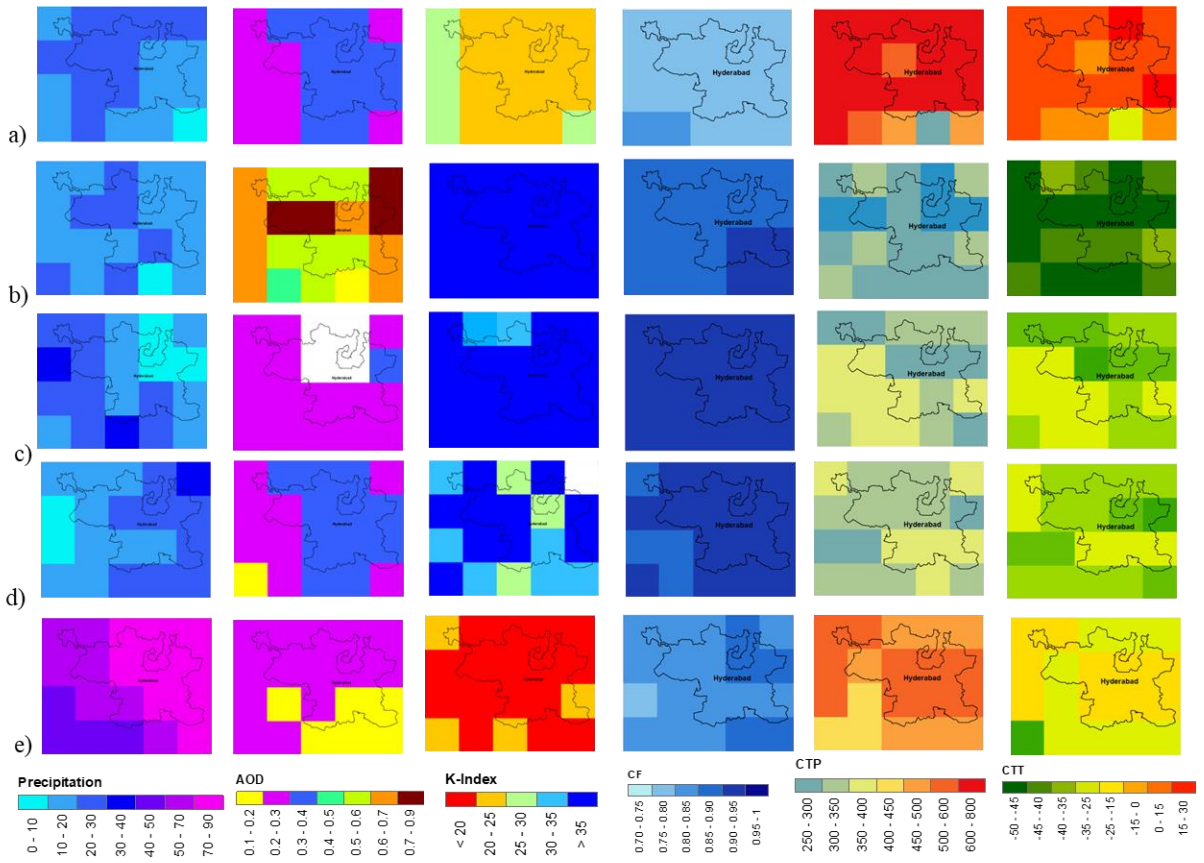

Fig 6.14: Spatial Distribution of Precipitation(mm), AOD, K-index(°C), CF, CTP (hPa) and CTT (°C) (Left to Right) for EPEs in Hyderabad on a) May 03, 2018 b) June 03, 2018 c) June 28, 2020 d) Oct 11, 2020 e) Nov 26, 2020

If AOD data was not available, the consecutive EPE was visualized. Consequently, 2 and 3 events from 2018 and 2020 had the required data for analyzing the occurrence of EPE. The spatial distribution of precipitation, AOD, cloud properties, and the K-index for the 10 days prior to the EPE is shown in Fig 6.14.

Isolated thunderstorm conditions (20°C < K < 25°C) were prevalent on May 03, 2018, and Nov 26, 2020, during the EPE. Among these, the precipitation was more pronounced on Nov 26, 2020, compared to all five EPEs in Hyderabad. However, AOD in four out of five EPEs falls within the range of 0-0.4. Numerous thunderstorm conditions (K > 35°C) were predominant in two out of five EPEs, specifically on June 03 and June 28, 2020. Nevertheless, the precipitation during these events was less than 40mm. Considering that the dates mentioned coincide with the lockdown phase in India due to the COVID-19 pandemic, it is possible that aerosols were trapped in the upper layers of the atmosphere, leading to the formation of numerous small cloud droplets. Alternatively, this might also be attributed to the onset of the monsoon season in the metropolitan city of Hyderabad.

Considering the EPE with the most precipitation, which occurred on Nov 26, 2020 (Fig 6.14e), the corresponding Cloud Top Pressure (CTP) was in the range of 450-600 hPa, and the Cloud Top Temperature (CTT) was in the range of -35°C to -15°C. The spatial pattern shows that more precipitation occurred in the presence of middle-level clouds when CTP was in the range of 500-600 hPa and CTT was in the range of -25°C to -15°C. Higher CTP (>680 hPa) and CTT (>0°C), accompanied by isolated thunderstorm conditions (20°C < K < 25°C), have resulted in lower precipitation (<30 mm), as evident from the precipitation (Fig 6.14a) on May 03, 2018. Additionally, lower CTP (<680 hPa) and CTT (<0°C), coupled with isolated thunderstorm conditions (20°C < K < 25°C) and numerous thunderstorm conditions (K > 35°C), have resulted in precipitation ranging from 20-30 mm (Fig 6.14b to 6.14d) in the city of Hyderabad. This may be attributed to the dispersion of Cloud Condensation Nuclei (CCN) from deep convective clouds. Thus, it can be inferred that higher CTP and lower CTT, along with lower Aerosol Optical Depth (AOD), may lead to higher precipitation in the metropolitan city of Hyderabad.

6.6.2.4 Bengaluru

The metropolitan city of Bengaluru experienced 14, 20, and 17 EPEs in 2018, 2019, and 2020, respectively. Unfortunately, data was only available for two events, namely, on June 07, 2019, and June 02, 2020. The spatial distribution of AOD, cloud properties, and the K-index is shown in Fig 6.15. AOD values in the range of 0.4-0.6, along with CTP (400-600 hPa) and CTT (<0°C), during numerous thunderstorm conditions (K > 35°C), resulted in precipitation

ranging from 40-60 mm, as evident from Fig 6.15a. However, low AOD (<0.4), coupled with low CTP (<400 hPa) and CTT approaching 0°C, led to precipitation of less than 30 mm in the city of Bengaluru (Fig 6.15b). Due to the limited number of EPEs available for analysis, it is not possible to conclusively determine the combination of parameters that result in low and high precipitation.

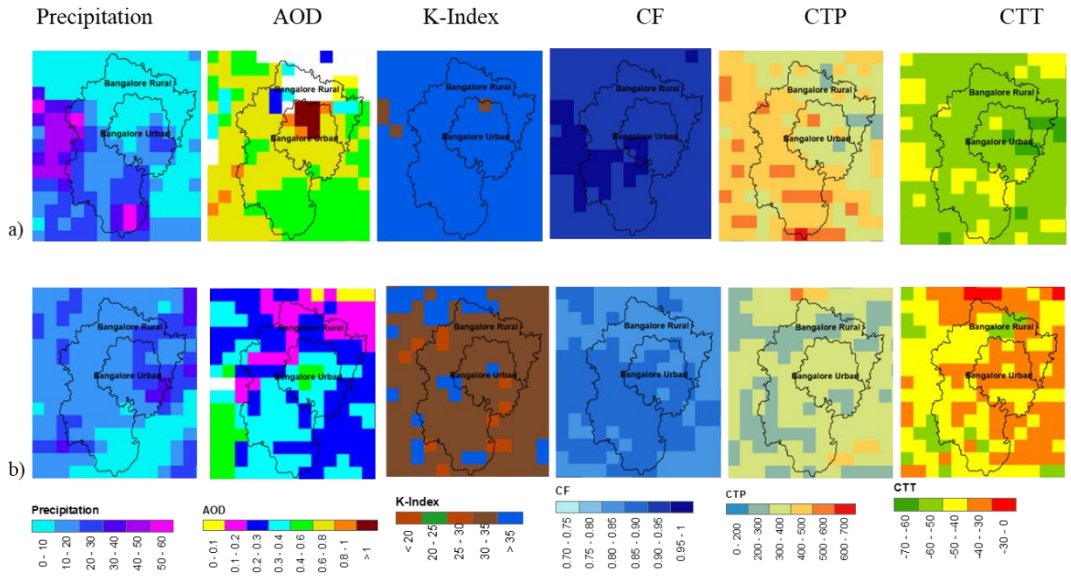

Fig 6.15: Spatial Distribution of Precipitation(mm), AOD, K-index (°C), CF, CTP (hPa) and CTT (°C) (Left to Right) for EPEs in Bengaluru on a) June 07, 2019 b) June 02, 2020.

6.6.3 Regression Analysis

The pixel values of each variable for every EPE in the metropolitan city were extracted to Excel using R Statistical software. Blank cells, which represent missing data, were removed prior to the analysis. The Excel file was then read, including the column names, and multiple linear regression analysis was performed, considering precipitation as the independent variable and aerosol, cloud, and atmospheric stability parameters as the dependent variables. The coefficients of MLR models to predict precipitation depth (in millimeters) during an EPE for each metropolitan city are given in Table 6.5.

The results showed that AOD was highly significant in predicting precipitation depths during an EPE for Mumbai and Chennai. Assuming that all other components in the regression equation are constant, Chennai receives more precipitation with an increase in AOD because the coefficient is positive, while Mumbai receives less precipitation because the coefficient is negative.

Table 6.5: Multiple Linear Regression (MLR) models for the four metropolitan cities of Mumbai, Chennai, Bengaluru and Hyderabad to predict precipitation depth during an EPE (Significance level: '***' 0.001 '**' 0.01 '*' 0.05)

City	**Mumbai**	**Chennai**	**Bengaluru**	**Hyderabad**
Parameter				
AOD	**-99 (***)**	**62 (***)**	3.95	-15.40
CF	6.81	115.32	**-59.41(*)**	-21.30
CTP	**0.29 (**)**	-0.16	**0.029(**)**	**0.33(***)**
CTT	-0.65	**2.53 (*)**	-0.04	**-2.70(***)**
K	0.13	**2.26 (***)**	0.18	**-0.74(**)**
Intercept	-81.50	-24.11	48.04	-139.25

The results showed that AOD was highly significant in predicting precipitation depths during an EPE for Mumbai and Chennai. Assuming that all other components in the regression equation are constant, Chennai receives more precipitation with an increase in AOD because the coefficient is positive, while Mumbai receives less precipitation because the coefficient is negative. This might be due to the location of the Chennai and Mumbai towards east and west coasts respectively. Also, the latitudinal influence might result in different behavior of precipitation. Additionally, the regression analysis for Chennai City showed that K and CTT were equally significant. Chennai's climate is nearly constant all year round because of its proximity to the thermal equator. Chennai's average elevation above sea level is 6.7 meters, making the city nearly flat. As a result, the vertical lapse rate for any EPE does not vary significantly, as seen by K-index map in Fig 6.11. This could be the cause of the positive and substantial coefficient of K-index in the regression equation for Chennai. CTP has a positive influence on precipitation and was found to be significant in all cities except Chennai. The behavior of cloud parameters was different in Mumbai and Chennai because of their location towards the west and east coast of peninsular India. The city of Mumbai is towards the windward side of the western ghat which receives precipitation from south-west monsoon from Arabian sea. The precipitation over the city is influenced by the maritime clouds. The variations in pressure at various city elevations when the monsoon arrives could potentially be a cause of an EPE (Chakravarty et al., 2021). The present study demonstrates that the coefficient of CTP for Mumbai was positive and significant, as indicated by Table 6.5.The cloud properties (CTP and CTT) and K-index were significant for the city of Hyderabad. Hyderabad's terrain is hilly, with elevations between 456 and 650 meters. Precipitation falls on the city due to low pressure in the Bay of Bengal and Arabian Sea. The city is situated in

the hilly area of the Deccan Plateau therefore, precipitation is enhanced by certain cloud characteristics.

6.7 Closure

The correlation of AOD and CF in various rainfall regimes reveal that widely scattered thunderstorm state influences the precipitation under favorable climate conditions. The analysis of factors causing EPE on metropolitan cities reveal that AOD has impact on coastal cities and cloud parameters have impact on other cities. The detailed summary and conclusions of the research work is presented in the next chapter.

CHAPTER 7
SUMMARY AND CONCLUSIONS

7.1 General

The research work was summarized in accordance with the stated objectives in this chapter. The conclusions reached after the analysis for each objective are described. Additionally, the limitations of the current research as well as the scope for further research of the work are also discussed.

7.2 Summary

This research aims to investigate how aerosols affect temperature and precipitation in the Indian peninsular region by using radiation diagnostics and atmospheric stability. Using R statistical software, the applicability of three different types of AOD data was examined in the current study in relation to field observations. In addition, all statistical metrics pertaining to every category of satellite data are computed to choose the most promising AOD data for additional examination. Furthermore, trend analysis was carried out using both the conventional Mann-Kendall test and the novel trend analysis approach based on decadal data. Generally, ITA is performed on gridded data. In the current study concentrates on application of ITA on raster data by suitable modification in ITA code using R statistical software was carried out. An analysis of the factors contributing to EPE in and around Peninsular India's urban cities is conducted.

The effect of atmospheric stability and AOD on the macrophysical properties of warm clouds in southern India is studied from 2005 to 2019. The effect of AOD on precipitation is also studied for cumulative 5-year, 10-year, and 15-year data for heterogenous rainfall regimes. The changes in cloud fraction for light, moderate and heavy rainfall regime is represented

using heat maps. The spatial distribution of AOD and CF in three rainfall regimes for cumulative 5-year, 10-year, and 15-year data is carried out.

This study explores the changes in mean temperature due to aerosols in peninsular India over three different time scales. The study calculates the ADRF using the proposed factored method and data from the MERRA-2 radiation diagnostics. The Mann-Kendall trend analysis was used to investigate the trend of ADRF over time, and it was found that ADRF increased from 2015 to 2019, with the highest increase observed in the tropical savanna and warm semi-arid climate regions. To examine the effect of AOD on temperature, the study analysed the variables for the period prior to lockdown, lockdown, and post-lockdown periods in 2020 and compared them to the average values from 2015 to 2019.

The present study also analysed the potential influence of aerosol, cloud, and atmospheric stability properties on the occurrence of EPEs. By arranging precipitation data from 2015 to 2021 in ascending order, the 95th percentile threshold value was determined. The precipitation data that exceeded the threshold value was considered as EPEs. The R Statistical Software was used to calculate the number of EPEs for the metropolitan areas of Bengaluru, Chennai, Hyderabad, and Mumbai between 2018 and 2020. The spread of AOD, cloud properties, and K-index for 10 days prior to the occurrence of EPEs. It was known that satellite AOD data might be contaminated with clouds during EPEs, so AOD greater than 1.5 was not considered in the analysis. Overall, the present research work examined the influence of AOD on cloud fraction and precipitation, radiative forcing and EPEs for the Southern Indian region.

7.3 Conclusions

The important findings drawn from the research work are as follows.

- Statistical analysis shows that MODIS Terra AOD data has highest coefficient of determination with less errors when compared to MERRA-2 and OMI data.
- Trend analysis on AOD data using Mann-Kendall test (MK test) show that there was positive trend in two decades but the spatial distribution of trend in second data was highly variant when compared to first decade.
- Trend analysis on raster data using Innovative Trend Analysis (ITA) method incorporates trend indicator which is equivalent to z- value in MK test. The results thus obtained conform to MK test and hence it can be concluded that ITA is also a preferable method for trend analysis on raster data.
- The analysis on effect of AOD on temperature was studied based on the distribution of ADRF. The results indicated that AOD, ADRF, and mean temperature decreased in

the pre-lockdown period, with the largest decline occurring in the tropical savanna region. This indicates that aerosols have a cooling effect on the atmosphere.

- However, the lockdown period has witnessed a decrease in AOD and mean temperature while ADRF increased in most of the study area. The increase in ADRF may be attributed to energy being trapped in the upper layers of the atmosphere. The same pattern was observed in the post-lockdown time scale.
- The analysis on AOD and CF for cumulative data periods has demonstrated a favourable correlation between them. For cumulative 10-year data, the correlation is smaller, while for cumulative 15-year data, it is stronger.
- The cumulative 10-year and 15-year data for isolated thunderstorm states show a substantial link between AOD and CF, even if there is a positive relationship for all atmospheric stability levels.
- Over a period of five years, a substantial correlation between AOD and CF was observed in the widely scattered thunderstorm state. Emissive aerosols might be the major cause for such result. Because emissive aerosols are present in clouds, solar energy is reflected off them rather being absorbed. In the research location, this impact results in increased cloud coverage and slowed cloud droplet evaporation.
- The distribution of AOD and CF in light rain is most visible in the tropical savanna region, followed by the warm semi-arid climate region, whereas in moderate rain, the tropical savanna climate region and the humid subtropical climate region were most visible.
- The lower AOD found a threefold increase in value when compared to the cumulative 5-year dataset in the heavy rain regime. The moderate AOD in heavy rain has increased by 84% and 44% for cumulative 10-year and 15-year datasets, respectively.
- Under heavy rain, there was also a noticeable increase in low and moderate CF for the entire study area. The increased production of sulphate and nitrate aerosols by certain industries may be the cause of the rise in AOD and CF. For the various rainfall regimes in peninsular India, the relationship between AOD and CF was established with respect to atmospheric stability.
- The spatial distribution indicated that AOD in the range of 0.2-0.6 influenced precipitation in Mumbai and Chennai. Furthermore, low-level clouds (CTP > 680 hPa) with isolated thunderstorm conditions (20°C < K < 25°C) and CTT > 0°C enhanced precipitation in Mumbai.
- Conversely, in Chennai, middle-level clouds (CTP < 680 hPa) with numerous thunderstorm conditions (K > 35°C) and CTT < 0°C intensified precipitation. This

difference might be attributed to the coastal and marine influences on the cities of Mumbai and Chennai.

- Middle-level clouds (CTP in the range of 440 hPa to 680 hPa), along with AOD less than 0.3, amplified precipitation in Hyderabad.
- A combination of middle-level clouds (CTP in the range of 440 hPa to 680 hPa), low AOD (<0.4), numerous thunderstorm conditions (K > 35°C), and CTT < 0°C led to intensified precipitation in all the observed EPEs. Low-level clouds (CTP > 680 hPa), AOD in the range of 0.4–0.6, isolated thunderstorm conditions (20°C < K < 25°C), and CTT > 0°C were other factors contributing to the occurrence of EPEs.
- The regression analysis indicated that the spread of AOD was significant for the coastal cities (Mumbai and Chennai). CTP was found to be significant for three out of four cities, while CTT and K were significant in two out of four cities.
- The environmental impact is on to address the mitigation measures to be taken for reducing the concentration of aerosols in the atmosphere. The social impact is to help in providing mitigation and preparedness of the individuals during the occurrence of EPEs.

7.4 Research Contributions

The following are the important research contributions from this study

- Validation of satellite AOD against the ground observations was performed and found that MODIS AOD is the suitable satellite product to perform further analysis.
- The aerosol-radiation interactions reveal that the aerosols heat up the atmosphere in most of the metropolitan cities and cool down towards the coastal regions.
- The results of this study provide important information on how aerosols affect temperature in peninsular India over a range of time periods. The study emphasizes necessity to comprehend the interaction between aerosols and other climate variables It helps us to understand the beginning of south-west monsoon and how local weather patterns work.
- The aerosol-cloud-precipitation interactions shows that the low AOD and widely scattered thunderstorm state can result in precipitation.
- The list of parameters that result in EPE varies for coastal and other metropolitan cities.

7.5 Limitations of the study

Although the research has covered major aspects of AOD affecting precipitation and temperature patterns in the study area, the following are the limitations in the research carried out.

- The current study has utilised the three properties of cloud namely cloud fraction, cloud top pressure and cloud top temperature. The cloud properties like Cloud Optical Depth, Cloud Effective Radius may be included in the study.
- The present research has utilised radiation diagnostics from MERRA-2. It can further be extended to use CERES data.
- The current study is limited to data between 2018-2020. The regression model may be strengthened by extending the duration for the identification of the EPEs. Also, the coarse resolution of the datasets may have impact on the results significantly.

7.6 Scope for Further Study

The research can further be extended to carry out the following works

- The type of aerosol that influences cloud formation and precipitation in a specific climatic region can be understood.
- Analysis of aerosol-cloud-precipitation interactions can help us to better understand and mitigate the impacts of climate change on the region.
- It may be possible to uncover additional reasons for the occurrence of EPEs by incorporating Precipitable Water Content (PWV) and cloud phase into the research to examine the formation of clouds with water content.

References

1. Ackerman, A.S., Toon, O.B., Stevens, D.E., Heymsfield, A.J., Ramanathan, V. and Welton, E.J., 2000. Reduction of tropical cloudiness by soot. Science, 288(5468), pp.1042-1047.
2. Adam, M.G., Tran, P.T. and Balasubramanian, R., 2021. Air quality changes in cities during the COVID-19 lockdown: A critical review. Atmospheric Research, 264, p.105823.
3. Alashan, S., 2018. An improved version of innovative trend analyses. Arab J Geosci 11 (3): 50.
4. Ali, R., Kuriqi, A., Abubaker, S. and Kisi, O., 2019. Long-term trends and seasonality detection of the observed flow in Yangtze River using Mann-Kendall and Sen's innovative trend method. Water, 11(9), p.1855.
5. Allen, S.K., Plattner, G.K., Nauels, A., Xia, Y. and Stocker, T.F., 2014, May. Climate Change 2013: The Physical Science Basis. An overview of the Working Group 1 contribution to the Fifth Assessment Report of the Intergovernmental Panel on Climate Change (IPCC). In EGU General Assembly Conference Abstracts (p. 3544).
6. Andreae, M.O., Rosenfeld, D., Artaxo, P., Costa, A.A., Frank, G.P., Longo, K.M. and Silva-Dias, M.A.F.D., 2004. Smoking rain clouds over the Amazon. science, 303(5662), pp.1337-1342.
7. Ångström, A., 1929. On the atmospheric transmission of sun radiation and on dust in the air. Geografiska Annaler, 11(2), pp.156-166.
8. Anil, S., Manikanta, V. and Pallakury, A.R., 2021. Unravelling the influence of subjectivity on ranking of CMIP6 based climate models: A case study. International Journal of Climatology, 41(13), 5998-6016.
9. Antuña-Marrero, J.C., Cachorro Revilla, V., García Parrado, F., de Frutos Baraja, Á., Rodríguez Vega, A., Mateos, D., Estevan Arredondo, R. and Toledano, C., 2018. Comparison of aerosol optical depth from satellite (MODIS), sun photometer and broadband pyrheliometer ground-based observations in Cuba. Atmospheric Measurement Techniques, 11(4), pp.2279-2293.
10. Babu, S. S., M. R. Manoj, K. K. Moorthy, M. M. Gogoi, V. S. Nair, S. K. Kompalli, S. K. Satheesh, 2013. "Trends in Aerosol Optical Depth over Indian Region: Potential Causes and Impact Indicators." Journal of Geophysical Research Atmospheres 118: 20.
11. Balakrishnaiah, G., Reddy, B.S.K., Gopal, K.R., Reddy, R.R., Reddy, L.S.S., Swamulu, C., Ahammed, Y.N., Narasimhulu, K., KrishnaMoorthy, K. and Babu, S.S., 2012. Spatio-temporal variations in aerosol optical and cloud parameters over Southern India retrieved from MODIS satellite data. Atmospheric environment, 47, 435-445.
12. Banerjee, S., and S. K. Ghosh. 2014. "Seasonal Trend of AOD and Angstrom Exponent (A) over Indian Megacities in Varying Spatial Resolution." Atmospheric and Oceanic Physics arXiv: 1403.7367v1.
13. Bellouin, N., Quaas, J., Gryspeerdt, E., Kinne, S., Stier, P., Watson-Parris, D., Boucher, O., Carslaw, K.S., Christensen, M., Daniau, A.L. and Dufresne, J.L., 2020. Bounding global aerosol radiative forcing of climate change. Reviews of Geophysics, 58(1), p.e2019RG000660.
14. Bhanu Kumar, O.S.R.U., Suneetha, P., Ramalingeswara, Rao S., Satya Kumar, M., 2012. Simulation of heavy rainfall events during retreat phase of summer monsoon season over parts of Andhra Pradesh. Int. J. Geosci. 3, 737–748. http://dx.doi.org/10.4236/ijg.2012.34074.

15. Bibi, H., Alam, K., Chishtie, F., Bibi, S., Shahid, I. and Blaschke, T., 2015. Intercomparison of MODIS, MISR, OMI, and CALIPSO aerosol optical depth retrievals for four locations on the Indo-Gangetic plains and validation against AERONET data. Atmospheric Environment, 111, pp.113-126.
16. Borbas, E., 2015. MODIS Atmosphere L2 Atmosphere Profile Product. NASA MODIS Adaptive Processing System, Goddard Space Flight Center, USA: http://dx.doi.org/10.5067/MODIS/MOD07_L2.061.
17. Budisulistiorini, S.H., Riva, M., Williams, M., Chen, J., Itoh, M., Surratt, J.D. and Kuwata, M., 2017. Light-absorbing brown carbon aerosol constituents from combustion of Indonesian peat and biomass. Environmental Science & Technology, 51(8), pp.4415-4423.
18. Caloiero, T., Coscarelli, R. and Ferrari, E., 2018. Application of the innovative trend analysis method for the trend analysis of rainfall anomalies in southern Italy. Water Resources Management, 32(15), pp.4971-4983.
19. Chakraborty, A., 2016. A synoptic-scale perspective of heavy rainfall over Chennai in November 2015. Curr. Sci. 111 (1), 201–207. http://dx.doi.org/10.18520/cs/v111/ i1/201-207.
20. Chakravarty, K., Bhangale, R., Das, S., Yadav, P., Kannan, B.A.M. and Pandithurai, G., 2021. Unraveling the characteristics of precipitation microphysics in summer and winter monsoon over Mumbai and Chennai–the two urban-coastal cities of Indian sub-continent. Atmospheric Research, 249, p.105313.
21. Che, H., Yang, L., Liu, C., Xia, X., Wang, Y., Wang, H., Wang, H., Lu, X. and Zhang, X., 2019. Long-term validation of MODIS C6 and C6. 1 Dark Target aerosol products over China using CARSNET and AERONET. Chemosphere, 236, p.124268.
22. Chen, S., Jiang, N., Huang, J., Xu, X., Zhang, H., Zang, Z., Huang, K., Xu, X., Wei, Y., Guan, X. and Zhang, X., 2018. Quantifying contributions of natural and anthropogenic dust emission from different climatic regions. Atmospheric Environment, 191, 94-104.
23. Choudhury, G., Tyagi, B., Krishna Vissa, N., Singh, J., Sarangi, C., Nand Tripathi, S., Tesche,M., 2020. Aerosol-enhanced high precipitation events near the Himalayan foothills. Atmos.Chem. Phys. 20, 15389–15399. https://doi.org/10.5194/acp-20-15389-2020.
24. Chung, E.S. and Soden, B.J., 2015. An assessment of direct radiative forcing, radiative adjustments, and radiative feedbacks in coupled ocean–atmosphere models. Journal of Climate, 28(10), pp.4152-4170.
25. Constantino, L. and Bréon, F.M., 2013. Aerosol indirect effect on warm clouds over South-East Atlantic, from co-located MODIS and CALIPSO observations. Atmospheric Chemistry and Physics, 13(1), 69-88.
26. Dagan, G., Koren, I. and Altaratz, O., 2015. Competition between core and periphery-based processes in warm convective clouds–from invigoration to suppression. Atmospheric Chemistry and Physics, 15(5), pp.2749-2760.
27. David, L.M., Ravishankara, A.R., Kodros, J.K., Venkataraman, C., Sadavarte, P., Pierce, J.R., Chaliyakunnel, S. and Millet, D.B., 2018. Aerosol optical depth over India. Journal of Geophysical Research: Atmospheres, 123(7), 3688-3703.
28. Deb, S.K., Kishtawal, C.M., Bongirwar, V.S., Pal, P.K., 2010. The simulation of heavy rainfall episode over Mumbai: impact of horizontal resolutions and cumulus parameterization schemes. Nat. Hazards 52, 117–142.
29. Dong, S., Sun, Y., Li, C., Zhang, X., Min, S.-K., Kim, Y.-H., 2021. Attribution of extreme precipitation with updated observations and CMIP6 simulations. J. Clim. 34 (3), 871–881. https://doi.org/10.1175/JCLI-D-19-1017.1.
30. Dumka, U.C., Saheb, S.D., Kaskaoutis, D.G., Kant, Y. and Mitra, D., 2016. Columnar aerosol characteristics and radiative forcing over the Doon Valley in the Shivalik range of

northwestern Himalayas. Environmental Science and Pollution Research, 23, pp.25467-25484.
31. Edenhofer, O. ed., 2015. Climate change 2014: mitigation of climate change (Vol. 3). Cambridge University Press.
32. Eirund, G.K., Drossaart van Dusseldorp, S., Brem, B.T., Dedekind, Z., Karrer, Y., Stoll, M. and Lohmann, U., 2022. Aerosol–cloud–precipitation interactions during a Saharan dust event–A summertime case-study from the Alps. Quarterly Journal of the Royal Meteorological Society, 148(743), pp.943-961.
33. Evans, J.S. and Ram, K., 2019. Package 'spatialEco'.
34. Fawole, O.G., Cai, X., Pinker, R.T. and MacKenzie, A.R., 2019. Analysis of radiative properties and direct radiative forcing estimates of dominant aerosol clusters over an urban-desert region in West Africa. Aerosol and Air Quality Research, 19(1), pp.38-48.
35. Fortelli, A., Scafetta, N., Mazzarella, A., 2019. Nowcasting and real-time monitoring of heavy rainfall events inducing flash-floods: an application to Phlegraean area (Central-Southern Italy). Nat. Hazards 97, 861–889. https://doi.org/10.1007/s11069-019-03680-7.GPM observations. Adv. Meteorol. 2019. https://doi.org/10.1155/2019/4631609.
36. Ghorbani, H., 2019. Mahalanobis distance and its application for detecting multivariate outliers. Facta Universitatis, Series: Mathematics and Informatics, 34(3), pp.583-595.
37. Gopal, K.R., Reddy, K.R.O., Balakrishnaiah, G., Arafath, S.M., Reddy, N.S.K., Rao, T.C., Reddy, T.L. and Reddy, R.R., 2016. Regional trends of aerosol optical depth and their impact on cloud properties over Southern India using MODIS data. Journal of Atmospheric and Solar-Terrestrial Physics, 146, 38-48.
38. Gouda, K.C., Gogeri, I. and ThippaReddy, A.S., 2022. Assessment of Aerosol Optical Depth over Indian Subcontinent during COVID-19 lockdown (March–May 2020). Environmental Monitoring and Assessment, 194(3), p.195.
39. Grandey, B.S., Stier, P. and Wagner, T.M., 2013. Investigating relationships between aerosol optical depth and CF using satellite, aerosol reanalysis and general circulation model data. Atmospheric Chemistry and Physics, 13(6), 3177-3184. https://ladsweb.modaps.eosdis.nasa.gov/
40. Gryspeerdt, E., Stier, P. and Partridge, D.G., 2014. Links between satellite-retrieved aerosol and precipitation. Atmospheric Chemistry and Physics, 14(18), pp.9677-9694.
41. Guhathakurta, P., Sreejith, O.P. and Menon, P.A., 2011. Impact of climate change on extreme rainfall events and flood risk in India. Journal of earth system science, 120, pp.359-373.
42. Gupta, G., Ratnam, M.V., Madhavan, B.L. and Narayanamurthy, C.S., 2022. Long-term trends in Aerosol Optical Depth obtained across the globe using multi-satellite measurements. Atmospheric Environment, 273, p.118953.
43. Guo, H., Kota, S.H., Chen, K., Sahu, S.K., Hu, J., Ying, Q., Wang, Y., Zhang, H., 2018a. Source contributions and potential reductions to health effects of particulate matter in India. Atmos. Chem. Phys. 18, 1e21. https://doi.org/10.5194/acp-18-15219-2018.
44. Guo, H., Sahu, S.K., Kota, S.H., Zhang, H., 2019. Characterization and health risks of criteria air pollutants in Delhi, 2017. Chemosphere 225, 27e34. https://doi.org/ 10.1016/j.chemosphere.2019.02.154.
45. Guo, J., Deng, M., Lee, S.S., Wang, F., Li, Z., Zhai, P., Liu, H., Lv, W., Yao, W. and Li, X., 2016. Delaying precipitation and lightning by air pollution over the Pearl River Delta. Part I: Observational analyses. Journal of Geophysical Research: Atmospheres, 121(11), pp.6472-6488.
46. Habib, G., Venkataraman, C., Chiapello, I., Ramachandran, S., Boucher, O., Shekar Reddy, M., 2006. Seasonal and interannual variability in absorbing aerosols over land. Atmos. Chem. Phys. 10, 10399e10420. https://doi.org/10.5194/acp-10- 10399-2010.

47. Holben, B., Eck, T., Slutsker, I., Tanre, D., Buis, J., Setzer, A., Vermote, E., Reagan, J.,Kaufman, Y., Nakajima, T., 1998. AERONETda federated instrument network and data archive for aerosol characterization. Remote Sens. Environ. 66, 1e16
48. Hu, Z., Jin, Q., Ma, Y., Pu, B., Ji, Z., Wang, Y. and Dong, W., 2021. Temporal evolution of aerosols and their extreme events in polluted Asian regions during Terra's 20-year observations. Remote Sensing of Environment, 263, p.112541.
49. Huffman, G., Bolvin, D., Braithwaite, D., Hsu, K., Joyce, R., Xie, P., 2014. Integrated Multi-satellite Retrievals for GPM (IMERG), version 4.4. NASA's Precipitation Processing Center. ftp://arthurhou.pps.eosdis.nasa.gov/gpmdata.
50. Jaksa, W.T., Sridhar, V., Huntington, J.L., and Khanal, M., 2013. Evaluation of the Complementary Relationship using Noah Land Surface Model and North American Regional Reanalysis (NARR) Data to Estimate Evapotranspiration in Semiarid Ecosystems, Journal of Hydrometeorology, Vol 14, Issue 1, 345-359, Feb 2013 doi: 10.1175/JHM-D-11-067.1.
51. Jasmine, M.K., Aloysius, M., Jayaprakash, R., Fathima, C.P., Prijith, S.S. and Mohan, M., 2022. Investigation on the role of aerosols on precipitation enhancement over Kerala during August 2018. Atmospheric Environment, 279, p.119101.
52. Jenamani, R.K., Bhan, S.C. and Kalsi, S.R., 2006. Observational/forecasting aspects of the meteorological event that caused a record highest rainfall in Mumbai. Current Science, pp.1344-1362.
53. Jethva, H., Satheesh, S., Srinivasan, J., 2007. Assessment of second generation MODIS aerosol retrieval (Collection 005) at Kanpur, India. Geophys. Res. Lett. 34.
54. Kahn, R.A., Nelson, D.L., Garay, M.J., Levy, R.C., Bull, M.A., Diner, D.J., Martonchik, J.V., Paradise, S.R., Hansen, E.G. and Remer, L.A., 2009. MISR aerosol product attributes and statistical comparisons with MODIS. IEEE Transactions on Geoscience and Remote Sensing, 47(12), pp.4095-4114.
55. Kant, S., Panda, J. and Gautam, R., 2019. A seasonal analysis of aerosol-cloud-radiation interaction over Indian region during 2000–2017. Atmospheric Environment, 201, 212-222.
56. Kant, S., Panda, J., Pani, S.K., Wang, P.K., 2018. Long-term study of aerosol–cloud–precipitation interaction over the eastern part of India using satellite observations during pre-monsoon season. Theor. Appl. Climatol. 1–22. https://doi.org/10.1007/s00704-018-2509-2.
57. Kaskaoutis, D.G., Badarinath, K.V.S., Kumar Kharol, S., Rani Sharma, A. and Kambezidis, H.D., 2009. Variations in the aerosol optical properties and types over the tropical urban site of Hyderabad, India. Journal of Geophysical Research: Atmospheres, 114(D22).
58. Kendall.M.G, Rank Correlation Methods, Griffin, London, UK, 1975.
59. Koren, I., Kaufman, Y.J., Rosenfeld, D., Remer, L.A. and Rudich, Y., 2005. Aerosol invigoration and restructuring of Atlantic convective clouds. Geophysical Research Letters, 32(14).
60. Koren, I., Remer, L.A., Altaratz, O., Martins, J.V. and Davidi, A., 2010. Aerosol-induced changes of convective cloud anvils produce strong climate warming. Atmospheric Chemistry and Physics, 10(10), 5001-5010.
61. Kottek, M., Grieser, J., Beck, C., Rudolf, B. and Rubel, F., 2006. World map of the Köppen-Geiger climate classification updated.
62. Kourtidis, K., Stathopoulos, S., Georgoulias, A.K., Alexandri, G. and Rapsomanikis, S., 2015. A study of the impact of synoptic weather conditions and water vapor on aerosol–cloud relationships over major urban clusters of China. Atmospheric Chemistry and Physics, 15(19), 10955-10964.
63. Kucienska, B., Raga, G.B. and Romero-Centeno, R., 2012. High lightning activity in maritime clouds near Mexico. Atmospheric Chemistry and Physics, 12(17), 8055-8072.

64. Kumar, A., 2013. Variability of aerosol optical depth and cloud parameters over North Eastern regions of India retrieved from MODIS satellite data. Journal of Atmospheric and Solar-Terrestrial Physics, 100, 34-49.
65. Kumar, A., 2020. Spatio-temporal variations in satellite based aerosol optical depths & aerosol index over Indian subcontinent: Impact of urbanization and climate change. Urban Climate, 32, 100598.
66. Kumar, K.R., Boiyo, R., Madina, A., Kang, N., 2018a. A 13-year climatological study on the variations of aerosol and cloud properties over Kazakhstan from remotely sensed satellite observations. J. Atmos. Sol. Terr. Phys. 179, 55–68. https://doi.org/10. 1016/j.jastp.2018.06.014.
67. Kumar, M., Parmar, K.S., Kumar, D.B., Mhawish, A., Broday, D.M., Mall, R.K. and Banerjee, T., 2018. Long-term aerosol climatology over Indo-Gangetic Plain: Trend, prediction and potential source fields. Atmospheric environment, 180, pp.37-50.
68. Kumar, S., Silva, Y., Moya-Alvarez, A.S. and Martínez-Castro, D., 2019. Seasonal and regional differences in extreme rainfall events and their contribution to the world's precipitation: GPM observations. Advances in Meteorology, 2019.
69. Lau, K. M., M. K. Kim, and K. M. Kim. 2006. "Asian Summer Monsoon Anomalies Induced by Aerosol Direct Forcing: The Role of the Tibetan Plateau." Climate Dynamics 26 (7–8): 855–864. doi:10.1007/s00382-006-0114-z.
70. Lau, W. K. M., and K.-M. Kim. 2010. "Fingerprinting the Impacts of Aerosols on Long Term Trends of the Indian Summer Monsoon Regional Rainfall." Geophysical Research Letters 37: L16705. doi:10.1029/2010GL043255
71. Levy, R.C., Remer, L.A., Kleidman, R.G., Mattoo, S., Ichoku, C., Kahn, R., Eck, T.F., 2010. Global evaluation of the Collection 5 MODIS dark-target aerosol products over India derived from TOMS: relationship to regional meteorology and emissions. Atmos. Environ. 40, 1909-1921.
72. Li, J. and Tartarini, F., 2020. Changes in air quality during the COVID-19 lockdown in Singapore and associations with human mobility trends. Aerosol and Air Quality Research, 20(8), pp.1748-1758.
73. Li, W., Jiang, Z., Zhang, X., Li, L., 2018. On the Emergence of anthropogenic signal in extreme precipitation change over China. Geophys. Res. Lett. 45 (17), 9179–9185. https://doi.org/10.1029/2018GL079133.
74. Li, Z., Guo, J., Ding, A., Liao, H., Liu, J., Sun, Y., Wang, T., Xue, H., Zhang, H. and Zhu, B., 2017. Aerosol and boundary-layer interactions and impact on air quality. National Science Review, 4(6), pp.810-833.
75. Li, S., Zhang, H., Wang, Z. and Chen, Y., 2023. Advances in the research on brown carbon aerosols: Its concentrations, radiative forcing, and effects on climate. Aerosol and Air Quality Research, 23(8), p.220336.
76. Liu, Q., Cheng, N., He, Q., Chen, Y., Liu, T., Liu, X., Zhang, H., Li, J. and Zhan, Q., 2020. Meteorological conditions and their effects on the relationship between aerosol optical depth and macro-physical properties of warm clouds over Shanghai based on MODIS. Atmospheric Pollution Research, 11(9), pp.1637-1644.
77. Liu, Q., Liu, X., Liu, T., Kang, Y., Chen, Y., Li, J. and Zhang, H., 2020. Seasonal variation in particle contribution and aerosol types in Shanghai based on satellite data from MODIS and CALIOP. Particuology, 51, 18-25.
78. Liu, S., Xing, J., Zhao, B., Wang, J., Wang, S., Zhang, X. and Ding, A., 2019. Understanding of aerosol–climate interactions in China: Aerosol impacts on solar radiation, temperature, cloud, and precipitation and its changes under future climate and emission scenarios. Current pollution reports, 5(2), pp.36-51.
79. Liu, Y., De Leeuw, G., Kerminen, V.M., Zhang, J., Zhou, P., Nie, W., Qi, X., Hong, J., Wang, Y., Ding, A. and Guo, H., 2017. Analysis of aerosol effects on warm clouds over

the Yangtze River Delta from multi-sensor satellite observations. Atmospheric Chemistry and Physics, 17(9), 5623-5641.
80. Liu, Y., Zhang, J., Zhou, P., Lin, T., Hong, J., Shi, L., Yao, F., Wu, J., Guo, H. and de Leeuw, G., 2018. Satellite-based estimate of the variability of warm cloud properties associated with aerosol and meteorological conditions. Atmospheric Chemistry and Physics, 18(24), 18187-18202.
81. Liu, Z., Yim, S.H., Wang, C. and Lau, N.C., 2018. The impact of the aerosol direct radiative forcing on deep convection and air quality in the Pearl River Delta region. Geophysical research letters, 45(9), pp.4410-4418.
82. López-Romero, J.M., Montávez, J.P., Jerez, S., Lorente-Plazas, R., Palacios-Peña, L. and Jiménez-Guerrero, P., 2021. Precipitation response to aerosol–radiation and aerosol–cloud interactions in regional climate simulations over Europe. Atmospheric Chemistry and Physics, 21(1), pp.415-430.
83. Maghrabi, A.H. and Alotaibi, R.N., 2018. Long-term variations of AOD from an AERONET station in the central Arabian Peninsula. Theoretical and Applied Climatology, 134(3-4), pp.1015-1026.
84. Mann, H.B., 1945. Nonparametric tests against trend. Econometrica: Journal of the econometric society, pp.245-259.
85. Manoj, M.R., Satheesh, S.K., Moorthy, K.K., Gogoi, M.M. and Babu, S.S., 2019. Decreasing trend in black carbon aerosols over the Indian region. Geophysical Research Letters, 46(5), pp.2903-2910.
86. Mao, J., Ping, F., Yin, L., Qiu, X., 2018. A Study of Cloud Microphysical Processes Associated With Torrential Rainfall Event Over Beijing. J. Geophys. Res. Atmos. 123, 8768–8791.https://doi.org/10.1029/2018JD028490.
87. Mao, Q. and Wan, H., 2022. Study on the Characteristics of Aerosol Radiative Forcing under Complex Pollution Conditions in Beijing. Atmosphere, 13(3), p.501.
88. McPhetres, A. and Aggarwal, S., 2018. An evaluation of MODIS-retrieved aerosol optical depth over AERONET sites in Alaska. Remote Sensing, 10(9), p.1384.
89. Menon, H.B., Shirodkar, S., Kedia, S., Ramachandran, S., Babu, S. and Moorthy, K.K., 2014. Temporal variation of aerosol optical depth and associated shortwave radiative forcing over a coastal site along the west coast of India. Science of the total environment, 468, pp.83-92.
90. Metz, B., Davidson, O., Swart, R. and Pan, J. eds., 2001. Climate change 2001: mitigation: contribution of Working Group III to the third assessment report of the Intergovernmental Panel on Climate Change (Vol. 3). Cambridge University Press.
91. Mhawish, Alaa, Tirthankar Banerjee, David M. Broday, Amit Misra, and Sachchida N. Tripathi. 2017. “Evaluation of MODIS Collection 6 Aerosol Retrieval Algorithms over Indo-Gangetic Plain: Implications of Aerosols Types and Mass Loading.” Remote Sensing of Environment 201:297–313.
92. Mishra, A.K., 2019. Quantifying the impact of global warming on precipitation patterns in India. Meteorological Applications, 26(1), 153-160.
93. Misumi, R., Uji, Y., Miura, K., Mori, T., Tobo, Y. and Iwamoto, Y., 2022. Classification of aerosol-cloud interaction regimes over Tokyo. Atmospheric Research, 272, 106150.
94. Mohammad, L., Mondal, I., Bandyopadhyay, J., Pham, Q.B., Nguyen, X.C., Dinh, C.D. and Al-Quraishi, A.M.F., 2022. Assessment of spatio-temporal trends of satellite-based aerosol optical depth using Mann–Kendall test and Sen’s slope estimator model. Geomatics, Natural Hazards and Risk, 13(1), pp.1270-1298.
95. More, S., Kumar, P.P., Gupta, P., Devara, P.C.S. and Aher, G.R., 2013. Comparison of aerosol products retrieved from AERONET, MICROTOPS and MODIS over a tropical urban city, Pune, India. Aerosol and air quality research, 13(1), pp.107-121.

96. Navinya, C., Patidar, G. and Phuleria, H.C., 2020. Examining effects of the COVID-19 national lockdown on ambient air quality across urban India. Aerosol and Air Quality Research, 20(8), pp.1759-1771.
97. Niyogi, D., Chang, H.I., Chen, F., Gu, L., Kumar, A., Menon, S. and Pielke, R.A., 2007. Potential impacts of aerosol–land–atmosphere interactions on the Indian monsoonal rainfall characteristics. Natural Hazards, 42(2), pp.345-359.
98. Öztopal, A. and Şen, Z., 2017. Innovative trend methodology applications to precipitation records in Turkey. Water resources management, 31, pp.727-737.
99. Pandey, S.K., Vinoj, V. and Panwar, A., 2020. The short-term variability of aerosols and their impact on cloud properties and radiative effect over the Indo-Gangetic Plain. Atmospheric Pollution Research, 11(3), pp.630-638.
100. Patakamuri, S.K. and Das, B., 2019. Package 'trendchange'. Cran, R-project.
101. Paulot, F., Paynter, D., Ginoux, P., Naik, V. and Horowitz, L.W., 2018. Changes in the aerosol direct radiative forcing from 2001 to 2015: observational constraints and regional mechanisms. Atmospheric Chemistry and Physics, 18(17), pp.13265-13281.
102. Penna, B., Herdies, D. and Costa, S., 2018. Estimates of direct radiative forcing due to aerosols from the MERRA-2 reanalysis over the Amazon region. Atmospheric Chemistry and Physics Discussions, pp.1-17.
103. Pinsky, M., Mazin, I.P., Korolev, A. and Khain, A., 2013. Supersaturation and diffusional droplet growth in liquid clouds. Journal of the Atmospheric Sciences, 70(9), pp.2778-2793.
104. Platnick, S., King, M.D., Meyer, K.G., Wind, G.A.L.A., Amarasinghe, N.A.N.D.A.N.A., Marchant, B.E.N.J.A.M.I.N., Arnold, G.T., Zhang, Z.H.I.B.O., Hubanks, P.A., Ridgway, B.I.L.L. and Riedi, J., 2015. MODIS cloud optical properties: User guide for the Collection 6 Level-2 MOD06/MYD06 product and associated Level-3 Datasets. Version, 1, p.145.
105. Quan, J., Tie, X., Zhang, Q., Liu, Q., Li, X., Gao, Y. and Zhao, D., 2014. Characteristics of heavy aerosol pollution during the 2012–2013 winter in Beijing, China. Atmospheric Environment, 88, 83-89.
106. Rajesh, T.A. and Ramachandran, S., 2019. Spatial, seasonal, and altitudinal heterogeneity in single scattering albedo of aerosols over an urban and a remote site: Radiative implications. Atmospheric environment, 218, p.116954.
107. Ramachandran, S., and R. Cherian. 2008. "Regional and Seasonal Variations in Aerosol Optical Characteristics and Their Frequency Distributions over India during 2001–2005." Journal of Geophysical Research 113: D08207. doi:10.1029/2007JD008560
108. Ramanathan, V., Chung, C., Kim, D., Bettge, T., Buja, L., Kiehl, J.T., Washington, W.M., Fu, Q., Sikka, D.R. and Wild, M., 2005. Atmospheric brown clouds: Impacts on South Asian climate and hydrological cycle. Proceedings of the National Academy of Sciences, 102(15), pp.5326-5333.
109. Ramanathan, V.C.P.J., Crutzen, P.J., Kiehl, J.T. and Rosenfeld, D., 2001. Aerosols, climate, and the hydrological cycle. science, 294(5549), 2119-2124.
110. Rana, A., Jia, S. and Sarkar, S., 2019. Black carbon aerosol in India: A comprehensive review of current status and future prospects. Atmospheric Research, 218, pp.207-230.
111. Rani, S. and Kumar, R., 2022. Spatial distribution of aerosol optical depth over India during COVID-19 lockdown phase-1. Spatial Information Research, 30(3), pp.417-426.
112. Rastogi, N., Singh, A., Sarin, M.M. and Singh, D., 2016. Temporal variability of primary and secondary aerosols over northern India: Impact of biomass burning emissions. Atmospheric environment, 125, pp.396-403.
113. Remer, L.A., Kaufman, Y.J., Levin, Z. and Ghan, S., 2002. Model assessment of the ability of MODIS to measure top-of-atmosphere direct radiative forcing from smoke aerosols. Journal of the atmospheric sciences, 59(3), 657-667.

114. Remer, L.A., Kaufman, Y.J., Tanré, D., Mattoo, S., Chu, D.A., Martins, J.V., Li, R.R., Ichoku, C., Levy, R.C., Kleidman, R.G. and Eck, T.F., 2005. The MODIS aerosol algorithm, products, and validation. Journal of the atmospheric sciences, 62(4), pp.947-973.
115. Richa Pinto, Five extremely heavy rainy days in Monsoon 2019, eight in past decade, The Times of India, Mumbai, 29 Sept 2019
116. Rienecker and Coauthors, 2011: MERRA - NASA's Modern-Era Retrospective Analysis for Research and Applications. J. Climate, 24, 3624-3648, doi:10.1175/JCLI-D-11-00015.1.
117. Rosenfeld, D. and Woodley, W.L., 2000. Deep convective clouds with sustained supercooled liquid water down to-37.5 C. Nature, 405(6785), pp.440-442.
118. Rosenfeld, D., 1999. TRMM observed first direct evidence of smoke from forest fires inhibiting rainfall. Geophysical research letters, 26(20), pp.3105-3108.
119. Rosenfeld, D., 2006. Aerosols, clouds, and climate. Science, 312(5778), 1323-1324.
120. Rosenfeld, D., 2018. Cloud-Aerosol-Precipitation Interactions Based of Satellite Retrieved Vertical Profiles of Cloud Microstructure, in: Remote Sensing of Aerosols, Clouds, and Precipitation. Elsevier, pp. 129–152. https://doi.org/10.1016/B978-0-12-810437-8.00006-2.
121. Rosenfeld, D., Lohmann, U., Raga, G.B., O'Dowd, C.D., Kulmala, M., Fuzzi, S., Reissell, A. and Andreae, M.O., 2008. Flood or drought: how do aerosols affect precipitation?. science, 321(5894), 1309-1313.
122. Roxy, M.K., Ghosh, S., Pathak, A., Athulya, R., Mujumdar, M., Murtugudde, R., Terray, P. and Rajeevan, M., 2017. A threefold rise in widespread extreme rain events over central India. Nature communications, 8(1), p.708.
123. Rutan, D.A., Kato, S., Doelling, D.R., Rose, F.G., Nguyen, L.T., Caldwell, T.E. and Loeb, N.G., 2015. CERES synoptic product: Methodology and validation of surface radiant flux. Journal of Atmospheric and Oceanic Technology, 32(6), pp.1121-1143.
124. Saheb, S.D., Kant, Y. and Mitra, D., 2016, May. Variability of aerosol optical depth and aerosol radiative forcing over Northwest Himalayan region. In Remote Sensing of the Atmosphere, Clouds, and Precipitation VI (Vol. 9876, p. 98762M). International Society for Optics and Photonics.
125. Sahu, L.K., Sheel, V., Pandey, K., Yadav, R., Saxena, P. and Gunthe, S., 2015. Regional biomass burning trends in India: Analysis of satellite fire data. Journal of Earth System Science, 124, pp.1377-1387.
126. Sanikhani, H., Kisi, O., Mirabbasi, R. and Meshram, S.G., 2018. Trend analysis of rainfall pattern over the Central India during 1901–2010. Arabian Journal of Geosciences, 11, pp.1-14.
127. Sarangi, C., Tripathi, S.N., Kanawade, V.P., Koren, I. and Pai, D.S., 2017. Investigation of the aerosol–cloud–rainfall association over the Indian summer monsoon region. Atmospheric Chemistry and Physics, 17(8), pp.5185-5204.
128. Sarangi, C., Tripathi, S.N., Mishra, A.K., Goel, A. and Welton, E.J., 2016. Elevated aerosol layers and their radiative impact over Kanpur during monsoon onset period. Journal of Geophysical Research: Atmospheres, 121(13), pp.7936-7957.
129. Sarkar, S., Chokngamwong, R., Cervone, G., Singh, R.P. and Kafatos, M., 2006. Variability of aerosol optical depth and aerosol forcing over India. Advances in Space Research, 37(12), pp.2153-2159.
130. Satheesh, S.K., 2002, December. Letter to the Editor Aerosol radiative forcing over land: effect of surface and cloud reflection. In Annales Geophysicae (Vol. 20, No. 12, pp. 2105-2109). Göttingen, Germany: Copernicus Publications.
131. Seiki, T. and Nakajima, T., 2014. Aerosol effects of the condensation process on a convective cloud simulation. Journal of the Atmospheric Sciences, 71(2), pp.833-853.

132. Şen, Z., 2012. Innovative trend analysis methodology. Journal of Hydrologic Engineering, 17(9), pp.1042-1046.
133. Setti, S., Maheswaran, R., Radha, D., Sridhar, V., Barik, K.K., Narasimham, M.L., 2020. Attribution of hydrologic changes in a tropical river basin to climate and land use change: A case study from India, ASCE Journal of Hydrologic Engineering, 258, doi: 10.1061/(ASCE)HE.1943-5584.0001937.
134. Shaik, D.S., Kant, Y., Mitra, D., Chandola, H.C. and Suresh Babu, S., 2018. Long-term variability of MODIS 3 km aerosol optical depth over Indian region. ISPRS Annals of the Photogrammetry, Remote Sensing and Spatial Information Sciences, 4, pp.359-366.
135. Shukla, B.P., Kishtawal, C.M. and Pal, P.K., 2017. Satellite-based nowcasting of extreme rainfall events over Western Himalayan region. IEEE Journal of Selected Topics in Applied Earth Observations and Remote Sensing, 10(5), pp.1681-1686.
136. Singh, R., Dey, S., Tripathi, S., Tare, V., Holben, B., 2004. Variability of aerosol parameters over Kanpur, northern India. J. Geophys. Res. Atmos. (1984-2012) 109.
137. Singh, R.P. and Chauhan, A., 2020. Impact of lockdown on air quality in India during COVID-19 pandemic. Air Quality, Atmosphere & Health, 13(8), pp.921-928.
138. Small, J.D., Jiang, J.H., Su, H. and Zhai, C., 2011. Relationship between aerosol and cloud fraction over Australia. Geophysical Research Letters, 38(23).
139. Soni, A.R. and Chandel, M.K., 2020. Impact of rainfall on travel time and fuel usage for Greater Mumbai city. Transportation Research Procedia, 48, 2096-2107.
140. Sridhar, V. and Elliott, R.L., 2002. On the development of a simple downwelling longwave radiation scheme. Agricultural and Forest Meteorology, 112(3-4), pp.237-243.
141. Sridhar, V., 2013. Tracking the influence of irrigation on land surface fluxes and boundary layer climatology, Journal of Contemporary Water Research & Education, 152, 79-93.doi: 10.1111/j.1936-704X.2013.03170.x
142. Sridhar, V., 2013. Tracking the influence of irrigation on land surface fluxes and boundary layer climatology, Journal of Contemporary Water Research & Education, 152, 79-93.doi: 10.1111/j.1936-704X.2013.03170.x
143. Sridhar, V., Anderson, K.A., 2017. Human-induced modifications to boundary layer fluxes and their water management implications in a changing climate, Agricultural and Forest Meteorology, 234, 66-79, doi:10.1016/j.agrformet.2016.12.009
144. Sridhar, V., Anderson,, K.A., 2017. Human-induced modifications to boundary layer fluxes and their water management implications in a changing climate, Agricultural and Forest Meteorology, 234, 66-79, doi:10.1016/j.agrformet.2016.12.009
145. Sridhar, V., Billah, M., Valayamkunnath, P., 2018. Field- scale intercomparison analysis of ecosystems in partitioning surface energy balance components in a semi-arid environment, Ecohydrology and Hydrobiology, 187, doi:10.1016/j.ecohyd.2018.06.005
146. Sridhar, V., Jin, X., Jaksa, W.T., 2013. Explaining the hydroclimatic variability and change in the Salmon River basin, Climate Dynamics, 40, 1921-1937, doi: 10.1007/s00382-012-1467-0
147. Sridhar, V., Modi, P., Billah, M.M., Valayamkunnath, P., Goodall, J., 2019. Precipitation Extremes and Flood Frequency in a Changing Climate in Southeastern Virginia, Journal of American Water Resources Association, 55 (4), 1–20, 780-799, doi: 10.1111/1752-1688.12752
148. Srinivas, C.V., Yesubabu, V., Hari Prasad, D., Hari Prasad, K.B.R.R., Greeshma, M.M.,Baskaran, R., Venkatraman, B., 2018. Simulation of an extreme heavy rainfall event over Chennai, India using WRF: Sensitivity to grid resolution and boundary layer physics. Atmos. Res. 210, 66–82. https://doi.org/10.1016/j.atmosres.2018.04.014.
149. Srivastava, A. and Saran, S., 2017. Comprehensive study on AOD trends over the Indian subcontinent: a statistical approach. International Journal of Remote Sensing, 38(18), pp.5127-5149.

150. Srivastava, A.K., Bhoyar, P.D., Kanawade, V.P., Devara, P.C., Thomas, A. and Soni, V.K., 2021. Improved air quality during COVID-19 at an urban megacity over the Indo-Gangetic Basin: from stringent to relaxed lockdown phases. Urban Climate, 36, p.100791.
151. Srivastava, A.K., Rajeevan, M. and Kshirsagar, S.R., 2009. Development of a high resolution daily gridded temperature data set (1969–2005) for the Indian region. Atmospheric Science Letters, 10(4), pp.249-254.
152. Srivastava, R., 2017. Trends in aerosol optical properties over South Asia. International Journal of Climatology, 37(1), pp.371-380.
153. Subba, T., Gogoi, M.M., Pathak, B., Bhuyan, P.K. and Babu, S.S., 2020. Recent trend in the global distribution of aerosol direct radiative forcing from satellite measurements. Atmospheric Science Letters, 21(11), p.e975.
154. Sujatha, E.R., Sridhar, V., 2017. Mapping Debris Flow Susceptibility using Analytical Network Process, Journal of Earth System Science, 126: 116. doi:10.1007/s12040-017-0899-7
155. Sujatha, E.R., Sridhar, V., 2021. Landslide Susceptibility Analysis in the Era of Climate Change: A Logistic Regression Model Case Study in Coonoor, India, Hydrology, 8(1), 41, doi: 10.3390/hydrology8010041
156. Takahashi, H.G., Watanabe, S., Nakata, M. and Takemura, T., 2018. Response of the atmospheric hydrological cycle over the tropical Asian monsoon regions to anthropogenic aerosols and its seasonality. Progress in Earth and Planetary Science, 5(1), 1-14.
157. Tao, W.K., Chen, J.P., Li, Z., Wang, C. and Zhang, C., 2012. Impact of aerosols on convective clouds and precipitation. Reviews of Geophysics, 50(2).
158. Tao, W.K., Li, X., Khain, A., Matsui, T., Lang, S. and Simpson, J., 2007. Role of atmospheric aerosol concentration on deep convective precipitation: Cloud-resolving model simulations. Journal of Geophysical Research: Atmospheres, 112(D24).
159. Thomas, A., Kanawade, V.P., Sarangi, C. and Srivastava, A.K., 2021. Effect of COVID-19 shutdown on aerosol direct radiative forcing over the Indo-Gangetic Plain outflow region of the Bay of Bengal. Science of the Total Environment, 782, p.146918.
160. Thomas, G., Thomas, J., Mathew, A.V., Devika, R.S., Krishnan, A. and Nair, A.J., 2022. Non-uniform effect of COVID-19 lockdown on the air quality in different local climate zones of the urban region of Kochi, India. Spatial Information Research, pp.1-11.
161. Tobías, A., Carnerero, C., Reche, C., Massagué, J., Via, M., Minguillón, M.C., Alastuey, A. and Querol, X., 2020. Changes in air quality during the lockdown in Barcelona (Spain) one month into the SARS-CoV-2 epidemic. Science of the total environment, 726, p.138540.
162. Tripathi, S.N., Dey, S., Chandel, A., Srivastava, S., Singh, R.P. and Holben, B.N., 2005, June. Comparison of MODIS and AERONET derived aerosol optical depth over the Ganga Basin, India. In Annales Geophysicae (Vol. 23, No. 4, pp. 1093-1101). Göttingen, Germany: Copernicus Publications.
163. Twomey, S., 1977. The influence of pollution on the shortwave albedo of clouds. J. atmos. Sci, 34, 1149-1152.
164. Valayamkunnath, P., Sridhar, V., Zhao, W., Allen, R.G., Germino, M.J., 2018. Intercomparison of surface energy fluxes, soil moisture, and evapotranspiration from eddy covariance, large aperture scintillometer, and modeling across three ecosystems in a semiarid climate, Agricultural and Forest Meteorology, 248, 22-47, doi: 10.1016/j.agrformet.2017.08.025
165. Varpe, S.R., Mahajan, C.M., Kolhe, A.R., Kutal, G.C., Budhavant, K.B., Singh, P.R. and Aher, G.R., 2022. Aerosol–cloud interaction over south-central India and adjoining coastal areas. Aerosol Science and Engineering, 6(1), pp.45-60.

166. Vijayakumar, K., Devara, P.C.S., Giles, D.M., Holben, B.N., Rao, S.V.B. and Jayasankar, C.K., 2018. Validation of satellite and model aerosol optical depth and precipitable water vapour observations with AERONET data over Pune, India. International journal of remote sensing, 39(21), pp.7643-7663.
167. Vijayakumar, K., Devara, P.C.S., Giles, D.M., Holben, B.N., Rao, S.V.B. and Jayasankar, C.K., 2018. Validation of satellite and model aerosol optical depth and precipitable water vapour observations with AERONET data over Pune, India. International Journal of Remote Sensing, 39(21), 7643-7663.
168. Wang, F., Guo, J., Zhang, J., Huang, J., Min, M., Chen, T., Liu, H., Deng, M. and Li, X., 2015. Multi-sensor quantification of aerosol-induced variability in warm clouds over eastern China. Atmospheric Environment, 113, 1-9.
169. Wang, K., Sun, X., Zhou, Y., Zhang, C., 2017. Validation of MODIS-Aqua aerosol products C051 and C006 over the Beijing-Tianjin-Hebei region. Atmosphere 8, 172. https://doi.org/10.3390/atmos8090172.
170. Wang, R., Zhu, Y., Qiao, F., Liang, X.Z., Zhang, H. and Ding, Y., 2021. High-resolution Simulation of an Extreme Heavy Rainfall Event in Shanghai Using the Weather Research and Forecasting Model: Sensitivity to Planetary Boundary Layer Parameterization. Advances in Atmospheric Sciences, 38, pp.98-115.
171. Wang, Z., Xue, L., Liu, J., Ding, K., Lou, S., Ding, A., Wang, J. and Huang, X., 2022. Roles of atmospheric aerosols in extreme meteorological events: A systematic review. Current Pollution Reports, 8(2), pp.177-188.
172. Woodward, A., Smith, K.R., Campbell-Lendrum, D., Chadee, D.D., Honda, Y., Liu, Q., Olwoch, J., Revich, B., Sauerborn, R., Chafe, Z. and Confalonieri, U., 2013. Climate change and health: on the latest IPCC report. The Lancet, 383(9924), pp.1185-1189.
173. Xie, J. and Xia, X., 2008. Long-term trend in aerosol optical depth from 1980 to 2001 in North China. Particuology, 6(2), pp.106-111.
174. Yang, Y., Wang, H., Smith, S.J., Zhang, R., Lou, S., Yu, H., Li, C. and Rasch, P.J., 2018. Source apportionments of aerosols and their direct radiative forcing and long-term trends over continental United States. Earth's Future, 6(6), pp.793-808.
175. Yousefi, R., Wang, F., Ge, Q., Shaheen, A. and Kaskaoutis, D.G., 2023. Analysis of the winter AOD trends over Iran from 2000 to 2020 and associated meteorological effects. Remote Sensing, 15(4), p.905.
176. Yu, H., Kaufman, Y.J., Chin, M., Feingold, G., Remer, L.A., Anderson, T.L., Balkanski, Y., Bellouin, N., Boucher, O., Christopher, S. and DeCola, P., 2006. A review of measurement-based assessments of the aerosol direct radiative effect and forcing. Atmospheric Chemistry and Physics, 6(3), pp.613-666.
177. Zalakeviciute, R., Vasquez, R., Bayas, D., Buenano, A., Mejia, D., Zegarra, R., Diaz, V. and Lamb, B., 2020. Drastic improvements in air quality in Ecuador during the COVID-19 outbreak. Aerosol and Air Quality Research, 20(8), pp.1783-1792.
178. Zhang, J., Christopher, S.A., Remer, L.A. and Kaufman, Y.J., 2005. Shortwave aerosol radiative forcing over cloud-free oceans from Terra: 2. Seasonal and global distributions. Journal of Geophysical Research: Atmospheres, 110(D10).
179. Zhang, X., Cai, C., Hu, X.M., Gao, L., Xu, X., Hu, J. and Chen, H., 2022. Aerosols consistently suppress the convective boundary layer development. Atmospheric Research, 269, p.106032.

List of Publications

Journals

1. Kotrike, T., Pratap, D. & Keesara, V.R. Validation and Trend Analysis of Satellite-Based AOD Data over Southern India. *Aerosol Sci Eng* (2021). https://doi.org/10.1007/s41810-020-00082-2. (ESCI, SCOPUS) (IF:1.5)
2. Tharani Kotrike, Venkata Reddy Keesara, Venkataramana Sridhar, Analysis of the causes of extreme precipitation in major cities of Peninsular India using remotely sensed data, Remote Sensing Applications: Society and Environment, 2023, 101082, https://doi.org/10.1016/j.rsase.2023.101082. (ESCI, SCOPUS) (IF:4.7).
3. Tharani Kotrike, Venkata Reddy Keesara, Venkataramana Sridhar,'Illustration of relation between AOD and CF Over Southern India for Different Rainfall Regions', Atmospheric Environment (Under review) (SCOPUS) (IF: 4.6)
4. Tharani Kotrike, Venkata Reddy Keesara, Venkataramana Sridhar 'Comparative Analysis of Aerosol Direct Radiative Forcing During COVID-19 Lockdown Period in Peninsular India', Journal of the Indian Society of Remote Sensing. (Under review) (SCIE, SCOPUS) (IF:2.1).

Conferences

1. Kotrike, T., Pratap, D. & Keesara, V.R., Abhilash, Estimation of Aerosol Direct Radiative Forcing in Southern India in International Conference on Developments and Applications of Geomatics in Sep 2022.

Appendix A

A.1 R Code for Validation of Satellite and Model Re-Analysis AOD Data with Ground Observations

```
library(rgdal)
library(sp)
library(raster)
library(maptools)
library(mapdata)
library(maps)
library(stringr)
library(dplyr)
library(readxl)
library(ggplot2)
library(ggpmisc)
library(ggpubr)
library(tidyverse)
library(ncdf4)
library(outliers)
library(OutlierDC)
library(OutlierDM)
library(OutlierDetection)
library(OutliersO3)
library(naniar)
setwd("D:/OMI_d_kanpur")
files <- list.files()
length(files)
for ( i in 1:length(files)){
        <- nc_open( files[i], write=FALSE, readunlim=TRUE, verbose=FALSE,
                auto_GMT=TRUE, suppress_dimvals=FALSE )
tmp <- paste(firststring = (str_sub(files[i], 22,25)) , secondstring = (str_sub(files[1], 27,30)))
x <- as.Date(tmp,format="%Y%m%d")
```

```
n <- ncvar_get(o,"FinalAerosolOpticalDepth500")
j <- mean(n,na.rm=TRUE)
l <- as.numeric(j)
if (!is.na(l)){
write.table(data.frame(x,j),file="data.csv",append=TRUE,na="",sep=',',col.names=FALSE)
}
nc_close(o)
}
f<-read.csv("data.csv", stringsAsFactors=FALSE)
colnames(f) <- c("Num","Date","AOD")
k<- read.csv("D:/OMI_AERONET/kanpur_500.csv")
m <- length(count.fields("data.csv"))
n <- length(count.fields("D:/OMI_AERONET/kanpur_500.csv"))
if (m>n) {o<-m}else{o<-n}
for(i in 1:o){
h <- match(f[i,2],k[,2])
if (!is.na(h)){
r <- k[h,3]
write.table(data.frame(f[i,3],k[h,3]),file="new.csv",append=TRUE,na="",sep=',',col.names=FALSE)
}
}
l <- read.csv("D:/OMI_d_kanpur/new.csv")
colnames(l) <- c("Num","AOD_OMI","AOD_AERONET")
m <- lm(l$AOD_OMI~l$AOD_AERONET,data=l)
n <- summary(m)$adj.r.squared
if (n<0.5){
repeat{
        x <- l$AOD_OMI
        y <- l$AOD_AERONET
        z <- data.frame(x,y)
        k <- na.omit(z)
```

```
        w <- maha(k)
        p <- data.frame(w$`Location of Outlier`)
        for (i in 1:length(p[,1])){
        y <- p[i,]
        l[y,] = NA
        }
        a <- na.omit(l)
        q <- data.frame(a)
        a <- lm(l$AOD_OMI~l$AOD_AERONET,data=q,na.rm=TRUE)
        n <- summary(a)$adj.r.squared
        print(n)
        if (n >= 0.49){
        break
        }
}
}
my.formula <- y~x
ggplot(l, aes(AOD_OMI,AOD_AERONET)) + geom_smooth(method = "lm", se=FALSE, color="black", formula = my.formula) +
        stat_poly_eq(formula = my.formula,
                aes(label = paste(..eq.label.., ..rr.label.., sep = "--")),
                parse = TRUE) +
        geom_point()+stat_cor(mapping = aes(AOD_OMI,AOD_AERONET), data = NULL, method = "pearson",label.sep = ", ",
                        label.x.npc = "left", label.y.npc = "top",
                        label.x = 0.02, label.y = 1.7, output.type = "expression" )
```

A.2 R code for Trend analysis using MK test

```
library(raster)
library(sp)
library(spatialEco)
setwd("D:/trend")
files <- list.files()
```

```
a <- stack(files)
result<-raster.kendall(a, tau = TRUE, intercept = TRUE,  p.value = TRUE,
                       z.value = TRUE, confidence = TRUE)
names(result) <- c("slope","intercept", "p.value","z.value","tau")
slope <- raster(result[1])
tau <- raster(result[7])
intercept <- raster(result[2])
p.value <- raster(result$p.value)
z.value <- raster(result[4])
writeRaster(result,file.path="D:/trend/",filename="Trend_rainfall.tif",filetype="GTiff",overwrite=TRUE)
plot(result)
m = c(-1, 0.05, 1, 0.05, 4, 0)
rclmat = matrix(m, ncol=3, byrow=TRUE)
p.mask = reclassify(result$p.value, rclmat)
fun=function(x) { x[x<1] <- NA; return(x)}
p.mask.NA = calc(p.mask, fun)
trend.sig = mask(result$slope, p.mask.NA)
plot(trend.sig)
writeRaster(trend.sig,filename="mk_sec.tif",filetype="GTiff",overwrite=TRUE)
```

A.3 R code for Trend Analysis using ITA

```
library(readxl)
library(trend)
library(modifiedmk)
library(trendchange)
library(ggplot2)
library(basicTrendline)
library(propagate)
library(locfit)
library(raster)
library(rgdal)
```

```
library(sp)
setwd("D:/pitta/phd/tphd/lockdown/Phddata/ADO/stack_yearly")
files <- list.files()
a <- stack("2010.tif","2011.tif","2012.tif","2013.tif","2014.tif")
b <- stack("2015.tif","2016.tif","2017.tif","2018.tif","2019.tif")
v <- extract(a,c(1:29714))
u <- extract(b,c(1:29714))
n <- data.frame(v,u)

for (i in 1:29714){
fh <- sort(v[i,],na.last=TRUE)
sh <- sort(u[i,],na.last=TRUE)
if(!is.na(v[i,]) & !is.na(u[i,])){
        m <- lm(sh ~fh)
        S <- (2*(mean(sh,na.rm=TRUE)-mean(fh,na.rm=TRUE)))/length(n)
        D <- mean((sh-fh)*10/mean(fh,na.rm=TRUE),na.rm=TRUE)
        ssd <- (2*sqrt(2))*sd(n[i,],na.rm=TRUE)*sqrt(1-
        cor(sh,fh,use="complete.obs"))/length(n)/sqrt(length(n))
        CLlower95 <- 0 - 1.96*ssd
        CLupper95 <- 0 + 1.96*ssd
write.table(data.frame(i,S,D,ssd,CLlower95,CLupper95,summary(m)$coef[1,4],summary
(m)$coef[2,4]),file="first_AOD_lockdown_mod.csv",append=TRUE,na="",sep=',',col.na
mes=FALSE)
}
}
r <- raster("2000.tif")
g <- read.csv("second_AOD_lockdown_mod.csv")
for(i in 1:nrow(g)){
r[g[i,2]] <- g[i,11]
}
plot(r)
s <- raster("2001.tif")
for(i in 1:nrow(g)){
```

```
s[g[i,2]] <- g[i,3]
}
h <- reclassify(r,cbind(9999,NA))
values(h)
m = c(0, 0.05, 1, 0.05, 1, 0)
rclmat = matrix(m, ncol=3, byrow=TRUE)
p.mask = reclassify(h, rclmat)
fun=function(x) { x[x<1] <- NA; return(x)}
p.mask.NA = calc(p.mask, fun)
trend.sig = mask(s, p.mask.NA)
plot(trend.sig)
writeRaster(trend.sig,filename="second_95_0.tif",filetype="GTiff",overwrite=TRUE)
```

A.4 R code for Stack of the Database

```
library(raster)
library(sp)
library(rgdal)
library(maptools)
library(mapdata)
library(maps)
library(stringr)
setwd("E:/may2023/Chennai/New Folder/AOD")
files <- list.files()
y <- readOGR(dsn="D:/lockdown/south",layer="CH")
h <- raster("D:/lockdown/data/year/AOD/2000.tif")
for(i in 1:length(files)){
f <- raster(files[i])
p <- names(f)
t <- str_sub(p,11,22)
projection(y)=projection(f)
f <- setMinMax(f)
NAvalue(f) <- -9999     ## Fill values
```

```
j <- resample(f,h,method='bilinear')    ## Resample to AOD
e <- crop(f,extent(y))
n <- mask(e,y)
g <- 0.001000000047497451*n     ## Scaling of the data
##h <- g-273.15
writeRaster(g,
            file=                file.path('E:/may2023/extreme_data/short/AOD',
            paste0(t,'.tif')),overwrite=TRUE)


}
setwd("E:/may2023/extreme_data/short/AOD")
for(t in 2015001:2015365){
g <- list.files(pattern=as.character(t))    ## Grouping of data according to day of the year
d <- stack(g)
d <- setMinMax(d)
f <- mean(d,na.rm=TRUE)
writeRaster(f,file= file.path('E:/sep2022/site/CTP',paste0(t,'.tif')),overwrite=TRUE)
}
for(t in 2016365:2016366){
g <- list.files(pattern=as.character(t))
d <- stack(g)
d <- setMinMax(d)
f <- mean(d,na.rm=TRUE)
writeRaster(f,file= file.path('E:/sep2022/site/CTP',paste0(t,'.tif')),overwrite=TRUE)
}
for(t in 2017115:2017365){
g <- list.files(pattern=as.character(t))
d <- stack(g)
d <- setMinMax(d)
f <- mean(d,na.rm=TRUE)
writeRaster(f,file= file.path('E:/sep2022/site/CTP',paste0(t,'.tif')),overwrite=TRUE)
}
```

```
for(t in 2018001:2018365){
g <- list.files(pattern=as.character(t))
d <- stack(g)
d <- setMinMax(d)
f <- mean(d,na.rm=TRUE)
writeRaster(f,file=
file.path('E:/may2023/extreme_data/CTP',paste0(t,'.tif')),overwrite=TRUE)
}
for(t in 2019305:2019336){
g <- list.files(pattern=as.character(t))
d <- stack(g)
d <- setMinMax(d)
f <- mean(d,na.rm=TRUE)
writeRaster(f,file=
file.path('E:/may2023/extreme_data/CTP',paste0(t,'.tif')),overwrite=TRUE)
}
for(t in 2020001:2020366){
g <- list.files(pattern=as.character(t))
d <- stack(g)
d <- setMinMax(d)
f <- mean(d,na.rm=TRUE)
writeRaster(f,file=
file.path('E:/may2023/extreme_data/CTP',paste0(t,'.tif')),overwrite=TRUE)
}
for(t in 2021001:2021365){
g <- list.files(pattern=as.character(t))
d <- stack(g)
d <- setMinMax(d)
f <- mean(d,na.rm=TRUE)
writeRaster(f,file=
file.path('E:/may2023/extreme_data/AOD',paste0(t,'.tif')),overwrite=TRUE)
}
```

A.5 R code for Correlation Analysis

```
library(raster)
library(sp)
library(rgdal)
library(maptools)
library(mapdata)
library(maps)
library(stringr)
library(xlsx)
library(readxl)
library(ExcelFunctionsR)
setwd("D:/lockdown/day_5/AOD")
files <- list.files()
cor <- function(x){
a <- raster(file.path('D:/lockdown/day_5/AOD',paste0(x,'.tif')))
b <- raster(file.path('D:/lockdown/day_5/CF',paste0(x,'.tif')))
c <- raster(file.path('D:/lockdown/day_5/CTP',paste0(x,'.tif')))
d <- raster(file.path('D:/lockdown/day_5/CTT',paste0(x,'.tif')))
e <- raster(file.path('D:/lockdown/day_5/K',paste0(x,'.tif')))
u <- raster(file.path('D:/lockdown/day_5/prec_conv_day',paste0(x,'.tif')))
f <- resample(b,a,method='bilinear')
g <- resample(c,a,method='bilinear')
l <- resample(d,a,method='bilinear')
m <- resample(e,a,method='bilinear')
v <- resample(u,a,method='bilinear')
for ( j in 1:ncell(a)){
        if(isTRUE(v[j]>=35.6 && v[j]<124.4)){
        if(isTRUE (g[j]>680 && l[j]>0 && m[j]>=20)){
        if(!is.na(a[j])==TRUE && !is.na(f[j])==TRUE)
write.table(data.frame(x,j,a[j],f[j],g[j],l[j],m[j],v[j]),file=file.path('D:/lockdown/day/cor/heavy','cor_day_rain_modday19.csv'),na="",sep=",",append=TRUE,col.names=FALSE)
        }
```

```
}
}
}

for (i in 489:610){
p <- files[i]
q <- str_sub(p,1,7)
cor(q)
}
```

A.6 R code for Identification of EPEs

```
library(raster)
library(sp)
library(rgdal)
library(maptools)
library(mapdata)
library(maps)
library(stringr)
library(xlsx)
library(readxl)
library(ExcelFunctionsR)
setwd("E:/may2023/Hyderabad/Prec_poly")
files <- list.files()
a <- raster(file.path('E:/may2023/Hyderabad','ghmc_extreme.tif'))
h <- raster("E:/may2023/Hyderabad/ghmc_2000.tif")
heavy <- function(x){
b <- raster(file.path('E:/may2023/Hyderabad/Prec_poly',paste0(x,'.tif')))
d <- resample(b,h,method='bilinear')
e <- resample(a,h,method='bilinear')
for(i in 1:ncell(e)){
if(isTRUE((is.na(e[i])) | (d[i]< e[i]))){
        d[i]<- NA
```

```
}
}
##writeRaster(d,
                ##file=
                file.path("E:/may2023/Chennai/prec_greater95",paste0(x,'.tif')),overwrite=
                TRUE)
if(isTRUE(freq(d,value=NA)<15 | freq(d,value=NA)==15)){
writeRaster(d,
                file=
                file.path("E:/may2023/Hyderabad/prec_greater95_ghmc/true",paste0(x,'.tif
                ')),overwrite=TRUE)
}
}
for (i in 1:length(files)){
p <- files[i]
q <- str_sub(p,1,7)
heavy(q)
}
```

A.7 R code for Data Preparation to Analyse EPEs

```
library(raster)
library(sp)
library(rgdal)
library(maptools)
library(mapdata)
library(maps)
library(stringr)
setwd("E:/may2023/extreme_data/CTP")
files <- list.files()
y <- readOGR(dsn="D:/lockdown/south",layer="ghmc_poly")
h <- raster("E:/may2023/Hyderabad/ghmc_2000.tif")
m <- raster("D:/lockdown/data/year/AOD/2000.tif")
b <- raster(files[1])
```

```
d <- stack(b,b,b,b,b,b,b,b,b,b)
j <- 0
for(i in 2018144:2018153){
r <- raster(file.path("E:/may2023/extreme_data/CTP",paste0(i,'.tif')))
##t <- resample(r,m,method='bilinear')
##extent(t)<- extent(d)
if(isTRUE(i==2018144)){
        j <- 1
}else{
        j <- j+1
}
d[[j]]<- r
}
c <- resample(d,h,method='bilinear')
n <- mean(c,na.rm=TRUE)
q <- crop(n,y)
r <- mask(q,y)
writeRaster(r,filename="E:/may2023/Hyderabad/2018154/CTP_past10.tif",filetype="GTiff",overwrite=TRUE)
```